SLAC-PUB-3242
October 1983
(T/E)

JETS IN e^+e^- ANNIHILATION*

R. Hollebeek
Stanford Linear Accelerator Center
Stanford University, Stanford, California 94305

Presented at the 11th SLAC Summer Institute on Particle Physics
Stanford, California, July 18–29, 1983

* Work supported by the Department of Energy, contract DE-AC03-76SF00515.

1. Introduction

Jets in e^+e^- annihilation are either a fantastic surprise or completely expected behavior depending on how strongly one believes in the present quark picture of hadron dynamics. Before embarking on an explanation of what is seen in e^+e^- annihilation from the standard quark picture, let us take a moment to see why the production of jets might be a rather surprising phenomena.

The initial particles are known to be quite small when measured against many of the other mesons and hadrons which we will be talking about. For example, the Bhabha scattering process, $e^+e^- \rightarrow e^+e^-$, can be used to test for structure in these leptons since the scattering formula would be modified by the presence of a form factor as shown in Equation (1).

$$F_{\pm}(q^2) = 1 \pm \frac{q^2}{q^2 - \Lambda_{\pm}^2} \tag{1}$$

where Λ is a measure of the scale of the electron or positron substructure. When expressed in terms of an rms charge radius, this form factor becomes

$$F_{\pm}(q^2) = 1 - \frac{q^2\langle R^2\rangle}{6} + \cdots \tag{2}$$

and present limits on Λ_+ of approximately 100 GeV imply a charge radius

$$\langle R^2\rangle \lesssim \frac{6(\hbar c)^2}{\Lambda_+^2} \tag{3}$$

or R less than approximately 5×10^{-16} cm.

The simple quantum numbers of the initial state and standard conservation laws of the interaction greatly simplify the analysis of the final state since we expect that the total charge, baryon number, strangeness, charm, and lepton number of the final state will be zero. An additional simplification comes from the fact that at storage rings (except for radiative corrections) all experiments are done in the center of mass frame so that the sum of the final state momenta will be zero and the square of the sums of their individual energies

$$s = (\sum E_i)^2 = (2E_{beam})^2 \tag{4}$$

will be fixed. Values of E_{beam} up to ~ 20 GeV have been achieved.

Now the most fundamental question is how does all this energy, packed into the collision of two extremely small particles, convert itself into hadrons? Figure 1 shows

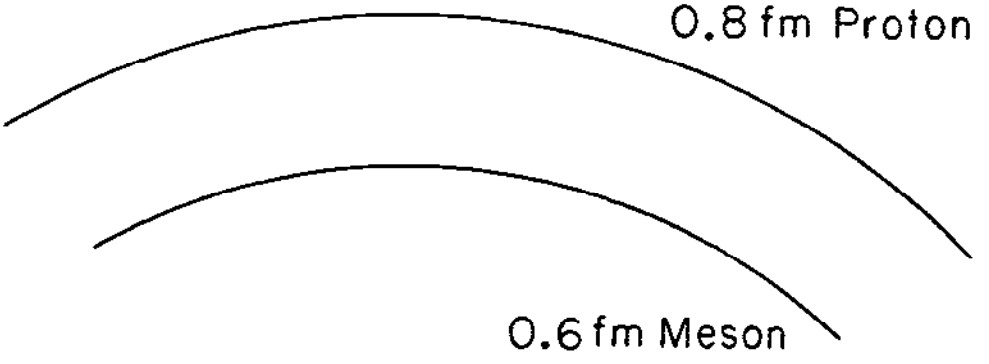

11-83
4681A1

Electron upper limit

Figure 1

the relative scales of the upper limit on the lepton when measured against the charge radii of the pi meson and the proton. The lesson to be learned here is that on the scale of what is going to be produced in the final state, electrons are extremely small! As we will see later, the bulk of the data on hadronic final states indicates that the particles emerge in two collimated jets traveling in opposite directions with approximately nine mesons in each jet. Our understanding of the details of this process is very sketchy; we are convinced by the striking two jet structure that the jets arise from the production of an initial state which at least for a time is two-body-like. We have almost no understanding of the detailed mechanism behind quantum number conservation within a jet or between jets.

2. Standard Quark Model

Our standard picture of matter is that it is composed of combinations of the spin 1/2, pointlike constituents called quarks shown in Table 1.

Table 1

Quark Charges and Masses

Quark		Charge	M_Q (GeV)
up	u	2/3	
down	d	-1/3	
strange	s	-1/3	$\sim .4$
charm	c	2/3	~ 1.5
bottom	b	-1/3	~ 5.0
top	t	2/3	?

This picture is supported by the known particles and their quantum numbers, the particle masses and decay branching ratios, and the presence of quark pair bound states such as the $c\bar{c}$ bound state ψ, ψ', at 3.1 GeV, $b\bar{b}$ bound states Υ, Υ' at 10 GeV and to a lesser extent light quark bound states such as the η, η' system $(s\,\bar{s})$ and the π mesons. Mesons are believed to be integer spin combinations of pairs of quarks while baryons are composed of 1/2-integer combinations of three quarks.

In addition to this basic picture of the composition of mesons and baryons, we believe that in many interactions the constituents interact as if they were *"Quasi-free"*. Scaling in deep inelastic eN scattering for example indicates the presence of

three pointlike constituents within the nucleon which interact independently. This extension of the quark composition model to the dynamics of independently interacting constituents (or partons) is often called the quark–parton model.

2.1 QUARK–PARTON MODEL OF e^+e^- ANNIHILATION

The Feynman diagram for the production of hadrons from e^+e^- annihilation is shown in Figure 2. We can analyze this cross section most easily in terms of another well-known pair production cross section namely $e^+e^- \rightarrow \mu^+\mu^-$ (Figure 3). Seen in the center-of-mass system, the cross section is given by

$$\frac{d\sigma}{d\Omega} = \frac{\alpha^2}{4s}\,\beta\left[1+\cos^2\theta+(1-\beta^2)\sin^2\theta+\beta^2 P^2\sin^2\theta\cos 2\theta\right] \tag{5}$$

where P is the initial state polarization (usually zero) and θ is the scattering angle between the e^+ and the μ^+. Since the muon is, like the electrons apparently point-like, the total cross section becomes

$$\sigma_{point-like} = \frac{4}{3}\,\pi\,\frac{\alpha^2}{s} = \frac{86.6nb}{s(GeV^2)}\left(\frac{e_\mu}{e}\right)^2 \tag{6}$$

If we now apply this formula to the production of hadrons, assuming that quarks are also point-like, we find that the total production cross-section for hadrons coming from an initial two-quark state in units of the muon pair cross section will be just

$$R = \frac{\sigma_h}{\sigma_\mu} = 3\sum_i Q_i^2 \tag{7}$$

where Q_i is the quark charge in units of the electron charge, and the sum runs over all quark pairs which can contribute at the available center-of-mass energy. The factor of three comes from the fact that we believe that quarks can come in each of three distinct types. This latter quantum number is called "color".

An additional consequence of this picture is that the quarks will have the angular distribution $1+\cos^2\theta$ characteristic of the production of spin-1/2 objects. If there were additional quarks of spin zero, we would expect a $\sin^2\theta$ distribution with the smaller cross-section

$$\sigma = \frac{\sigma_{point}}{4} \tag{8}$$

since there is no $(2J+1)$ spin sum in the final state of such a system.

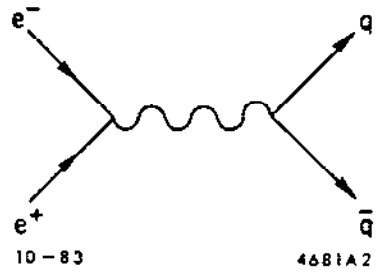

Figure 2

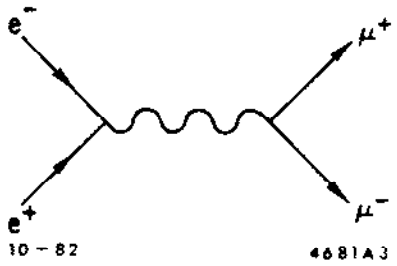

Figure 3

The behavior of R as a function of center-of-mass energy (shown in Figure 4) is in fact one of the most beautiful confirmations of this picture of hadron interactions. Except for the presence of the indicated bound states and resonances, $R(s)$ rises in discrete steps and agrees with the values predicted by the quark-parton picture.

The spin-1/2 nature of the quarks is seen in the fact that the angular distribution of hadrons produced does in fact have a $1 + \cos^2\theta$ distribution. We will come back to the problem of finding the initial quark axis from the directions of the final state particles (the approximately nine mesons in each jet), but if we define the thrust axis θ_T as a measure of the quark axis, then its distribution (Figure 5) shows the required behavior.[1]

A further consequence of the point-like nature of the quarks within the quark-parton picture is that the break-up of the quark into mesons to form a jet should be independent of the center-of-mass scale s. Thus we expect the cross-section to scale, i.e.,

$$\frac{d\sigma}{dx} \sim \frac{1}{s}\, f(x) \tag{9}$$

where x is the dimensionless ratio

$$x = \frac{2E_h}{\sqrt{s}} \quad .$$

Although small violations of this behavior are seen, this scaling parameterization works well over a large range of energies provided the x value is greater than approximately 0.2 (see Figure 6).

2.2 Phase Space for N Body Final States

We would now like to ask increasingly more detailed questions about what is seen in the final states of these interactions in order to learn more about the dynamics involved in the production of the hadronic matter. But before doing this, it is useful to examine the consequences of a model in which all of the dynamics is determined by the n body phase space integral. The earliest of such models is due to Fermi[2] and with some modifications explains many of the features which we observe. The analysis of the phase space integrals which I am following is due to Lepore and Stuart.[3] The basic principle is to Fourier transform the energy-momentum conserving delta function using

$$\delta = \int_{-\infty}^{\infty} d\alpha\, e^{i(\sqrt{s} - \sum E_i)\alpha} \int_{-\infty}^{\infty} d^3\lambda\, e^{i \sum p_i \lambda} \quad . \tag{10}$$

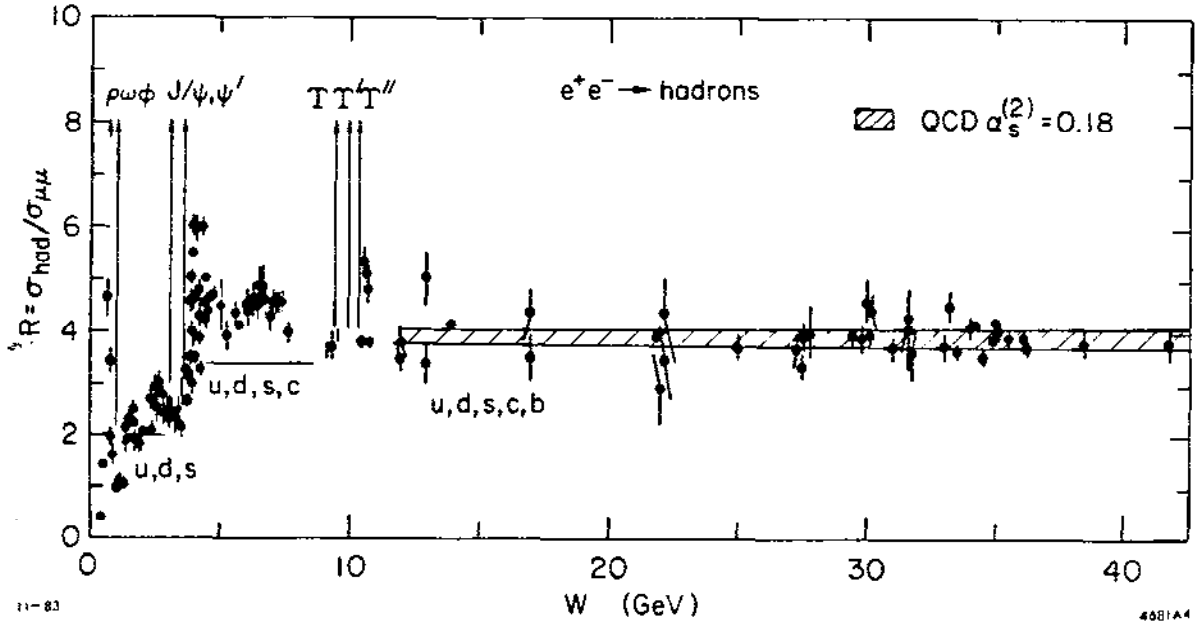
10
8
6
4
2
0
0
10
20
30
40
W (GeV)
R = σhad/σμμ
ρωφ J/ψ,ψ′
TT′T″
e+e− → hadrons
QCD α(2)s = 0.18
u,d,s
u,d,s,c
u,d,s,c,b

Figure 4

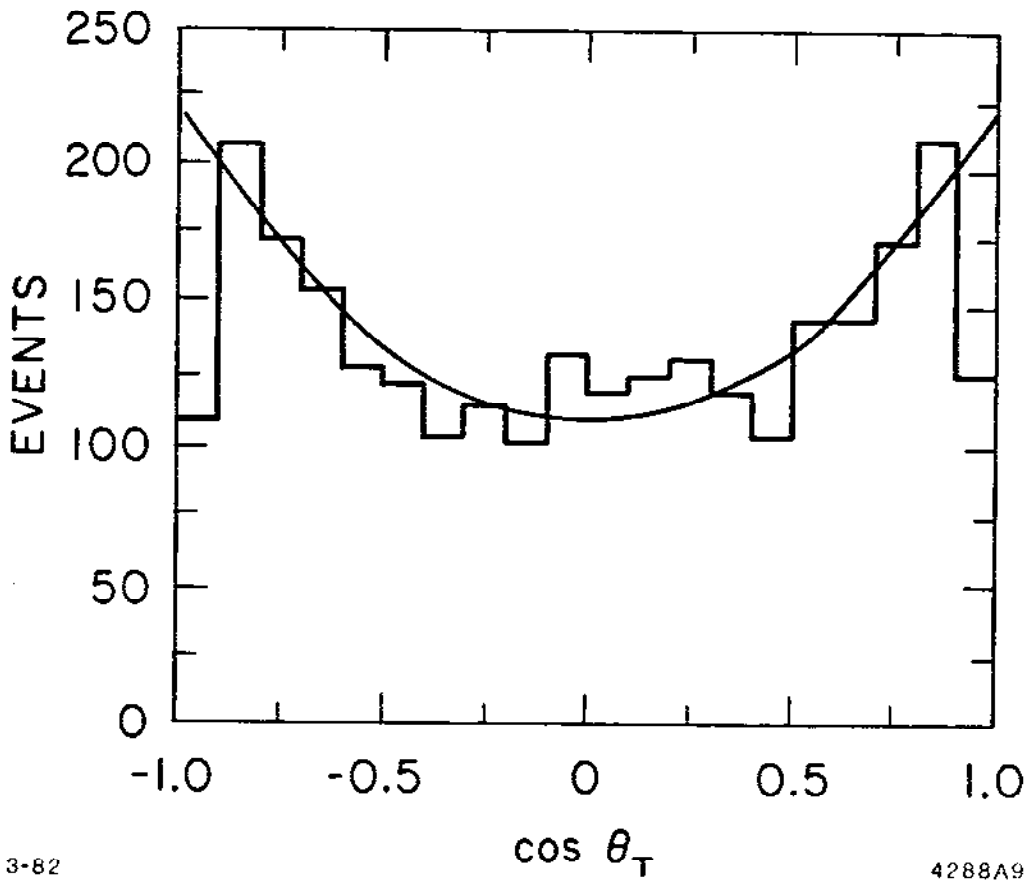

Figure 5

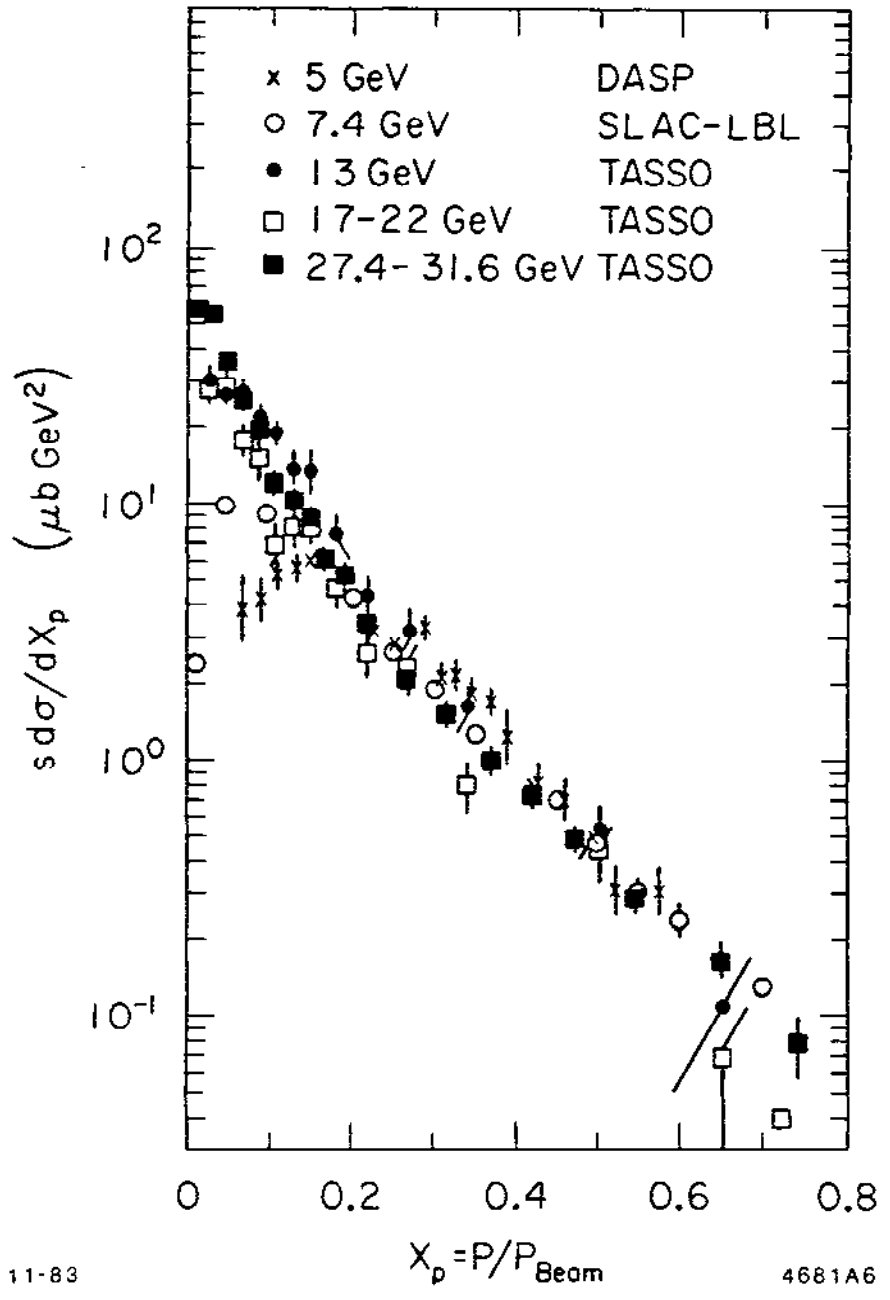
× 5 GeV DASP
○ 7.4 GeV SLAC-LBL
● 13 GeV TASSO
□ 17-22 GeV TASSO
■ 27.4-31.6 GeV TASSO
10^2
10^1
10^0
10^{-1}
$s\,d\sigma/dX_p$ ($\mu b\,GeV^2$)
0
0.2
0.4
0.6
0.8
$X_p = P/P_{Beam}$
11-83
4681A6

Figure 6

The angular integrals can be done by introducing the variables $p = M \sinh \theta$ and $E = M \cosh \theta$ and we find that the result is of the form

$$\int d^3\lambda \int d\alpha \, e^{i\sqrt{s}\,\alpha} \prod I_i \tag{11}$$

where

$$I_i = \frac{2\pi^2}{i} \frac{M}{(\alpha^2 - \lambda^2)^{1/2}} H_1^{(2)} \left[M(a^2 - \lambda^2)^{1/2} \right] .$$

Making use of the relation between n and $n-1$ body phase space,

$$E \frac{d^3 R_n(s)}{dp^3} = \frac{1}{2} R_{n-1}(s + m^2 - 2\sqrt{s}\, E) \tag{12}$$

where each of the final particles is assumed to have mass m, we find that the phase space integrals can be solved in two limits. If the individual particle masses are large compared to the available energy, i.e.,

$$s - (\sum m_i)^2 \ll s \tag{13}$$

we have the nonrelativistic limit to be applied to particle production at low x. This has the form

$$\frac{E d^3\sigma}{dp^3} \sim e^{-M_x/m} \tag{14}$$

where $M_x^2 = s + m^2 - 2\sqrt{s}\, E$. At high x where the particle masses are negligible, we have the relativistic limit

$$\frac{E d^3\sigma}{dp^3} \sim (1 - x)^{(2n-6)/2} \tag{15}$$

where $x = 2E_h/\sqrt{s}$.

From Equations (14) and (15) we can see that we expect scaling behavior in this simple model. The slope of $d\sigma/dx$ will be steeper at small x and will be dependent on the masses of the produced particles. At the high x end, the distribution will be determined by the mean multiplicity $\langle n \rangle$ and will scale if $\langle n \rangle$ changes slowly with s. Within statistics, these features are consistent with the data shown in Figure 6. Note that at small x in the figure a correction has to be made for the use of $x_p = p/p_{beam}$.

2.3 How Do We Get Jets?

Despite the fact that the production of two quasi-free quarks seems to explain many of the features of the data, we have still to look closer at the conversion of

these quarks into many hadrons. Up to now we have considered the process of multihadron production as a two-step process as shown in Figure 7. The conversion of the quarks into hadrons was assumed to leave the magnitude of the production cross-section unmodified, and the quark axis was found to be preserved in the axis of the jets themselves. The fact that the axis is visible at all, and that jets are seen is actually a consequence of the limited $p_\perp$ behavior of hadronic interactions. The invariant cross-section $(Ed^3\sigma)/(dp^3)$ can be rewritten in terms of two new variables: rapidity, defined as

$$y \equiv \frac{1}{2}\ell n\left(\frac{E+p_\parallel}{E+p_\parallel}\right) \quad , \tag{16}$$

and the transverse momentum $p_\perp$ relative to some axis. The relation between these two expressions is just

$$\frac{Ed^3\sigma}{dp^3} = \frac{d^2\sigma}{dydp_\perp^2} \quad . \tag{17}$$

In hadronic interactions, one usually finds that transverse momenta relative to an incoming quark direction are suppressed so the cross-sections have the form

$$\frac{d^2\sigma}{dydp_\perp^2} \sim e^{-\alpha p_\perp^2} \quad . \tag{18}$$

If we extend this observation to the conversion or fragmentation of the quark into hadrons, we would expect to have to introduce a matrix element

$$|M|^2 = e^{-p_\perp^2/2\sigma_q^2} \quad . \tag{19}$$

If σ_q is small enough compared to the momenta of the hadrons, this form will result in the preservation of the quark axis in the directions of the final state hadrons. Since there is no modification of the rapidity distribution, we expect this distribution to be flat out to a maximum rapidity y_{MAX} determined by the available energy. Integrating over the inclusive cross-section of Equation (17) we also find that the mean multiplicity will be related to y_{MAX} and hence the growth of $\langle n\rangle$ with center-of-mass energy will be just

$$\langle n\rangle \sim y_{MAX} \sim \ell n\, s \quad . \tag{20}$$

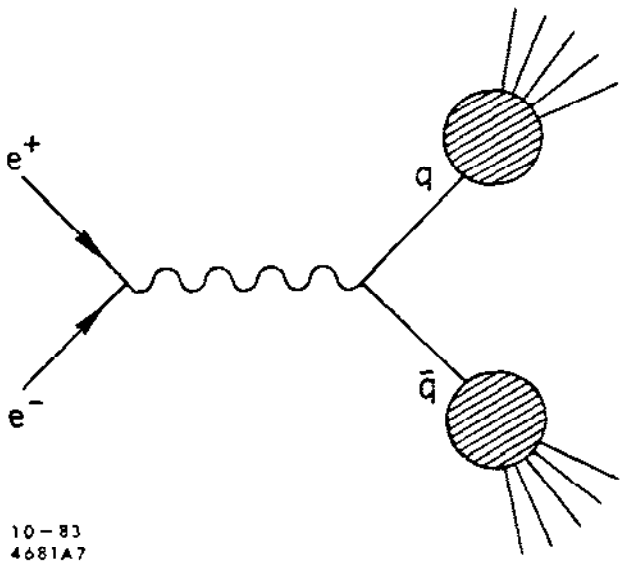

Figure 7

This has the extremely important consequence that since the multiplicity is growing slower than $\sqrt{s}$, the mean energy per particle increases with s. Since the angular deviation of a particle from the quark axis is determined by the ratio between $\langle p_\perp \rangle$ (which is fixed by σ_q) and $\langle E \rangle$, the jets will become more and more collimated and easier to recognize as s increases. The cone angle of the jet will be roughly

$$\delta \sim \frac{\langle p_\perp \rangle}{\langle p_\parallel \rangle} \sim \frac{\ell n\, s}{\sqrt{s}} \quad . \tag{21}$$

Before the advent of machines with available center-of-mass energies in the 30 GeV range, establishing the existence of jet-like behavior required a detailed analysis of the final state structure[4]; however, with present energies, the jets are quite clear. A typical two jet event from the MARK II detector at PEP ($\sqrt{s} = 29$ GeV) is shown in Figure 8.

Figure 9 shows the rapidity distributions as a function of y and $y - y_{\rm MAX}$ for a range of energies. For each energy, there is a wide region where the y distribution is flat, and different energies have similar shapes for the fall off near y_{MAX}. However, there are some problems with our simple picture. First, the cross-section at small y is not the same at all energies indicating that $(d\sigma/dy)|_{y\sim 0}$ is not really constant. While this may not be surprising between 4.8 GeV and 13 GeV due to threshold effects in the production of heavy charmed or bottom mesons, some of the effect remains between 13 GeV and the highest energies. [This effect can be seen in the inset of Figure 9(a).] Second, in the high statistics, high energy data there is perhaps a decrease near $y = o$ which indicates a suppression of production of particles with small $p_\parallel$.

2.4 More Problems with the Simple Two-Jet (Limited $p_\perp$) Picture

Even though the limited $p_\perp$ picture explains the shape of the rapidity and $p_\perp$ distributions reasonably well, we have seen in the last figure that it does not correctly account for the behavior of $d\sigma/dy$ near $y = 0$. This can also be seen by looking at the behavior of the normalization of these curves as a function of center-of-mass energy. If only charged particles are used, (the neutrals have similar behavior) the normalization of $(d^2\sigma)/(dy dp_\perp^2)$ will be the average charged multiplicity $\langle n_{CH} \rangle$. The prediction of the limited $p_\perp$ model was that if σ_q was fixed, this multiplicity would rise like $y_{\rm MAX}$, namely $\langle n_{CH} \rangle \sim \ell n\, s$. However, from Figure 10 we can see that this is not the case. In the low energy region (1.4 to 7 GeV) the best fit to the data is

$$\langle n_{CH} \rangle = (2.67 \pm 0.04) + (0.48 \pm 0.02)\, \ell n\, s \tag{22}$$

but in the high energy region (7 GeV to 31.6 GeV) this becomes

$$\langle n_{CH} \rangle = (-6.1 \pm 0.4) + (2.79 \pm 0.06)\, \ell n\, s \quad . \tag{23}$$

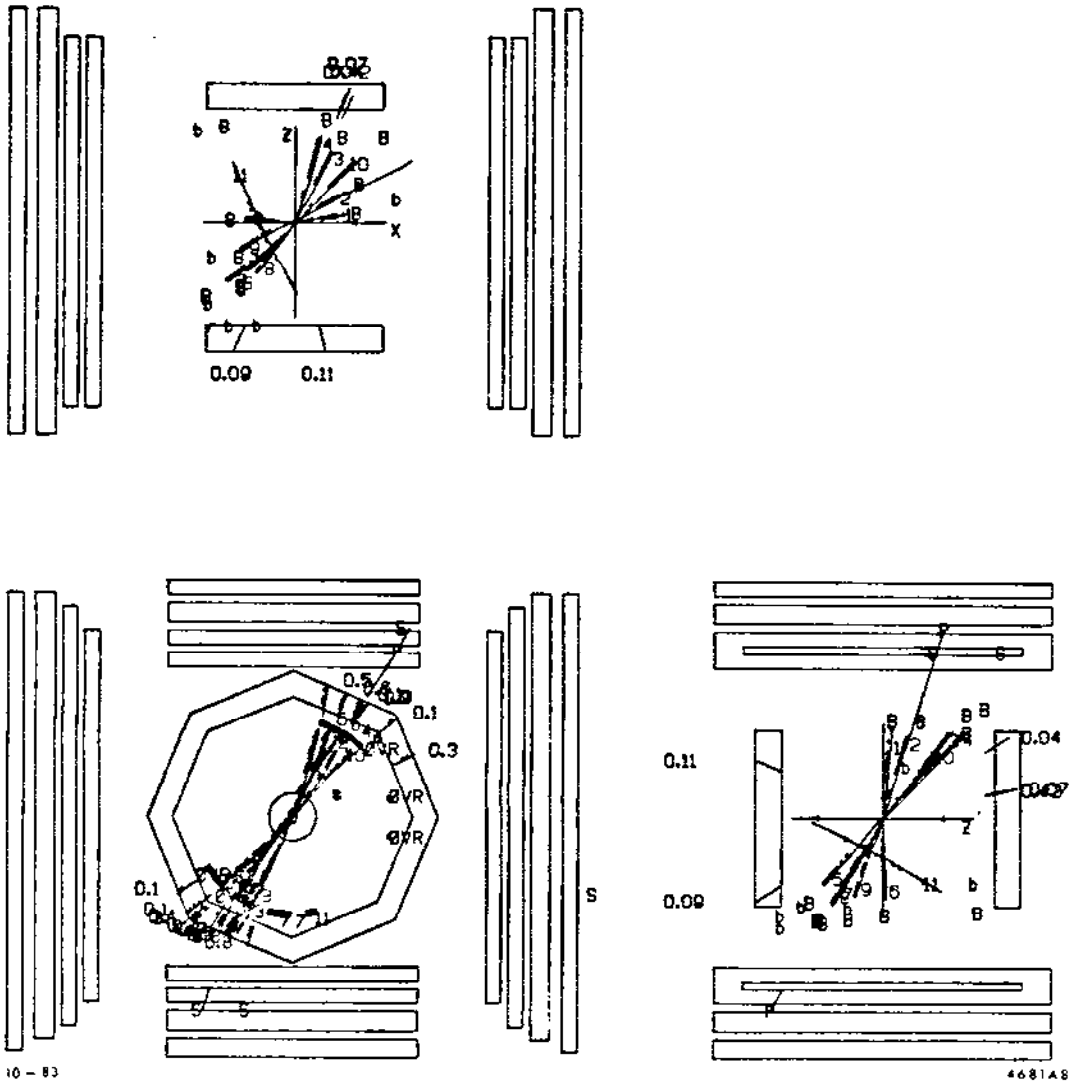

Figure 8

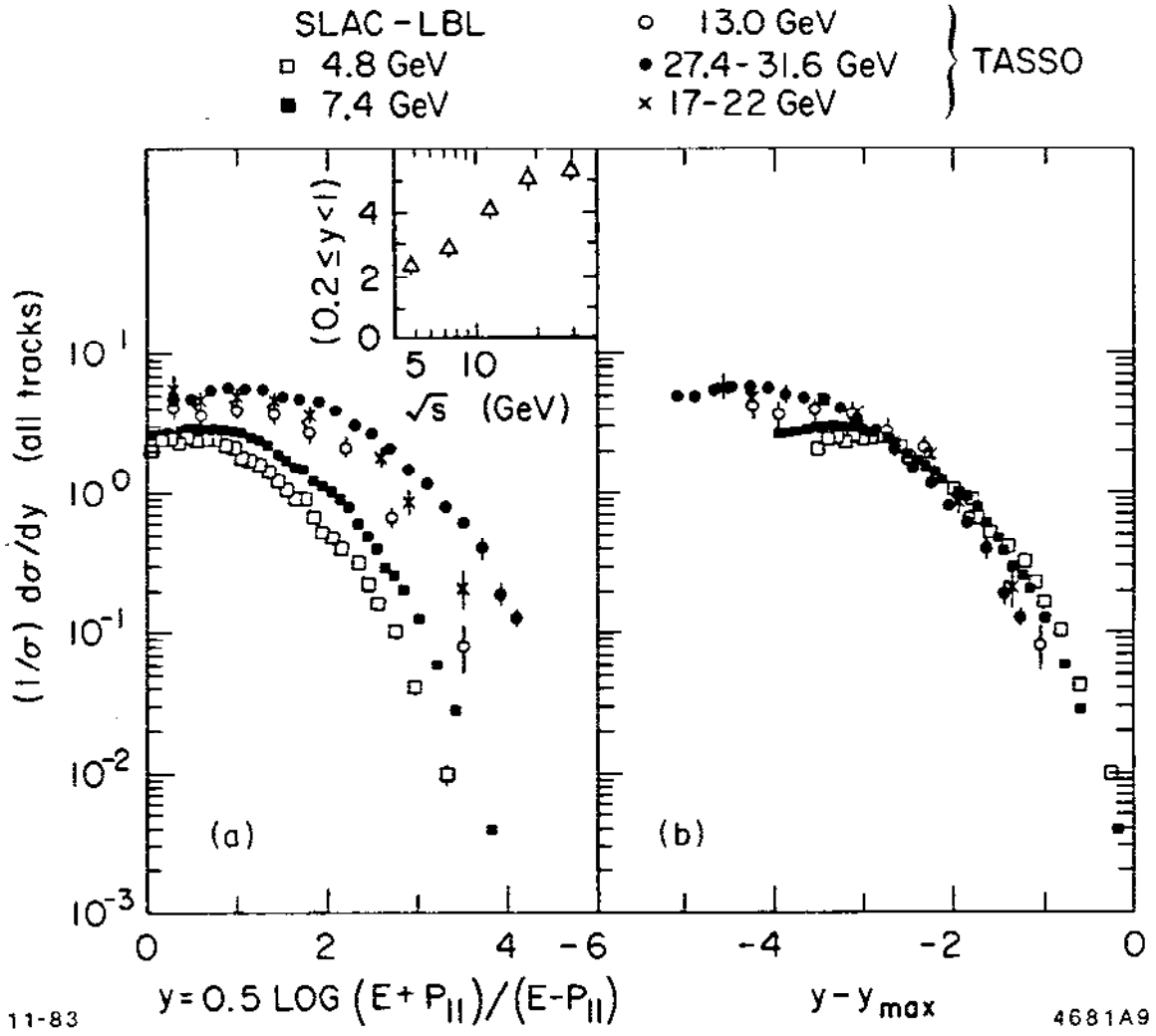
SLAC - LBL
4.8 GeV
7.4 GeV
13.0 GeV
27.4 - 31.6 GeV
17-22 GeV
TASSO
(1/σ) dσ/dy (all tracks)
(0.2≤y<1)
√s (GeV)
(a)
(b)
y = 0.5 LOG (E+P∥)/(E-P∥)
y - y max
11-83
4681A9

Figure 9

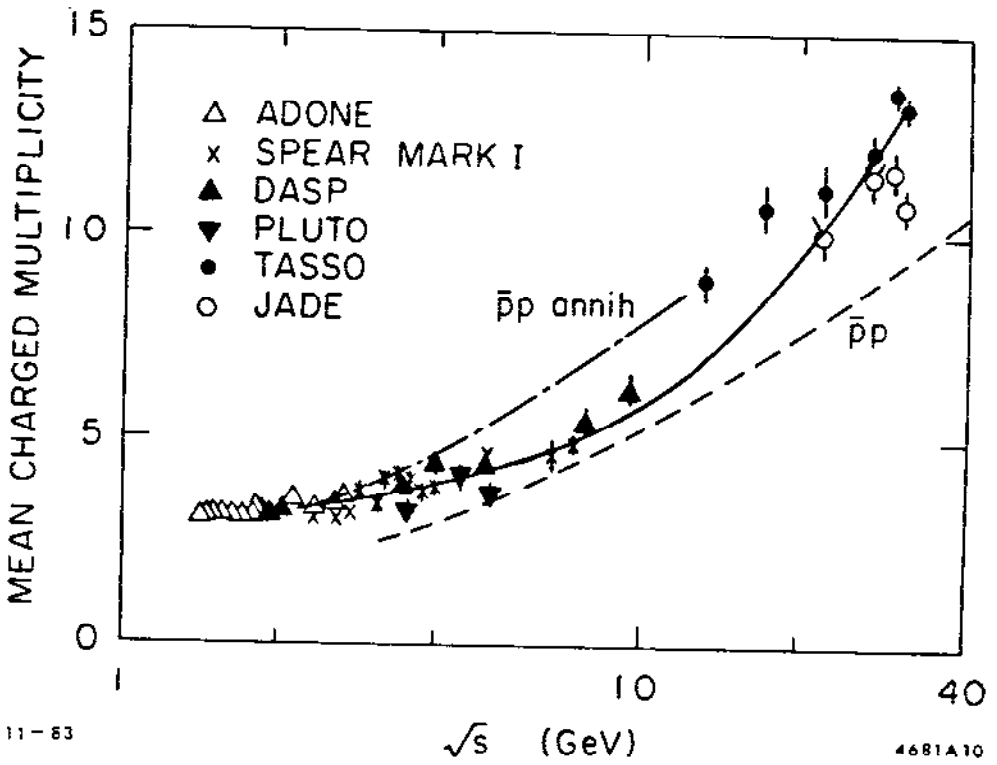
MEAN CHARGED MULTIPLICITY
15
10
5
0
1
10
40
√s (GeV)
ADONE
SPEAR MARK I
DASP
PLUTO
TASSO
JADE
p̄p annih
p̄p
11-83
4681A10

Figure 10

The fit shown in the solid curve[5]

$$\langle n_{CH} \rangle = n_o + a\, exp\left\{ b\sqrt{\ell n\,(s/\Lambda^2)} \right\} \tag{24}$$

with $\Lambda = 0.5$ GeV, $n_o = 2.92 \pm 0.04$, $a = 0.0029 \pm 0.0005$ and $b = 2.85 \pm 0.07$, is motivated by QCD or quantum chromodynamics in which three-jet events are expected to contribute to the increase in multiplicity. Simpler forms can also describe the data, of course, and in fact the Fermi statistical model, though it does not predict the two-jet structure of the events, has a variation of $\langle n_{CH} \rangle$ with energy which is

$$\langle n_{CH} \rangle \sim s^{1/4} \tag{25}$$

and is in good agreement with the data. A reasonable fit is also obtained from

$$\langle n_{CH} \rangle = 2. + 0.2\ \ell n\, s + 0.13\ (\ell n\, s)^2 \tag{26}$$

with s in GeV.

The problems with $d\sigma/dy$, the incorrect behavior of $\langle n_{CH} \rangle$ with energy, and tails in the $p_\perp$ distribution (to be discussed later) all lead us to abandon the simplest two-jet picture of hadron events. Additional contributions to the multiplicity and modifications to $d\sigma/dy$ and $d\sigma/p_\perp$ could arise from three-jet production at high energies but we must be careful to add this new process in a way which does not destroy the good agreement which we have found for $R(s)$.

3. Shape Measures

In order to see whether three-jet events or even four-jet events are present in the data, we need to have ways of measuring the hadronic final states and classifying them into two-, three- and four- or more jet samples. One way of doing this is known as the *Momentum Tensor Analysis*[6] and proceeds by finding the eigenvalues of the momentum tensor summed over all particles:

$$M_{\alpha\beta} = \frac{\sum P_{i\alpha} P_{i\beta}}{\sum p_i^2} \tag{27}$$

$$\alpha,\ \beta = x,\ y,\ z$$

The solution to the eigenvalue problem for this tensor finds the set of axes which minimizes the relative transverse momentum squared with respect to those axes. The motivation for finding an axis which minimizes $p_\perp^2$ is of course that the limited $p_\perp$

behavior of the quark fragmentation leads us to think that this axis will be a good estimator of the original quark direction. If we order the eigenvalues such that $Q_1 < Q_2 < Q_3$ then the associated eigenvectors $\hat{n}_1, \hat{n}_2, \hat{n}_3$, of the momentum ellipsoid will be as shown in Figure 11(a). The mean squared momenta relative to the shortest axis is

$$\frac{\langle P_{out}^2 \rangle}{\langle P^2 \rangle} \equiv \frac{\Sigma\,(\underline{p} \cdot \hat{n}_1)^2}{\Sigma\; p^2} = Q_1 \qquad . \tag{28}$$

Similarly for the axis $\hat{n}_2$ we define

$$\frac{\langle P_{in}^2 \rangle}{\langle P^2 \rangle} = Q_2 \qquad . \tag{29}$$

For our model of hadron production, we expect that most events will originate from two quarks fragmenting in oppositely directed cones as shown in Figure 11(b). In this case, the eigenvalues Q_1 and Q_2 should be approximately equal, and if the energy is high enough for the mean transverse momentum to be small compared to the mean particle energy, Q_1 will be much less than Q_3. Events with three jets will originate from three partons whose vectors lie in a plane. On average, this plane will be normal to the eigenvector $\hat{n}_1$ if again σ_q is small enough compared to the mean particle energy. In fact, if we assume that the three partons fragment in these events in a way which is similar to two-jet fragmentation, then we would find Q_1 unchanged in three-jet events, but Q_2 somewhat larger.

If there are many jets in an event, or if the energy is low, the event will look spherical, i.e.,

$$Q_1 \sim Q_2 \sim Q_3 = \frac{1}{3} \qquad . \tag{30}$$

A convenient variable to use for testing for this condition is *sphericity* defined as

$$S = \frac{3}{2}(1 - Q_3) = \frac{3}{2}\,\frac{\langle P_{out}^2 \rangle + \langle P_{in}^2 \rangle}{\langle p^2 \rangle} \qquad . \tag{31}$$

(This was actually one of the original variables used at low energy to establish the existence of two-jet events.) Spherical events will have $S = 1$ and jetty events will have small sphericities. Similarly, we can define *aplanarity* in terms of the smallest eigenvalue (which should be the same for two-jet and planar three-jets)

$$A = \frac{3}{2}\,Q_1 \tag{32}$$

and since this is insensitive to three-jet events and sensitive only to distributions out of the plane normal to $\hat{n}_1$, we can use it to look for heavy particle production or four and more jet events.

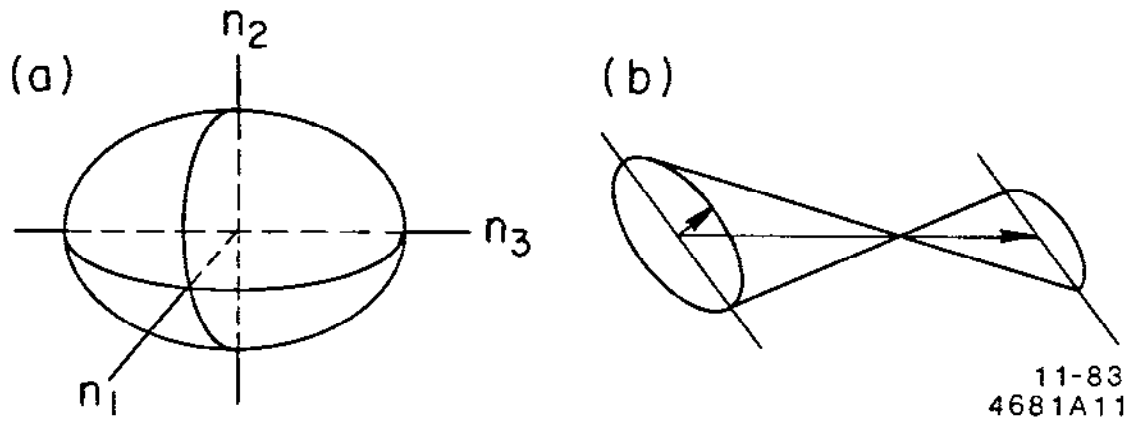

Figure 11

3.1 LINEAR SHAPE VARIABLES

There is one major problem in principle with the momentum tensor approach to finding parton directions. Since the eigenvalue problem minimizes the transverse momentum of particles relative to the axes in a least squares sense, the axes and eigenvalues are nonlinear functions of the particle momenta. This makes the theoretical calculation of, for example, the sphericity distribution a difficult task. Worse, however, is the fact that this nonlinearity makes the method sensitive to the details of the quark fragmentation. As an example of this, since $p_\perp^2$ is minimized, if we paired all particles and reminimized using the resultant vectors of these pairs, we would find different eigenvectors. Thus if quarks fragmented a significant fraction of the time into ρ mesons which then decayed into π pairs, this would modify the momentum tensor quantities.

One solution to this dilemma is to linearize the problem. Thus we can define a new axis $\hat{n}_3$ called the thrust axis which maximizes the linear sum of projected momenta along $\hat{n}_3$. A similar extension for the other two axes yields the "eigenvalues"

$$\text{THRUST} \qquad T = \frac{\text{MAX} \sum |p \cdot \hat{n}_3|}{\sum |p|} \tag{33}$$

and

$$\text{MAJOR AXIS} \qquad M_2 = \frac{\text{MAX} \sum |p \cdot \hat{n}_2|}{\sum |p|}$$

where $\hat{n}_2$ is required to be perpendicular to $\hat{n}_3$. The minor axis is defined as the axis perpendicular to the thrust and major axes.

$$\text{MINOR AXIS} \qquad M_1 = \frac{\sum |p \cdot \hat{n}_1|}{\sum |p|} \quad . \tag{34}$$

Deviations from the two-jet hypothesis can be seen by the analog of comparing Q_1 and Q_2 in the momentum tensor analysis. Thus we define the *oblateness* as

$$O = M_2 - M_1 \quad . \tag{35}$$

The analog of sphericity in the linear analysis is *spherocity*[7], defined as

$$S' = \frac{16}{\pi^2} \left[\frac{\sum |p_\perp|}{\sum |p|} \right]^2 \tag{36}$$

and the analog of aplanarity is *acoplanarity*,[8]

$$\mathcal{A} = 4M_1^2 \quad . \tag{37}$$

Triplicity is the sum of the momenta projected along the three axes and approaches one for a perfect three-jet event. When studying the details of three-jet events, it is convenient to look for three axes which minimize the linear sums of transverse momenta with the additional requirement that the three axes must lie in a plane. In this case, the *trijetiness*[9] is defined to be a measure of how well the event conforms to the hypothesis of three planar jets.

As a further extension of these shape measures, standard clustering techniques from numerical analysis can be applied to determine the number of jets in an event. In most previous measures, an assumption has to be made about the number of jets and then tested. If clustering algorithms are used however, criteria can be made for a cluster to be considered a jet, and low energy clusters or other clusters which do not meet these requirements can be removed and/or merged with other clusters. To associate particle groups into clusters requires a metric in momentum and/or position space which defines the "distance" in a clustering sense between any two particles. The easiest way to group the particles is then to use MIN/MAX techniques which start clusters using particles separated by greater than MAX while merging into a cluster all other particles closer than MIN.

While clustering techniques are attractive because they make no *a priori* assumptions about the number of jets, care must be taken in interpreting the results since some metrics are linear and some are not. Nonlinear metrics will have problems with fragmentation similar to those discussed before. In addition to nonlinearities, there may be complicated procedures for merging clusters or associating clusters with jets. However, one of the major strengths of the clustering technique lies in this flexibility since the algorithm can be adjusted and optimized for a particular analysis task using a detailed model or Monte Carlo.[10]

3.2 Energy Dependence of Shape Measures

We now return to the simple model in which the rapidity distribution is flat and the $p_\perp$ is fixed. Since the mean multiplicity is proportional to $\ell n\, s$, the mean momentum is $\langle p \rangle \sim \sqrt{s}\,/\ell n\, s$, and the variation of sphericity with energy will be approximately

$$S = \frac{3}{2}\frac{\langle p_\perp^2 \rangle}{\langle p^2 \rangle} \sim \frac{\langle n \rangle^2}{s}\,\langle p_\perp^2 \rangle \sim \frac{(\ell n\, s)^2}{s} \quad . \tag{38}$$

The data[11] are shown in Figure 12 as a function of $\sqrt{s}$, and **do not** fall as sharply as Equation (38) over the whole range.

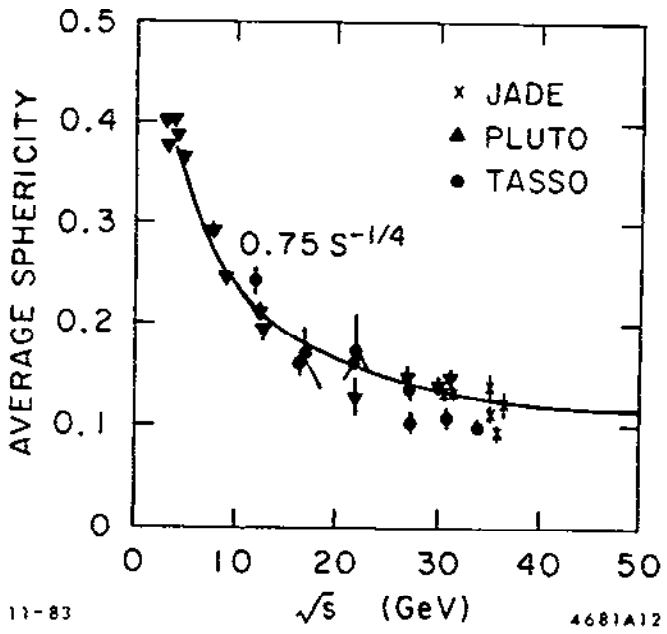
AVERAGE SPHERICITY
0.5
0.4
0.3
0.2
0.1
0
0 10 20 30 40 50
√s (GeV)
× JADE
▲ PLUTO
● TASSO
0.75 S^-1/4
11-83
4681A12

Figure 12

Since the sphericity is related to the eigenvalues Q_1, Q_2, Q_3 by

$$S = 3/2(1 - Q_3) \quad , \tag{39}$$

if we make the assumption that Q_1 and Q_2 are equal and use the fact that

$$Q_1 + Q_2 + Q_3 = 1 \tag{40}$$

we can determine both Q_1 (the shortest axis of the ellipsoid of the average event) and Q_3 (the long axis) for each value of sphericity. The ratio gives the eccentricity of the ellipse

$$\frac{Q_3}{Q_1} = \frac{1 - \frac{2}{3}S}{\frac{1}{3}S} \quad . \tag{41}$$

Table 2 shows this ratio evaluated at low, medium and high energy and illustrates that even though the sphericity does not decrease as rapidly as Equation (38), the events have become much more jet-like at high energies. Figure 13 shows the changes in the distributions for sphericity and aplanarity.[12]

Table 2

Variation of the Maximum to Minimum Axis Ratio with Energy

$\sqrt{s}$	Sphericity	Q_3/Q_1
4	0.4	5.6
10	0.24	10.5
40	0.12	23.0

3.3 Evidence for More Than Two-Jets

The large ratio Q_3/Q_1 makes it rather easy to believe in two-jets at high energy, but as we have seen, the simplest model predicts a too rapid fall off of the sphericity, does not predict the growth of the central region $(d\sigma/dy)|_{y\approx 0}$, and does not predict the rapid rise in multiplicity. The most striking evidence that more jets are required, however, comes from looking directly at the $p_\perp$ distributions. Figure 14 compares the normalized distribution of the square of the transverse momentum for charged particles relative to the event axis at low and high energies.[13] While the behavior at low $p_\perp^2$ is similar, there is a substantial change at high $p_\perp^2$. In order to distinguish between an increase in $p_\perp^2$ due to an energy dependent σ_q and the production of planar three-jet events, we compare the behavior of the distributions of the eigenvalues Q_1 and Q_2.

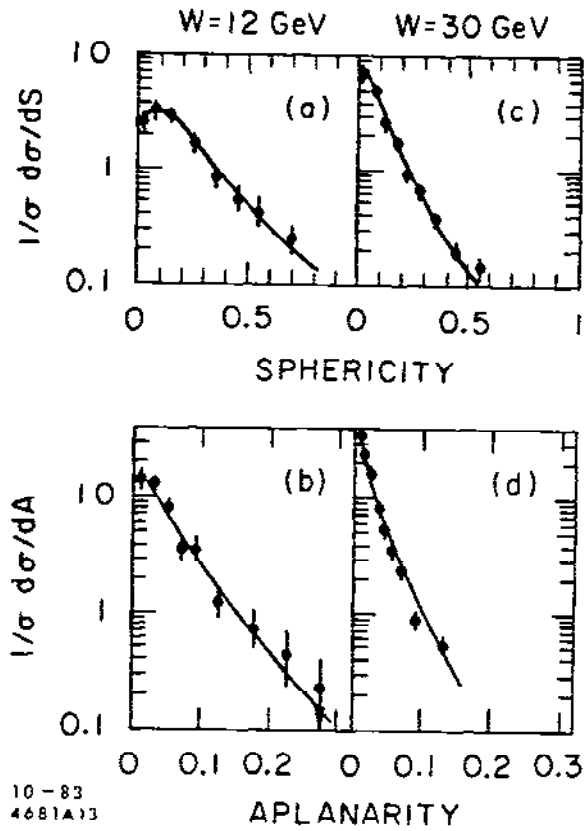
W=12 GeV
W=30 GeV
10
1
0.1
1/σ dσ/dS
(a)
(c)
0
0.5
0
0.5
1
SPHERICITY
(b)
(d)
1/σ dσ/dA
0
0.1
0.2
0
0.1
0.2
0.3
APLANARITY
10-83
4681A13

Figure 13

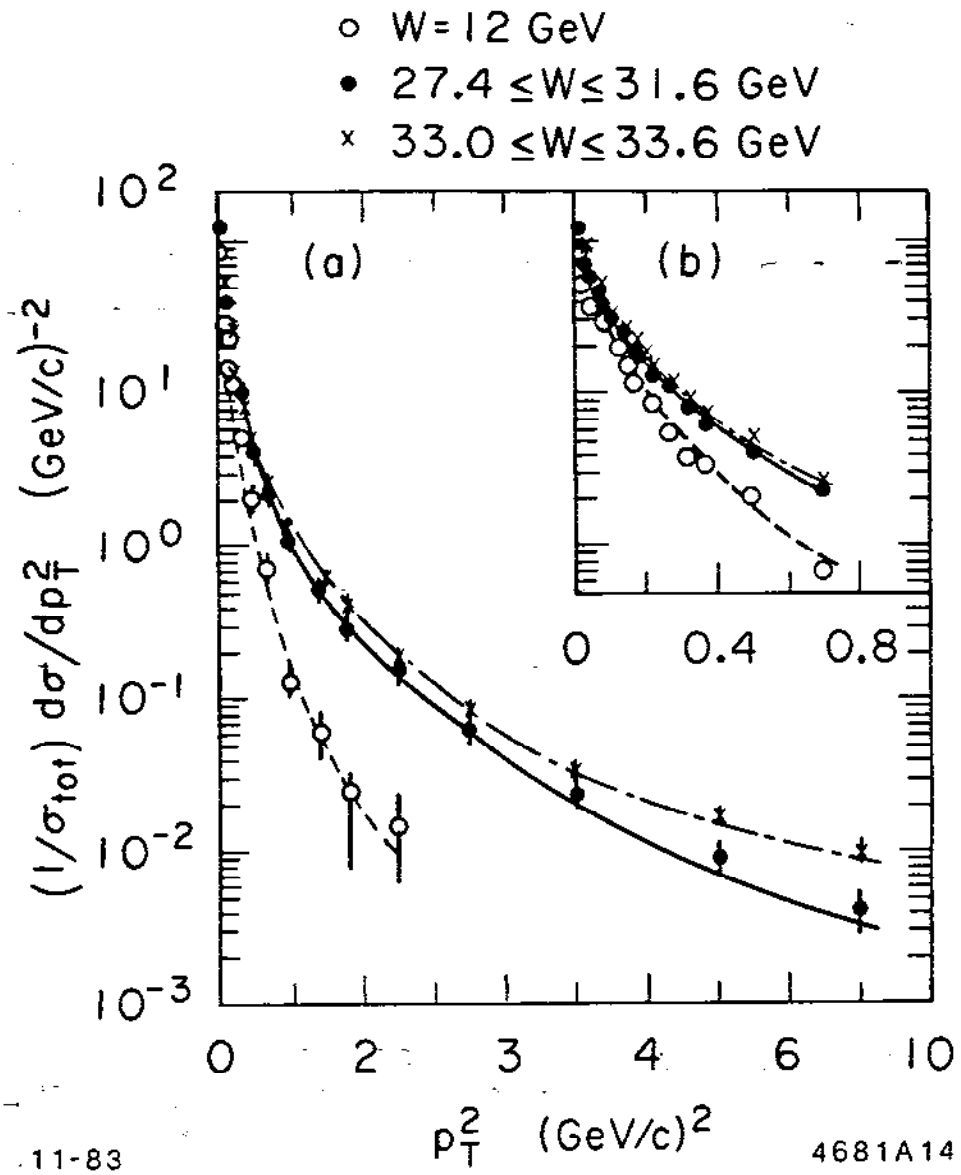
o W = 12 GeV
• 27.4 ≤ W ≤ 31.6 GeV
× 33.0 ≤ W ≤ 33.6 GeV
(a)
(b)
10^2
10^1
10^0
10^{-1}
10^{-2}
10^{-3}
$(1/\sigma_{tot})\, d\sigma/dp_T^2$ (GeV/c)$^{-2}$
0
2
3
4
6
10
0
0.4
0.8
p_T^2 (GeV/c)^2
11-83
4681A14

Figure 14

If the change were due to an increase in σ_q, then the events would be faster ellipsoids but with Q_1 still approximately equal to Q_2 The data, however, indicate that the energy behavior of these two quantities is quite different. Figure 15 shows that almost all of the increase in $p_\perp^2$ is coming from an increase in $p_\perp$ **in the plane** of the event.

The curves in Figure 15(a) and (b) indicate the effect of increasing σ_q from 300 MeV/c to 450 MeV/c. While such a modification would be consistent within statistics for the behavior of P_{in}, it fails to describe the long tail in P_{out} at high energy. Figure 15(e) and (d) indicate the quality of the agreement within a model which has a fixed σ_q but a small admixture of planar events at high energy.[13]

4. The Third Jet

We would now like to add a third jet, but in doing so we must be careful not to disturb the basic perturbative picture we have been using which explains the total cross section in terms of quark pair production. If three jet production proceeds through a process like that shown in Figure 16, the coupling constant at the new vertex must be small. A natural candidate for the parton which gives rise to the third jet is the same object which mediates the strong force between quarks. This "gluon", so named because it forms the glue which gives rise to strong binding, must in our case have a coupling constant much less than one.

A consistent picture of these interactions exists in the theory of quantum chromodynamics, which allows the strong interaction to be treated perturbatively in some cases. The coupling constant, α_s, is not constant, but decreases with increasing Q^2. The variation of the coupling constant is given by

$$\alpha_s = \frac{12}{11N_c - 2N_f} \frac{1}{\ell n\, s/\Lambda^2} \tag{42}$$

where N_f is the number of flavors of quarks (u, d, s ...) whose masses are small compared to $\sqrt{Q^2}/2$ and N_c is the number of colors. The constant Λ determines the rate of variation of α_s. It is important to note that α_s and Λ are **not** independent parameters. As shown below, given α_s at a particular Q^2, one can solve for Λ and determine α_s at all Q^2's.

Coupling constants which vary with Q^2 are present even in QED where the sum of the two diagrams shown in Figure 17(a) renormalizes the QED coupling constant α to

$$\alpha(Q^2) = \alpha(\mu_0^2)\left[1 + \frac{\alpha(\mu_0^2)}{3\pi}\ \ell n\ \frac{Q^2}{\mu_0^2}\right] \quad . \tag{43}$$

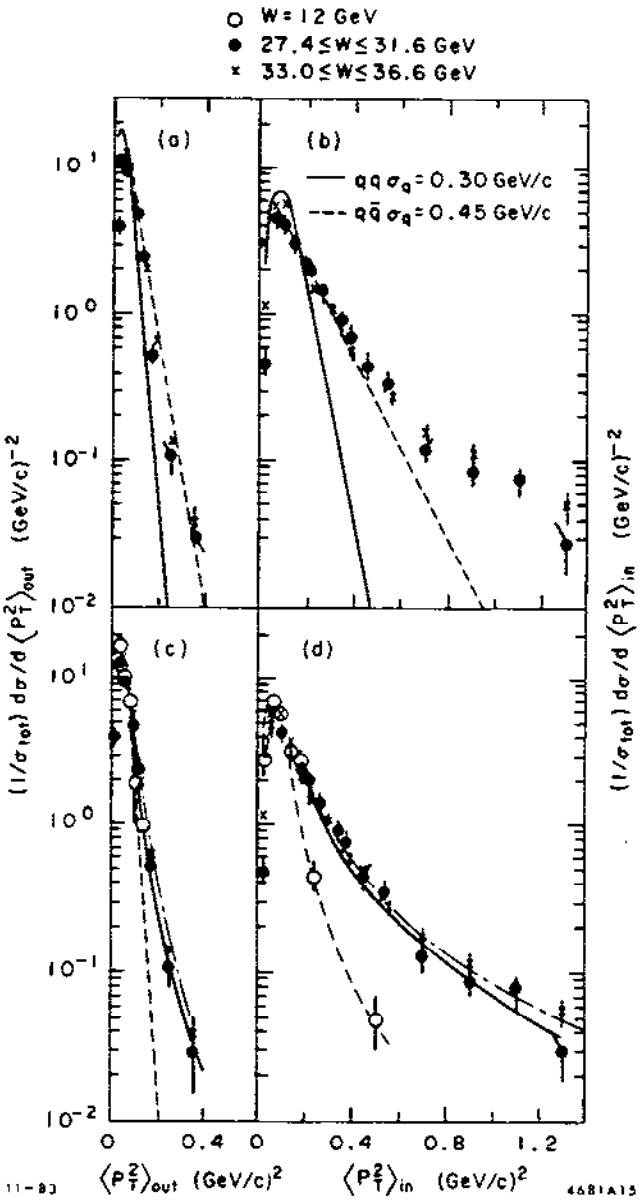
W = 12 GeV
27.4 ≤ W ≤ 31.6 GeV
33.0 ≤ W ≤ 36.6 GeV
(a)
(b)
(c)
(d)
qq σq = 0.30 GeV/c
qq̄ σq = 0.45 GeV/c
(1/σtot) dσ/d ⟨P²T⟩out (GeV/c)⁻²
(1/σtot) dσ/d ⟨P²T⟩in (GeV/c)⁻²
⟨P²T⟩out (GeV/c)²
⟨P²T⟩in (GeV/c)²
11-83
4681A15

Figure 15

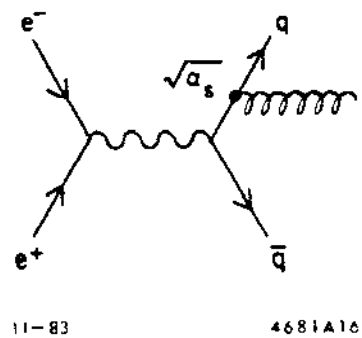

Figure 16

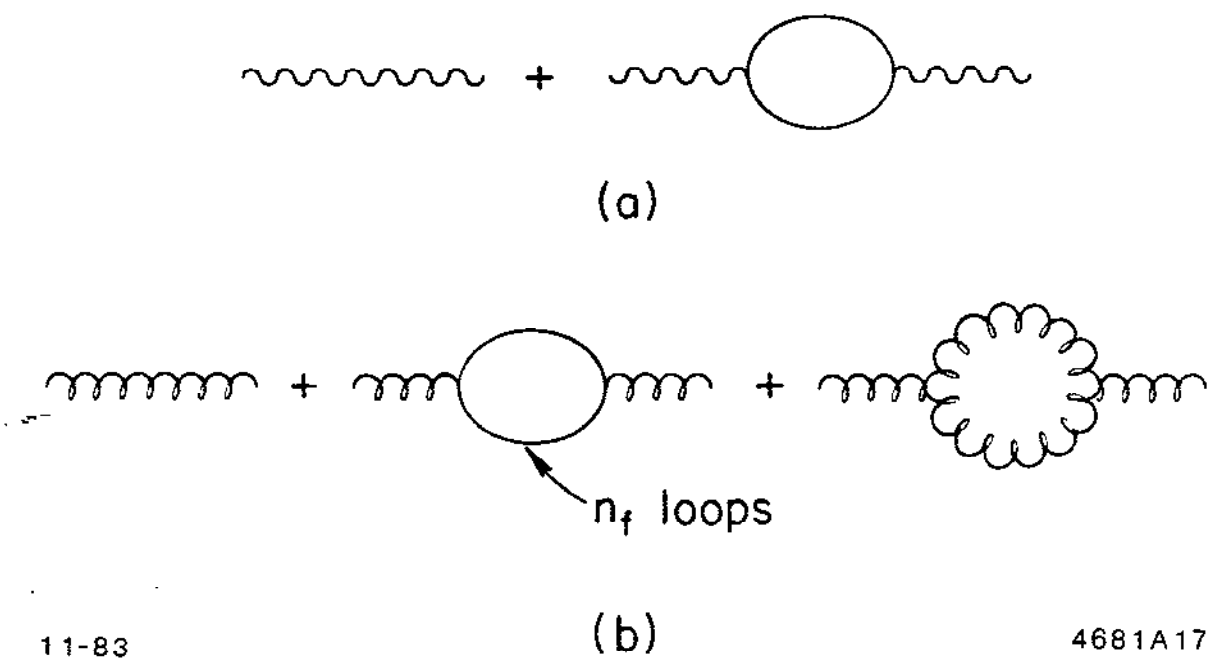

Figure 17

In this case the coupling constant **increases** with Q^2 and since $\alpha(\mu_0^2)$ is very small, the variation is quite small.* A similar analysis in QCD can be carried out provided the lowest order perturbation diagrams are all that need to be summed. In this case, a new diagram enters [see Figure 17(b)] because QCD is a non-Abelian theory so the gluons carry "color" charge and can couple to themselves (just as a photon couples to any charge carrier in QED). The calculation for the diagrams in Figure 17(b) yields a variation of $\alpha_s(Q^2)$ with Q^2 (using $N_c = 3$) given by

$$\alpha_s(Q^2) \sim \alpha_s(\mu_0^2)\left[\, 1 + \frac{\alpha_s(\mu_0^2}{12\pi}\,(2N_f - 33)\,\ell n\,\frac{Q^2}{\mu_0^2}\,\right] \tag{44}$$

which decreases with Q^2 provided $2N_f$ is less than 33. If Q^2 is sufficiently high, we expect α_s to be small enough for the perturbative calculation to be valid. This property — called asymptotic freedom — is crucial in this application, since without it, we would have no reason to believe that the addition of gluons would not make large changes in the behavior of $R(s)$. In this connection, it is important to keep in mind that the negative term in Equation (44) comes directly from the non-Abelian coupling (gluon self-coupling) diagrams.

The strong coupling constant variation is sometimes expressed in first order QCD as

$$\alpha_s(Q^2) = \frac{12\pi}{11N_c - 2N_f}\left[\ell n\,\frac{Q^2}{\Lambda^2}\right]^{-1} \tag{45}$$

But note that if $\alpha_s(Q_0^2)$ is known at some Q_0^2, then given N_c and N_f, we know α_s at all Q^2, thus we can solve for the first order Λ parameter. Using Equations (44) and (45) we find

$$\Lambda^2 = Q_0^2\, e^{-b/\alpha_s(Q_0^2)}$$

where (46)

$$b = \frac{12\pi}{11N_c - 2N_f}$$

In principle, one need never refer to Λ, however, since Equation (44) is just

$$\frac{\alpha_s(Q_0^2)}{\alpha_s(Q^2)} = \left[\,\frac{\alpha_s(Q_0^2)}{b}\;\ell n\,\frac{Q^2}{Q_0^2} + 1\,\right] \tag{47}$$

*For the interested reader, it is amusing to calculate the coupling constant α at the mass of the Z, which will convince you that even in QED the effect is important.

4.1 QCD AND OTHER MODIFICATIONS TO R

Within the framework of QCD, diagrams like that of Figure 16 can be included in the calculation of $R(s)$. The result will be of the form

$$R = 3 \sum e_q^2 \left\{ 1 + C_1 \frac{\alpha_s}{\pi} + C_2 \left(\frac{\alpha_s}{\pi} \right)^2 + \ldots \right\} \quad . \tag{48}$$

The coefficient C_1 is found to be 1 and the coefficient C_2 depends on the renormalization scheme used for the second order calculation.[14] Within the $\overline{MS}$ (minimal subtraction) scheme, the value of C_2 is

$$C_2 = 1.99 - 0.12\ N_f \quad . \tag{49}$$

Since these coefficients are reasonable small, and since as we see later, α_s is somewhere between 0.1 and 0.2, we have succeeded in adding the physics of three-jets without making too large a modification of R. In fact, we have done so well that the QCD modification is small compared to the experimental systematic errors! Table 3 shows recent measurements of R by a number of experimental groups. The weighted average value of R for data taken above 29 GeV is 3.95 ± 0.08 which yields a value for α_s between 0.27 and 0.16.

Table 3

Experimental Measurements of R

Experiment	$\sqrt{s}$ GeV	R	$\pm$	ΔR_{STAT}	$\pm$	ΔR_{SYST}
MARK J	12–36.7	3.84	$\pm$	0.05	$\pm$	0.22
TASSO	14–36.7	4.01	$\pm$	0.03	$\pm$	0.20
MARKII	29	3.90	$\pm$	0.05	$\pm$	0.25
MAC	29	3.93	$\pm$	0.04	$\pm$	0.20
JADE	30–36.7	3.93	$\pm$	0.03	$\pm$	0.09
TASSO	30–36.7	4.05	$\pm$	0.03	$\pm$	0.19

If we were to use a different second order subtraction scheme, for example the momentum space scheme where

$$C_2 = -2.19 + 0.16\ N_f \quad , \tag{50}$$

the same experimental measurements would yield α_s values between 0.39 and 0.19. Unfortunately we must conclude from this that present experimental and theoretical

uncertainties are too large to **determine** α_s from these measurements. Present experimental errors are also too large to see the expected variation in R (~ 0.03) over the range of available energies.

Even without these problems, there are additional things to consider before converting the measured value of R directly into a value of α_s using Equation (48). The first order QCD correction is approximately seven percent, weak interactions will contribute on the order of three percent corrections at these energies, QED radiative corrections are uncertain to an order of two percent, the variation of α_s with Q^2 is a one percent effect, and finally quark mass effects modify the value of R according to[15]

$$R = \frac{3}{2}\,\beta(3-\beta^2)\,e_Q^2\left\{1+\frac{4}{3}\,\alpha_s F(\beta)\right\} \tag{51}$$

where

$$F(\beta) = \frac{\pi}{2\beta} - \frac{3+\beta}{4}\left(\frac{\pi}{2} - \frac{3}{4\pi}\right) \quad .$$

While these factors are small near 29 GeV ($\sim 0.1\%$), they are not negligible near 10 GeV. Other effects may also be important in the 10 GeV range. We know for example that the cross-section exhibits considerable structure above the $c\bar{c}$ resonances and this may also be true above the $b\bar{b}$ family.

4.2 Back to Three-Jets

Assuming that we can isolate a sample of three-jet events and in some way measure the individual jet properties, let us see what we can learn about α_s and QCD. If the three jets have fractional energies $x_i = E_i/E_b$, and the angle between the gluon and one of the quarks is θ, as shown in Figure 18, at the parton level, the differential cross-section will be

$$\frac{d^2\sigma\,(3\,jet)}{dx_1\,dx_2} = \frac{2\alpha_s}{3\pi}\;\sigma\,(2\,jet)\;\frac{x_1^2+x_2^2}{(1-x_1)(1-x_2)} \tag{52}$$

where $x_1 + x_2 + x_3 = 2$.

Given the rough value of α_s determined before, we can see that roughly five to ten percent of the events should be planar three-jet events. The exact number will depend on the minimum gluon energy and angle with respect to a quark which gives an observable third jet. Obviously as $k = 2 - x_1 - x_2$ becomes small or as θ approaches zero, the event looks more and more like a two-jet event. In fact there is no clear dividing line between the two classes of events. In a way which is reminiscent of the soft photon problem in QED, some $q\bar{q}$ (soft glue) events are indistinguishable from 2 JETS and belong in the calculation of that cross-section.

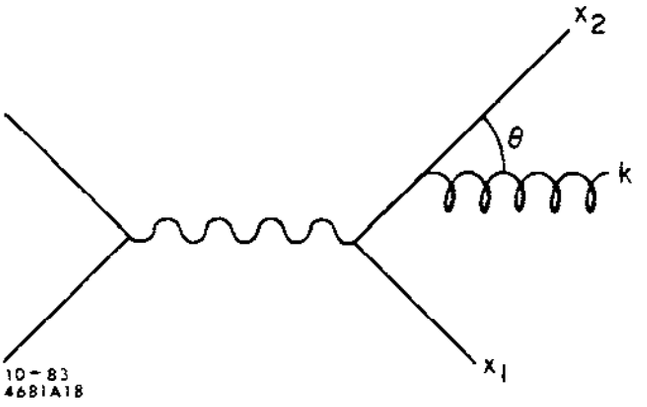

Figure 18

Experimentally, it is convenient to look for three-jets only in those events with a thrust [$T = \text{MAX}(x_1, x_2, x_3)$] of less than some maximum value, typically 0.9. That this does not completely cure the problem of ambiguities about whether the event has two or three jets is shown in Figure 19. A sample of three-jet events has been generated for $T_{\text{MAX}} = 0.95$. All other events are considered to have two-jet kinematics. At the parton level (solid curves) it is quite clear that there are a well-defined number of events with thrust less than 0.95 and hence a well-defined "3 JETS cross-section." However, when we consider the effect of fragmentation on the two-jet cross-section, it is clear that some of these events, when measured, will have thrust less than 0.95 and appear to be like three-jet events in that respect. As can be seen from the dotted curves in Figure 19, the tail of the two-jet distribution at small thrust is almost as large as the parton level three-jet contribution. Before we can use the thrust distribution to test QCD, we must be quite certain about the tail of the two-jet contributions.

4.3 GLUON SPIN

In discussing two jet events in e^+e^- annihilation, we found that the angular distribution of the jet (thrust) axis reflected the fact that the spin of the quarks was 1/2. We can apply the same principle to the three-jet case to determine the spin of the third jet. Experimentally it is easier to determine the axis of a jet than its total energy. Using energy and momentum conservation, the fractional energies of the three jets can be deduced from their relative angles using

$$x_i = \frac{2 \sin \theta_i}{\sin \theta_1 + \sin \theta_2 + \sin \theta_3} \quad . \tag{53}$$

The angular distributions of the jets relative to each other are determined by the spin of the jets; thus if the gluon (jet number 3) is a vector particle, the differential cross-section is given by Equation (52) namely

$$\text{Vector gluon :} \qquad \frac{d^2\sigma}{dx_1\, dx_2} = \frac{2\alpha_s}{3\pi}\, \sigma_0 \left\{ \frac{x_1^2 + x_2^2}{(1-x_1)(1-x_2)} + \begin{matrix} 1,\ 2,\ 3 \\ \text{cyclic} \\ \text{permutations} \end{matrix} \right\} . \tag{54}$$

For scalar gluons, the angular distributions are given by

$$\text{Scalar gluon :} \qquad \frac{d^2\sigma}{dx_1\, dx_2} = \frac{\tilde{\alpha}_s}{3\pi}\, \sigma_0 \left\{ \frac{x_3^2}{(1-x_1)(1-x_2)} + \begin{matrix} \text{cyclic} \\ \text{permutations} \end{matrix} \right\} \tag{55}$$

where $\tilde{\alpha}_s$ is some effective coupling constant for the scalar theory. Following the method of Ellis and Karliner,[16] the angular distributions can be simplified by looking for the angular distribution of x_2 and x_3 in the rest frame of x_1 as shown in Figure 20. The angle $\tilde{\theta}$ can be determined from the measured jet axes using

$$\cos \tilde{\theta} = \frac{x_2 - x_3}{x_1} = \frac{\sin \theta_2 - \sin \theta_3}{\sin \theta_1} \quad . \tag{56}$$

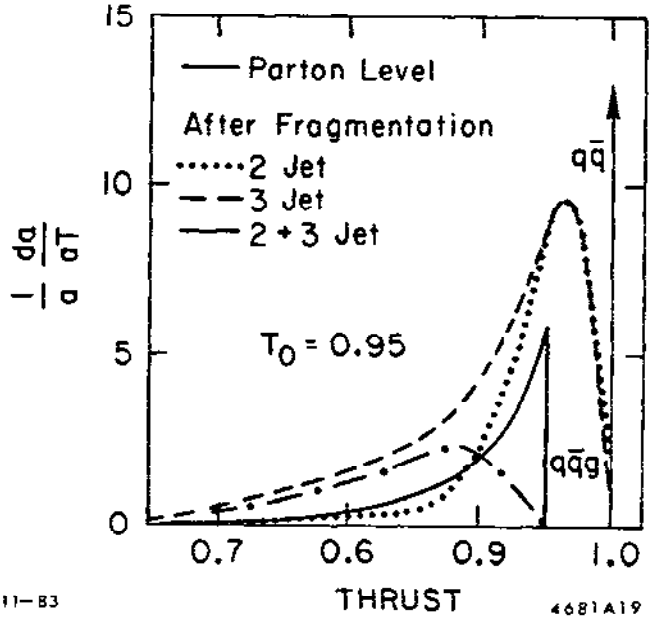
15
10
5
0
Parton Level
After Fragmentation
2 Jet
3 Jet
2 + 3 Jet
$T_0 = 0.95$
$q\bar{q}$
$q\bar{q}g$
$\frac{1}{\sigma}\frac{d\sigma}{dT}$
0.7
0.6
0.9
1.0
THRUST
11-83
4681A19

Figure 19

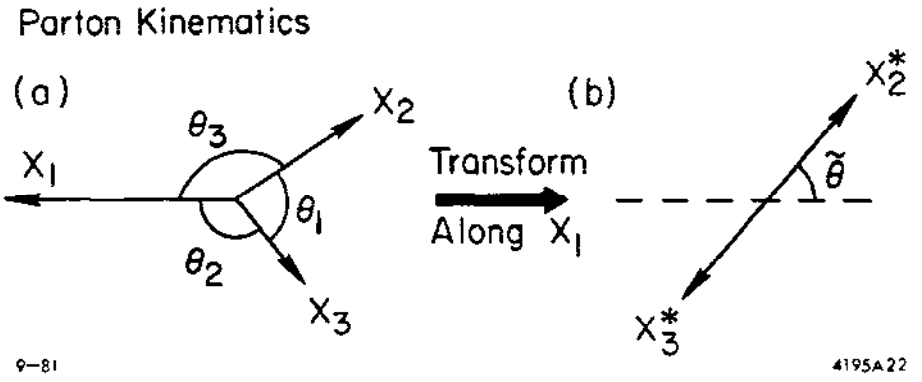
Parton Kinematics
(a)
X_1
X_2
X_3
θ_1
θ_2
θ_3
Transform
Along X_1
(b)
X_2^*
X_3^*
$\tilde{\theta}$
9-81
4195A22

Figure 20

The experimental data from the TASSO detector for energies above 25 GeV and event thrust (x_1) less than 0.9 is shown in Figure 21 and rules out the scalar hypothesis.

4.4 Determining α_s from the Ratio of Jet Cross-Sections

Naively, one would expect that Equation (52) would allow one to measure α_s from the ratio of jet cross-sections since

$$\frac{\sigma_{3\,\mathrm{JET}}}{\sigma_{2\,\mathrm{JET}}} \sim \alpha_s \qquad \text{and} \qquad \frac{\sigma_{4\,\mathrm{JET}}}{\sigma_{3\,\mathrm{JET}}} \sim \alpha_s \qquad \cdots$$

Of course, the gluon must have some minimum energy to be observable and since the energy spectrum for the gluons will be a bremsstrahlung spectrum

$$\frac{d\sigma}{dE\,d\theta} \sim \frac{\alpha_s}{k\theta} \quad , \tag{57}$$

we need to define a minimum angle θ_{MIN} and energy k_{MIN} above which events will be called three-jet events. Remember, however, that as Q^2 becomes small, α_s becomes larger. For soft and/or collinear gluons, the theory becomes nonperturbative and we do not know the form which corresponds to Equation (57). As shown in Figure 22, this means that we do not know the form of the cross-section below θ_{MIN}. The total two-jet and three-jet cross-sections are thus given by

$$\begin{aligned} \sigma_{2\,\mathrm{JET}} &\equiv \sigma_2 + \int_0^{E_{\mathrm{MIN}}} \int^{\theta_{\mathrm{MIN}}} \frac{d^2\sigma_3}{dE\,d\theta} \\ \sigma_{3\,\mathrm{JET}} &\equiv \int_{\theta_{\mathrm{MIN}}} \int_{E_{\mathrm{MIN}}} \frac{d^2\sigma_3}{dE\,d\theta} \quad . \end{aligned} \tag{58}$$

Note that at the parton level, the two-jet cross-section consists of two parts, the second of which we do not know how to evaluate.

Unfortunately, there is a second complication which comes from the fact that experiments do not see partons (quarks and gluons) directly, but see the hadrons which result from their fragmentation. If we start with an event which at the parton level has two-jets, then each of these jets will result in hadrons spread over some angular range as shown in Figure 23(a), both due to the finite resolution of the detection apparatus and the fragmentation process itself. As a result [Figure 23(b)], some of these events will result in configurations which have energy greater than E_{MIN} and angles greater than θ_{MIN}. The **detected** three-jet cross section is now

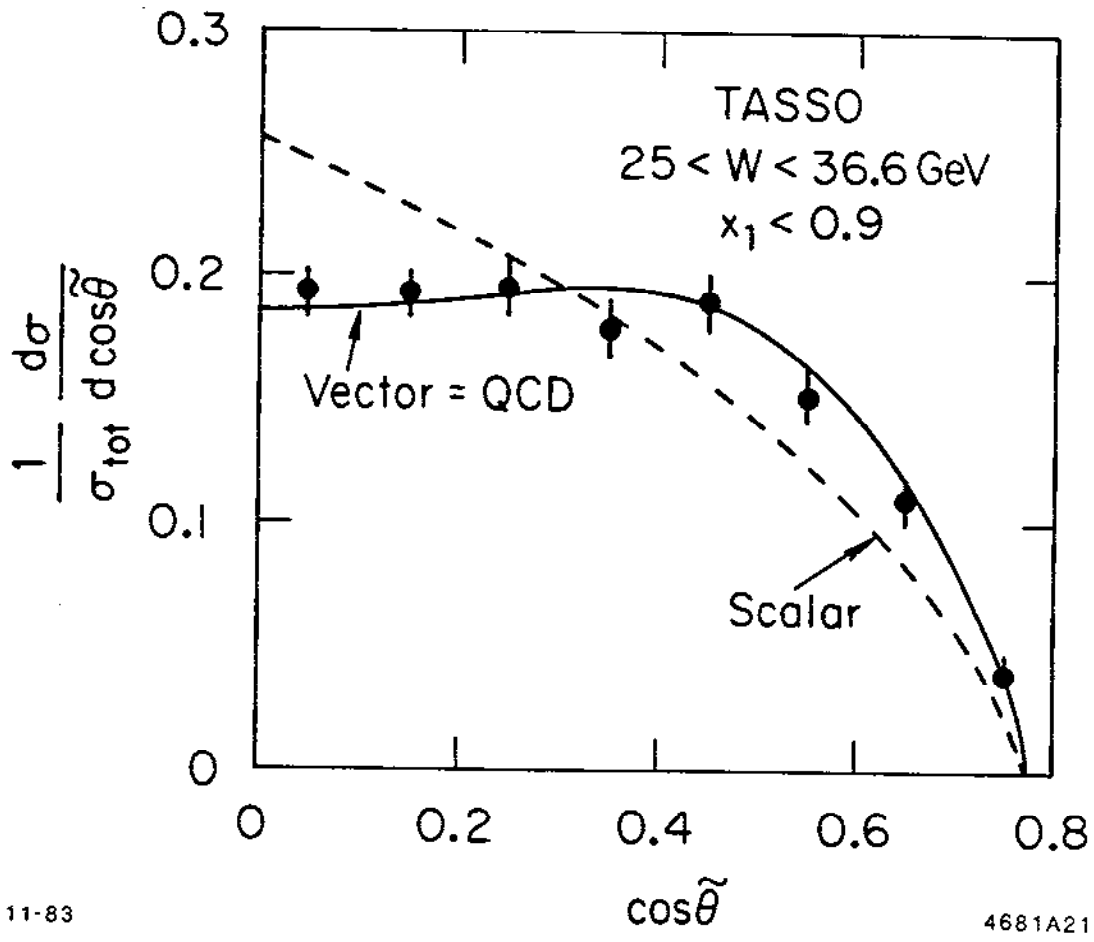
TASSO
25 < W < 36.6 GeV
$x_1 < 0.9$
Vector = QCD
Scalar
$\frac{1}{\sigma_{tot}} \frac{d\sigma}{d\cos\tilde{\theta}}$
$\cos\tilde{\theta}$
0.3
0.2
0.1
0
0
0.2
0.4
0.6
0.8
11-83
4681A21

Figure 21

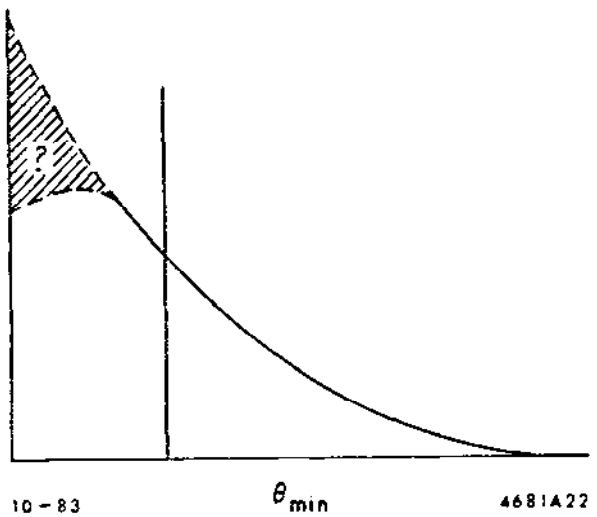

Figure 22

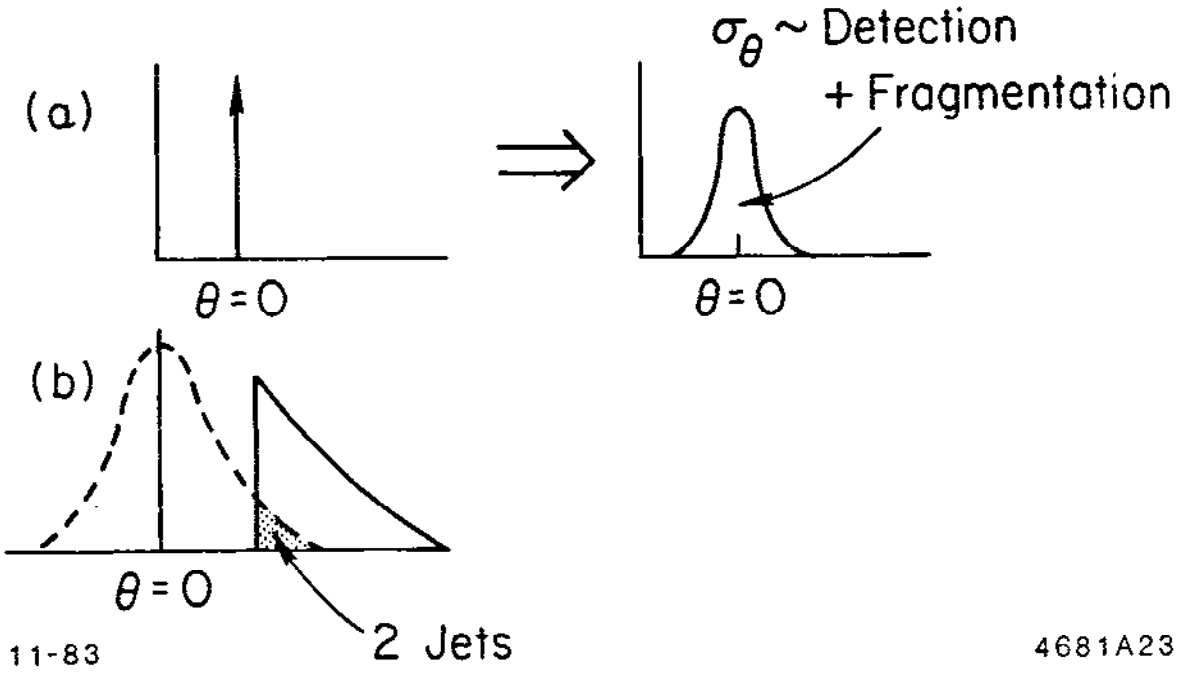

Figure 23

$$\sigma_{3\,\mathrm{JET\ DETECTED}} = (1-\epsilon)\,\sigma_{3\,\mathrm{JET}} + 2\ \mathrm{JET\ TAIL}$$

where ϵ is the fraction of three-jet events which as a result of detector resolution and fragmentation are detected as two-jet events even though at the parton level they might have satisfied the three-jet cuts for E_{MIN} and θ_{MIN}. One of the goals of the experimentalist is of course to design cuts which minimize these problems. This has to be done with the aid of a detailed model of the detector and the fragmentation process. One can typically reduce the contribution of two-parton events which are present in a three-jet sample so that if the efficiency for three-jet detection is such that approximately ten percent of the events are classified as three-jet events, the 2 JET contamination is approximately one percent of the total or ten percent of the 3 JET sample. This is sufficient to get a relatively clean sample of three-jet events for studying particle composition, angular distributions, et cetera. Different models of the fragmentation process, however, disagree about the magnitude of the second term in the two-jet cross-section [Equation (58)] and so as yet we cannot use the jet cross-section ratios to determine α_s precisely.

5. We Need a Fragmentation Model

It is clear from the preceding discussion that we need a rather detailed fragmentation model to use in extracting information from the data about QCD. Since these models are attempting to parameterize or describe the soft part of QCD which cannot be handled perturbatively, they are somewhat arbitrary. After discussing the more common models, we will return to look at the data and see how we can use the data to constrain the models.

There are at present three major classes of fragmentation models, each of which have been implemented in large Monte Carlo simulation programs for use in e^+e^- annihilation. The *Independent Fragmentation Model* considers the fragmentation process to be independent of the parton production process. In addition each parton fragments independently of the others. Hence quantum number conservation often has to be added in a somewhat *ad hoc* manner. The Hoyer, Ali and Feynman-Field Monte Carlos are all of this type. Figure 24(a) shows an example of this type of process; the fragmentation process may or may not be different for gluons and quarks. *String Models*, studied extensively by the Lund group, are based on the analogy between strong QCD and $1+1\,D$ QED. The fragmentation process results from $q\bar{q}$ production at breaks in a string (or color flux tube) extending between the partons [Figure 24(b)]. Thus fragmentation within three-parton events may be different from

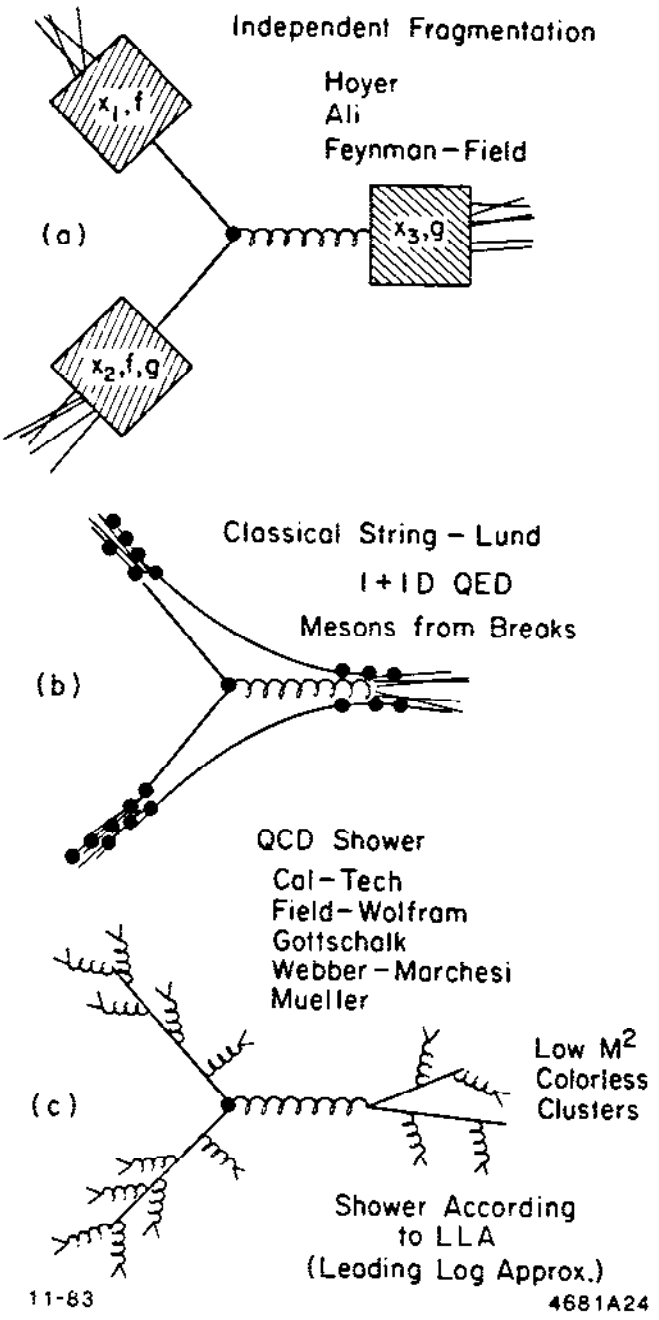
Independent Fragmentation
Hoyer
Ali
Feynman – Field
(a)
x_1, f
x_2, f, g
x_3, g
Classical String – Lund
1 + 1 D QED
Mesons from Breaks
(b)
QCD Shower
Cal – Tech
Field – Wolfram
Gottschalk
Webber – Marchesi
Mueller
(c)
Low M^2
Colorless
Clusters
Shower According
to LLA
(Leading Log Approx.)
11-83
4681A24

Figure 24

that in two-parton events, and the partons do not fragment independently. Finally, QCD shower Monte Carlos (Field-Wolfram, Gottschalk, Webber-Marchesi, Mueller) generate soft hadronization using a cascade approach which attempts to generate a shower of partons using leading log QCD approximations at each step in the shower [Figure 24(c)].

Each Monte Carlo must first decide how many partons to produce using first or second order QCD matrix elements or possibly leading log approximations. These partons must then be converted into hadrons with an independent/string/shower algorithm which accounts for quantum number conservation. These primary hadrons must then decay into secondary hadrons whenever they are unstable. In some cases these decays are quite straightforward, the angular distributions and branching ratios being taken from Particle Data Group compilations. In other cases, such as the decays of heavy mesons (B, B^*, $F\ldots$) or charmed baryons, the branching ratios can vary from model to model. To complicate the situation further, many groups replace the "standard" decay routines with their own favorite secondary decays and branching ratios! Finally, the response of the detector to the resulting mesons and baryons must be simulated along with the effect of analysis and physics cuts.

5.1 Independent Fragmentation Model

The fragmentation of a quark (or gluon) in this model is defined primarily by the splitting function $f(z)$ which determines the probability that a quark emits a hadron with fractional energy z. As shown in Figure 25, if the original quark has four-momentum, $\not{P}$ then each splitting results in a hadron with four-momentum $z\not{P}$ and a residual quark with $(1-z)\not{P}$. The earliest form of the splitting function used in these models was

$$f(z) = 1 - a_F + 3a_F(1-z)^2 \tag{59}$$

where

$$z = \frac{(p_{\parallel} + E)_h}{(p_{\parallel} + E)_q} \quad .$$

Successive applications of this simple splitting function lead to the final jet, and one can see that the inclusive momentum spectrum of **primary** hadrons is completely determined by $f(z)$. Corrections for secondary decays of course have to be made when comparing to observed distributions. It is an interesting exercise to show that without

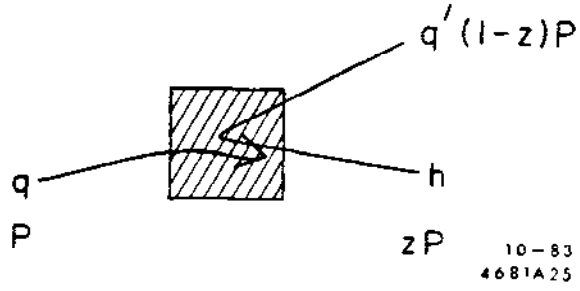

Figure 25

secondary decays, the successive application of $f(z)$ results in an integral equation for the resultant hadron spectrum which is just

$$D(z) = f(z) + \int_z^1 \frac{dz'}{z'} \, f(1-z') \, D\left(\frac{z}{z'}\right) \tag{60}$$

where the second term is the feed-down contribution. Furthermore, it is possible to show that

$$D(z) = \frac{f(z)}{z}$$

is a solution for all $f(z)$ of the form

$$f(z) = (m+1)(1-z)^m \quad . \tag{61}$$

The important point to remember is that the hadron spectrum D(z) is an important constraint on the form of f(z).

As we discussed before, the behavior of the hadronic events is characterized by severly limited transverse momentum. This is incorporated into the model by introducing a $q_\perp$ for the hadron relative to the quark axis in each splitting. The probability distribution is given by

$$\frac{dN}{dq_\perp^2} \sim e^{-q_\perp^2/2\sigma_q} \tag{62}$$

with the $q_\perp$ of the hadron being balanced at each splitting by the $q_\perp$ of the recoil quark q' as shown in Figure 26. The spin of the produced hadron is determined at each branching by the ratio of vector (ρ, K^*, ...) to pseudoscalar (π, K, ...) production via the internal parameter

$$\frac{P}{P+V}$$

The final state multiplicity is very sensitive to this parameter because of the difference between vector and pseudoscalar meson masses and decay multiplicities.

Looking at the branching process in more detail, we can see that the type of hadron produced will depend on the initial quark and the choice of final quark q' as in Figure 27. The meson production results from a series of $q\bar{q}$ pair productions. The type of pair produced is chosen with

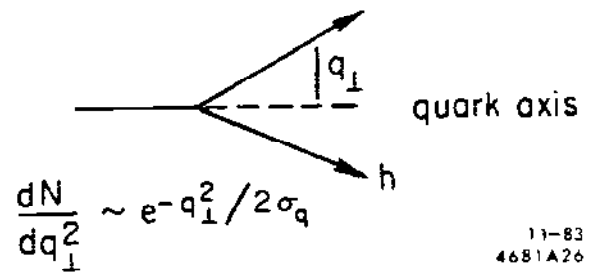
$q_\perp$
quark axis
h
$\frac{dN}{dq_\perp^2} \sim e^{-q_\perp^2/2\sigma_q}$
11-83
4681A26

Figure 26

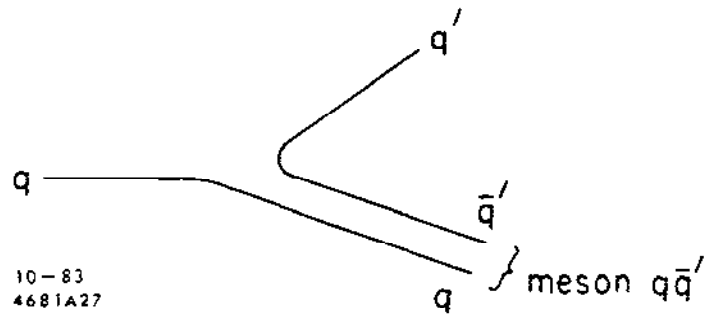

Figure 27

$$u\bar{u} : d\bar{d} : s\bar{s} = a : a : b \tag{63}$$

with $b < a$ to account for the phase space suppression due to the heavier s quark mass. The a/b ratio will determine the $\rho : K^*$ ratio as well as the $\pi : K$ ratio in the final state. As shown in Figure 28, if one starts from a two-parton state, the primary $q\bar{q}$ pair will be $u : c : d : s : b = 4 : 4 : 1 : 1 : 1$. Charmed or bottom mesons or baryons are expected to contain the primary quark, and one pair joins the last q' of the q fragmentation with the last $\bar{q}'$ of the $\bar{q}$ fragmentation.

In principle, the fragmentation of a gluon can be described by a similar process, but first we need to convert each gluon into a quark-antiquark pair. In the Hoyer Monte Carlo, all of the momentum of the gluon is carried by one of these quarks. As a result, gluon fragmentation is indistinguishable from quark fragmentation. In the Ali model, the gluon is split into a quark pair using the Altarelli-Parisi splitting function for gluons:

$$f_g(z) = z^2 + (1-z)^2 \quad . \tag{64}$$

As discussed before for quark jets, $f(z)$ will determine the momentum spectrum of hadrons within the gluon jet.

In the case of heavy meson production, the heavy quark tends to carry away a large fraction of the momentum. Thus the fragmentation function will tend to peak more strongly for heavier quarks. In addition, if heavy quark pair production is strongly suppressed, the heavy meson will always contain the primary quark and hence there will be no feed-down contribution as in Equation (60). The form of the fragmentation function used is

$$D(z) = \frac{k}{z\left(1 - \frac{1}{z} - \frac{\epsilon}{1-z}\right)^2} \quad . \tag{65}$$

The heavier the quark, the smaller the value of ϵ. The constants can be determined from measurements of inclusive D and B meson production.

Baryon production does not fit easily into branching processes of the type shown in Figures 27 and 28, and must be put in phenomenologically. The observed proton fractions in the final states can be roughly explained if there is a probability of order ten percent of producing a diquark-antidiquark pair at each branching in addition to the process in Equation (63). If this is indeed the production mechanism for baryons, we might expect significant $p_\perp$ correlations between baryon pairs[17] and we would also expect baryons to be correlated in rapidity and probably that baryon-antibaryon pairs would tend to lie in the same jet due to local compensation of baryon number.

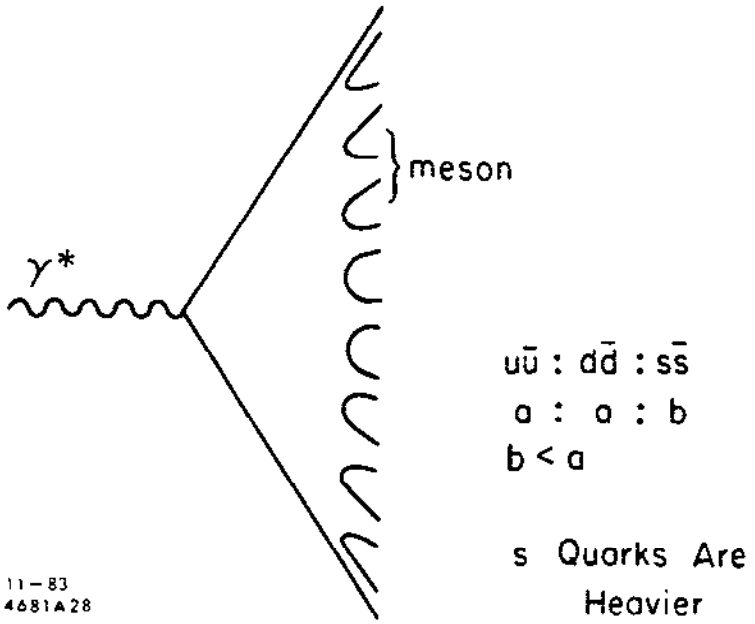

Figure 28

Most of the independent fragmentation models have now been modified to include diagrams arising from higher order corrections in QCD. Figure 29 shows the type of diagrams considered. The earliest Hoyer and Ali models included only diagrams up to order α_s with two and three jets. Subsequent versions of the Ali model included the order α_s^2–four-jet contributions, but did not include virtual corrections to the three-jet processes. The reason the latter processes are difficult to include is that the virtual three-jet corrections cancel divergences in the four-jet processes when one of the four-jets becomes soft. In order to do this properly, one must have a criterion for deciding when a four-jet event contains a parton which is soft enough to make it look like a three-jet event. An event which looks like Figure 30(a) could arise from a diagram like that shown in Figure 30(b). In this case, we can classify the event as a three-jet event provided the invariant mass of the soft parton with the nearest jet is small enough.

Two calculations of the four-jet corrections to the three-jet cross-section including virtual corrections originally yielded quite different results. In the first approach,[18] a small invariant mass cut ($M_{ij} \gtrsim 0.1$ GeV) was used and predicted large corrections to the three-jet fraction. A calculation using a larger cutoff[19] ($M_{ij} \gtrsim 5.0$ GeV) gave a ten to twenty percent correction. The discrepancy has been studied by Gottschalk[20] in terms of the variable

$$y = \frac{M_{ij}^2}{s} \quad . \tag{66}$$

In the ERT calculation, the cutoff invariant mass corresponds to a y value of 10^{-5} while in the FKSS approach, the cutoff is approximately 10^{-2}. As a function of y, Figure 31 shows that the four- and three-jet cross-sections are both positive only for y values greater that 0.03. In addition, requiring the four-jet contribution to be positive for thrust values less than 0.9 requires a y value of approximately $y \gtrsim 0.04$ (Figure 32).

The total cross-section for hadron production is given by

$$\sigma_{\rm TOT} = \sigma_0 \left[1 + \frac{\alpha_s(Q^2)}{\pi} + (1.98 - .115\, N_f)\, \frac{\alpha_s^2(Q^2)}{\pi^2} \right] \tag{67}$$

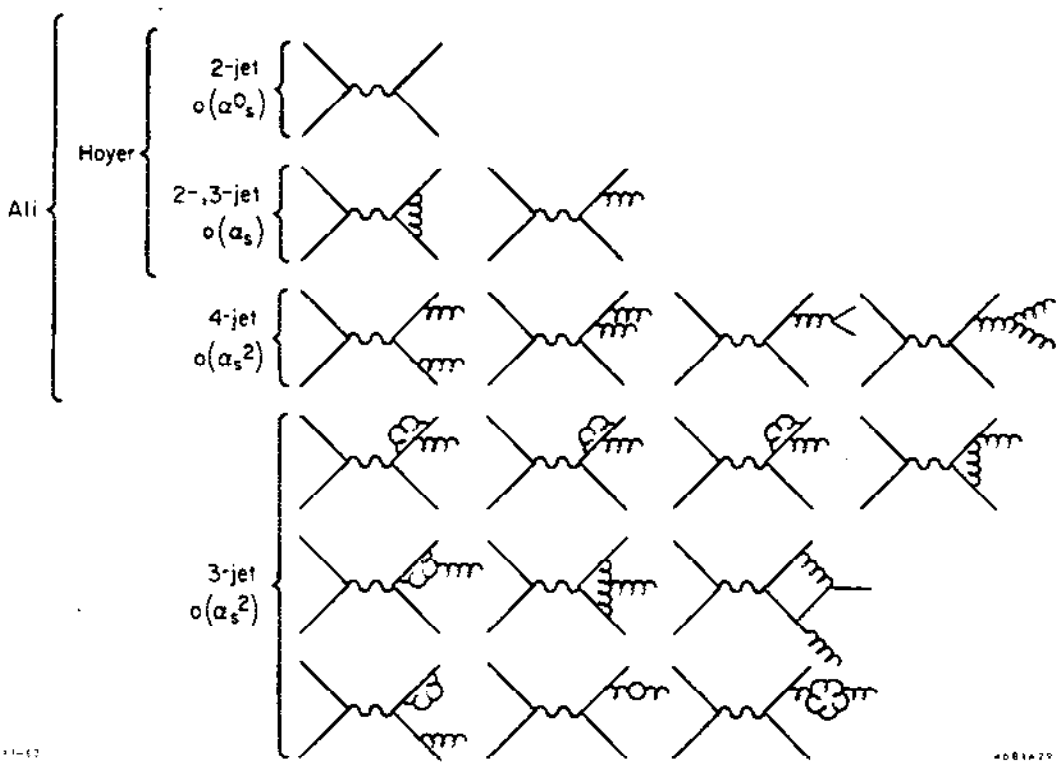

Figure 29

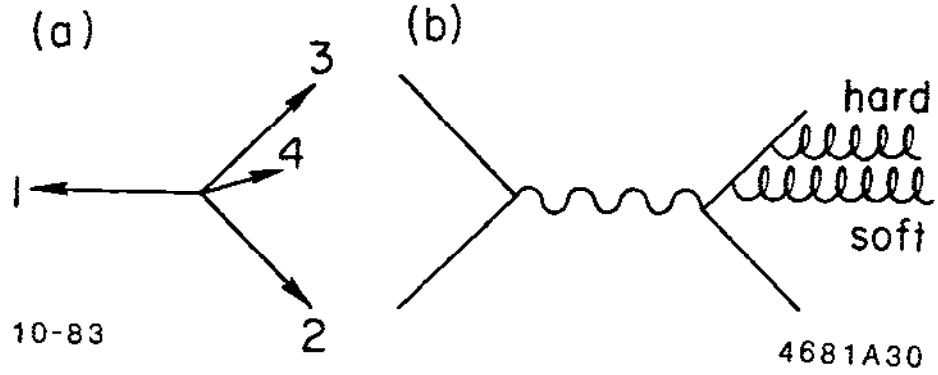

Figure 30

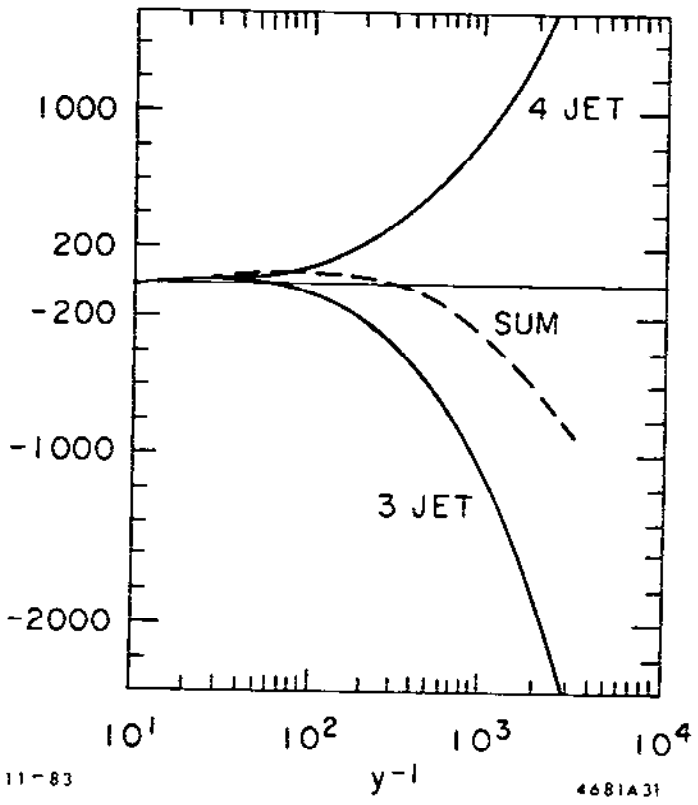
1000
200
-200
-1000
-2000
4 JET
SUM
3 JET
10^1
10^2
10^3
10^4
y-1
11-83
4681A31

Figure 31

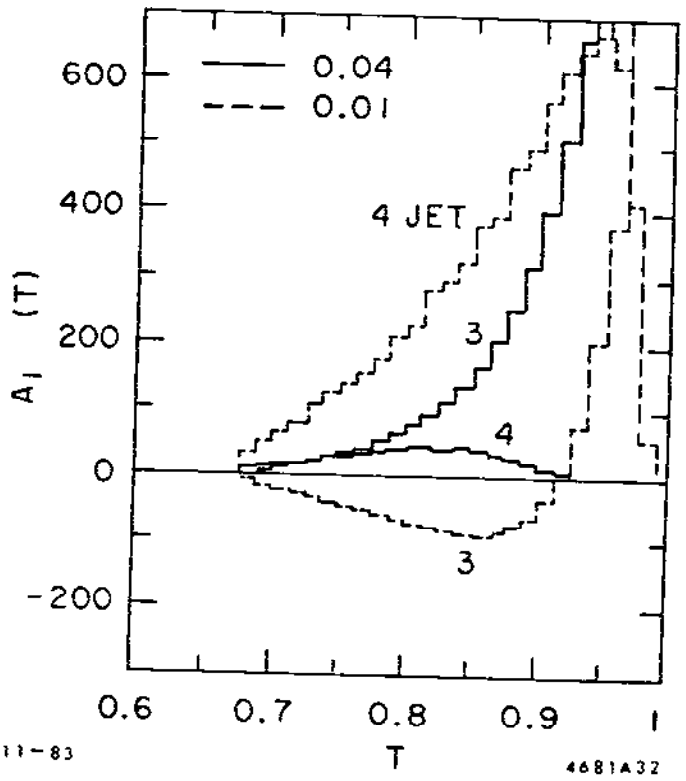
0.04
0.01
600
400
200
0
-200
4 JET
3
4
3
A_1 (T)
0.6
0.7
0.8
0.9
1
T
11-83
4681A32

Figure 32

where

$$\sigma_0 = \frac{11}{3}\,\frac{4\pi\alpha^2}{3s}$$

Because of the physical processes involved in fragmentation, three-jet events are indistinguishable from two-jets when the event thrust is greater than ~ 0.95 and four-jets become indistinguishable from three-jets for acoplanarity less than ~ 0.05, thus the observed three- and four-jet cross-sections must be defined as

$$\begin{aligned}\sigma_{3\,\mathrm{JET}} &= \int_{2/3}^{T_{\mathrm{MAX}}} dT\,\frac{d\sigma}{dT}\,(q\bar{q}g)\\ \sigma_{4\,\mathrm{JET}} &= \int_{A_{\mathrm{MIN}}}^{1} dA\,\frac{d\sigma}{dA}\,(q\bar{q}gg + q\bar{q}q\bar{q})\end{aligned} \tag{68}$$

where, for example[21]

$$\frac{d\sigma}{dT}\,(q\bar{q}g) = \frac{2}{3}\,\frac{\alpha_s}{\pi}\,\sigma_0\left[\frac{2(3T^2-3T-2)}{T(1-T)}\,\ell n\left(\frac{2T-1}{1-T}\right) - \frac{3(3T-2)(2-T)}{1-T}\right] \tag{69}$$

5.2 The String-Lund Model

In the previous model, a $q\bar{q}$ pair was produced and some time later we imagine that the two quarks are moving apart and that eventually they fragment independently. However, this model violates several things which we know about quarks. Quarks carry color, and this color charge leads to the strong force which binds quarks together to form mesons. From potential models of $q\bar{q}$ bound states, we find that this force is almost constant as a function of the separation between the quarks. This leads to a potential energy between two moving quarks which increases as

$$\begin{aligned}E &\sim Kd\\ K &\sim 1\,\mathrm{GeV/fm} = 0.2\,\mathrm{GeV}^2\end{aligned} \tag{70}$$

where d is the separation between the two quarks. At some point, we will have an energy larger than the mass of two light quarks, and we could have $q\bar{q}$ pair production from the field between the original pair. Schwinger[22] has shown that the behavior of 3+1 dimensional QCD is very similar to that of 1 + 1 QED in that the force leads to the formulation of a color flux tube with constant energy per unit length between the

$q\bar{q}$ pair. If the separation is large enough, this flux tube (or string in 1 + 1 dimensions) will break as shown in Figure 33 leading eventually to the formation of mesons.

This behavior in 1 + 1 dimensions is often depicted by a graph of t versus x as shown in Figure 34. Lines of constant proper time will be hyperbolas in this plot, and the velocity of a quark or meson will be inversely proportional to the slope of its trajectory in the plane. If a string breaks at two places, A and B as in Figure 33, and if the distance between points A and B satisfies

$$(x_A - x_B)^2 - (t_A - t_B)^2 > \frac{m^2}{K^2} \tag{71}$$

a meson can be produced. The fragmentation process generates many such mesons with the slowest mesons being produced first in contrast to the procedure used in the independent models where fragmentation starts with the fastest (primary) quarks. For this reason, this is called an "inside out cascade."

If each meson carries away a random fraction of the energy remaining in a string segment, the longitudinal fragmentation function will be $f(z) = 1$, but this is modified in QCD by the suppression of high z hadrons due to collinear gluon emission and leads to the effective form

$$\begin{aligned} f(z) &= (1+c)(1-z)^c \\ c &= \frac{2}{3}\,\frac{12}{33-2N_f}\left(\ell n\ell n\,\frac{M^2_{\text{upper}}}{\Lambda^2} - \ell n\ell n\,\frac{M^2_{\text{lower}}}{\Lambda^2}\right) \end{aligned} \tag{72}$$

where M^2_{upper} is the invariant mass above which gluons are considered separately and M^2_{lower} is a typical meson mass square. In practice, the c parameters are left as free parameters to be adjusted for each quark type, and are approximately as shown in Table 4.[23]

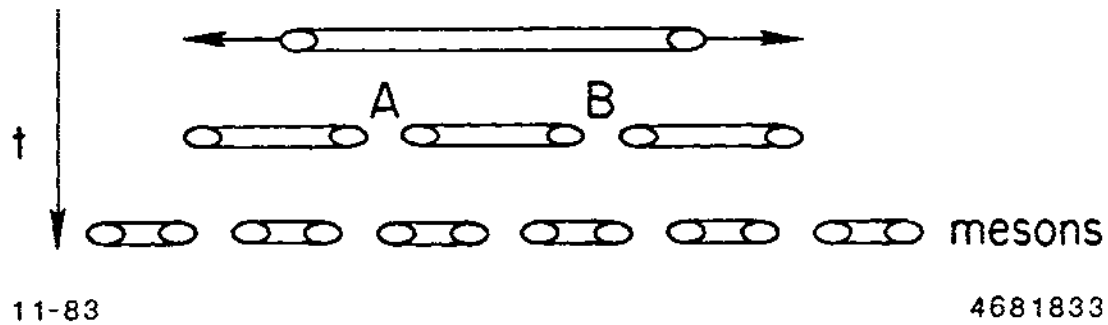

Figure 33

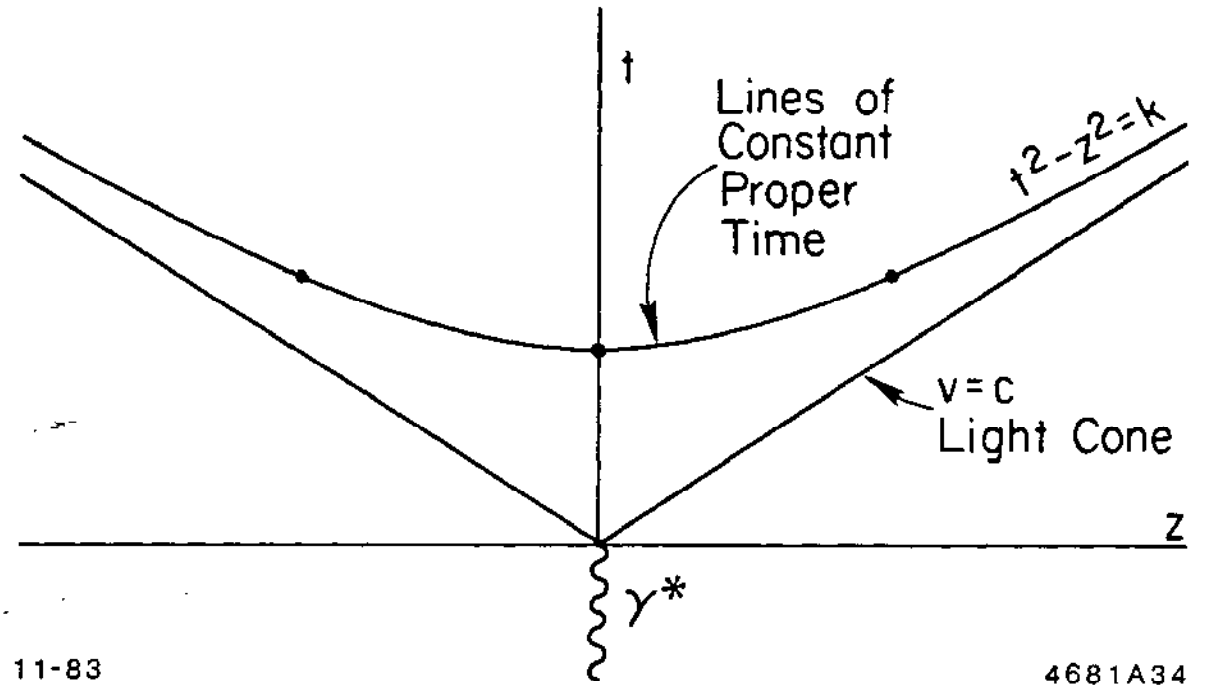
t
Lines of
Constant
Proper
Time
$t^2-z^2=k$
v=c
Light Cone
z
γ^*
11-83
4681A34

Figure 34

Table 4

Lund Model fragmentation parameters $f(z) = (1+c)(1-z)^c$					
quark	u	d	s	c	b
c	0.5	0.5	0.35	0.15	0.05

Finite meson mass and transverse momentum relative to the flux tube axis can be treated as a tunneling process and lead to production probabilities of the form

$$e^{-\pi(m^2+p_\perp^2)/K} \quad . \tag{73}$$

As a result, heavy quark pair production is suppressed in the ratio

$$u : d : s : c = 1 : 1 : 0.3 : 10^{-11} \quad ,$$

and all mesons have the same $p_\perp$ spectra independent of their flavor content.

Hard gluon emission is added to the model with probabilities taken from perturbative QCD to order α_s. For a three-parton configuration (Figure 35), the string is stretched from quark to gluon to antiquark. The gluon energy is shared equally between two string segments and thus if the number of particles produced per unit rapidity is a fundamental property of the string (or the color flux tube), the gluon jet will be softer than a quark jet. We would expect to find

$$\frac{dN}{dy}\Big\|_{\text{gluon}} \simeq 2\,\frac{dN}{dy}\Big\|_{\text{quark}} \tag{74}$$

but this effect may be moderated by finite mass effects and the lower mean energy of the gluon jet. This prediction is quite similar to the QCD prediction

$$\langle n\rangle_{\text{glue}} \simeq \frac{9}{4}\,\langle n\rangle_{\text{quark}} \tag{75}$$

where the 9/4 comes from the color factor

$$\frac{2n_c^2}{n_c^2-1} \quad . \tag{76}$$

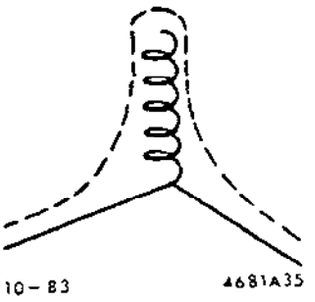

Figure 35

Since particle production occurs along the string, there may be fewer particles produced in the angular region between the q and the $\bar{q}$ than between the quarks and the gluon.[24]

The use of the tunneling hypothesis for quark mass effects has the interesting consequence that flavor production ratios, for example — the K/π ratio, are completely determined by the vertex weighting factor for each string break

$$\frac{(K\tau)^2}{(K\tau)^2 + m_t^2} \quad , \quad m_t^2 = m^2 + p_\perp^2 \quad . \tag{77}$$

All particle and flavor dependent mass effects should result from this simple factor. The model could of course be extended if necessary to include flavor dependent factors other than those predicted by mass dependent suppression of the tunneling probability.

Baryon production is introduced into the model by allowing the string to break into diquark-antidiquark pairs with an adjustable parameter fixed by the proton fraction in the final states. This is similar to what is done in the independent fragmentation models except that again production ratios for different types of baryons (ρ, Λ, Σ ...) are related in a definite way by the tunneling suppression factors.

Inclusion of higher order QCD effects in the string model raises several interesting questions. In the case of a $q\bar{q}g$ event, there is only one way to stretch the string between the q and the $\bar{q}$. However, with two gluons, there are two possibilities. The "correct" configuration can be chosen provided the gluons do not have the same color and provided the colors of the quarks are known. This requires a modification of the α_s^2 QCD matrix elements.[23,18]

Gluon jets produced using the string fragmentation picture tend to be softer than those produced by the independent fragmentation models, so that with a fixed set of analysis cuts, some three-jet events in the string picture will be lost into the two-jet sample. Qualitatively, this requires an increase in the effective value of α_s in order to produce the same number of observed three-jet events. As will be seen later, this type of effect makes it difficult to determine α_s in a model independent or fragmentation independent way.

5.3 CASCADE MODELS

Cascade models differ from the previous two models in two important ways. First, the evolution of the event is followed using leading log perturbative QCD until there are large numbers of partons in the final state. Soft gluon contributions are eliminated by requiring the parent parton in a branching to have a minimum invariant mass, typically a few GeV. Second, before these partons are converted into hadrons, preconfinement takes over, i.e., as shown in Figure 36, groups of partons combine to form color singlet clusters. This use of preconfinement means that color screening occurs before hadronization. The actual hadronization process must be parameterized from low energy data in terms of the decay of these clusters into smaller mass subclusters.

The joining of various parts of the parton shower together into colorless groups before hadronization is analogous to a model with many strings. The emphasis, unlike the independent fragmentation model, is on incorporating the strong color force as a fundamental feature of the model so that hadronization can be described in terms of the behavior of hadrons and not in terms of the fragmentation functions of colored quarks and gluons. Unlike the string model which generates hadrons from breaks in the string, the hadrons in this model are formed from the combination of leading log QCD showers and low mass hadronization. Perhaps in the future, we will be able to show that these two pictures are equivalent.

6. Can We Measure α_s from Jet Properties?

We now would like to return to the question of measuring the strong coupling constant α_s from properties of the jets observed in the final states. In the earliest measurements (1979-1980) there were several groups with of order 1000 events above $\sqrt{s} = 30$ GeV and there was reasonable agreement using lowest order QCD independent fragmentation models that α_s was approximately 0.17. Table 5 shows the results of these measurements. The MARK J group adjusted the transverse momentum fragmentation parameter σ_q and the coupling constant α_s to fit the oblateness and minor

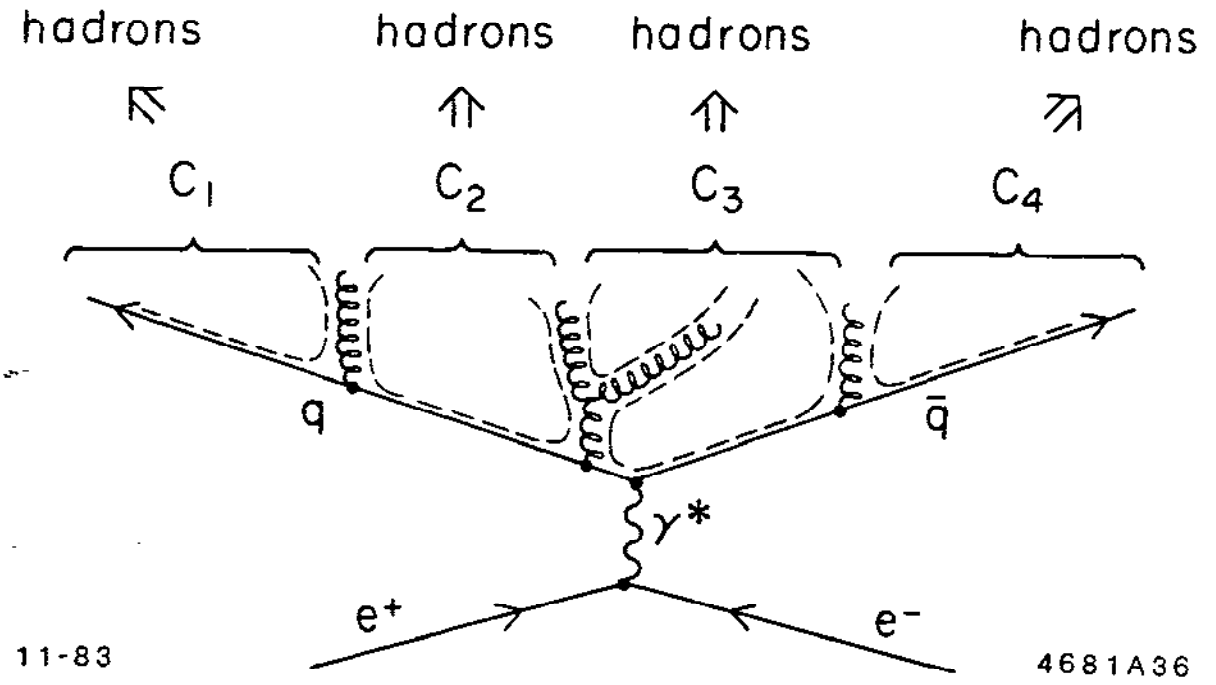
hadrons
hadrons
hadrons
hadrons
C1
C2
C3
C4
q
q̄
γ*
e+
e−
11-83
4681A36

Figure 36

Table 5

Results on α_s (1979/80)					
	Distributions Fitted	Fit Parameter	Model	Higher Orders	α_s ($\pm$ stat $\pm$ syst)
MARK J	0, Minor	σ_q, α_s	Ali	some $O(\alpha_s^2)$	$0.19 \pm 0.02 \pm 0.04$
TASSO	$\frac{dN}{dx}$, p_{out}^2 ,	a_F , σ_q	Hoyer	$O(\alpha_s)$	$0.19 \pm 0.02 \pm 0.03$
	S, A	$\frac{P}{P+V}$, α_s			
			Ali	some $O(\alpha_s^2)$	$0.17 \pm 0.02 \pm 0.04$
JADE	$\frac{dN}{dx}$, p_{out}^2 ,	a_F , σ_q	Hoyer	$O(\alpha_s)$	$0.18 \pm 0.03 \pm 0.03$
	S, A	$\frac{P}{P+V}$, α_s			
PLUTO	Number of 3-Cluster Events, x_1	α_s	Hoyer	$O(\alpha_s)$	$0.15 \pm 0.03 \pm 0.02$

axis distributions. The TASSO and JADE groups in addition varied the vector fractions and longitudinal fragmentation and fitted the thrust distributions, the mean transverse momentum out of the plane, the sphericity and the aplanarity. The PLUTO group used a similar method to fit α_s as a function of the number of three-cluster events and the thrust distribution in these events.

The first group to make extensive use of the string model, however, found substantially higher values for α_s.[25] Using five different methods, they found as shown in Table 6 that while they agreed with previous determinations using independent models, the string picture required values of α_s which were higher by ~ 0.08. This could be traced to the tendency of the string model to produce softer fragmentation in the

Table 6

CELLO (1982) $O(\alpha_s)$		
Distribution Fitted	Hoyer Independent Jets	Lund Model String Picture
$N(S > 0.25, A < 0.1)$	$\alpha_s = 0.19 \pm 0.03$	0.28 ± 0.045
$N(O > 0.2)$	$\alpha_s = 0.19 \pm 0.02$	0.26 ± 0.040
N (3clusters)	$\alpha_s = 0.145 \pm 0.020$	0.235 ± 0.025
dN/dX_1	$\alpha_s = 0.155 \pm 0.015$	0.235 ± 0.025
Energy − Energy Correlation	$\alpha_s = 0.150 \pm 0.020$	0.25 ± 0.04

three-parton final states. These results disagree with a similar determination by the JADE group which fits the number of three-cluster events and the thrust distributions and finds $\alpha_s = 0.20 \pm 0.015 \pm 0.03$ for **both** models.[26]

While the discrepancy is still not resolved, part of the problem may lie in the fact that the CELLO fits using the Hoyer model are not in good agreement with the data for both the thrust distribution and the $p_\perp$ distribution as shown in Figure 37. Clearly it is important to optimize all of the parameters in each of the models to give the best fit to the data before comparing values of α_s. The TASSO group has made a comparison of this type. They modify the longitudinal fragmentation function in the independent fragmentation model which was originally of the form

$$f(z) = 1 - a + 3a(1 - z)^2 \tag{78}$$

to be of a form similar to that used in the string models, namely

$$f(z) = (1 + a_L)(1 - z)^{a_L} \tag{79}$$

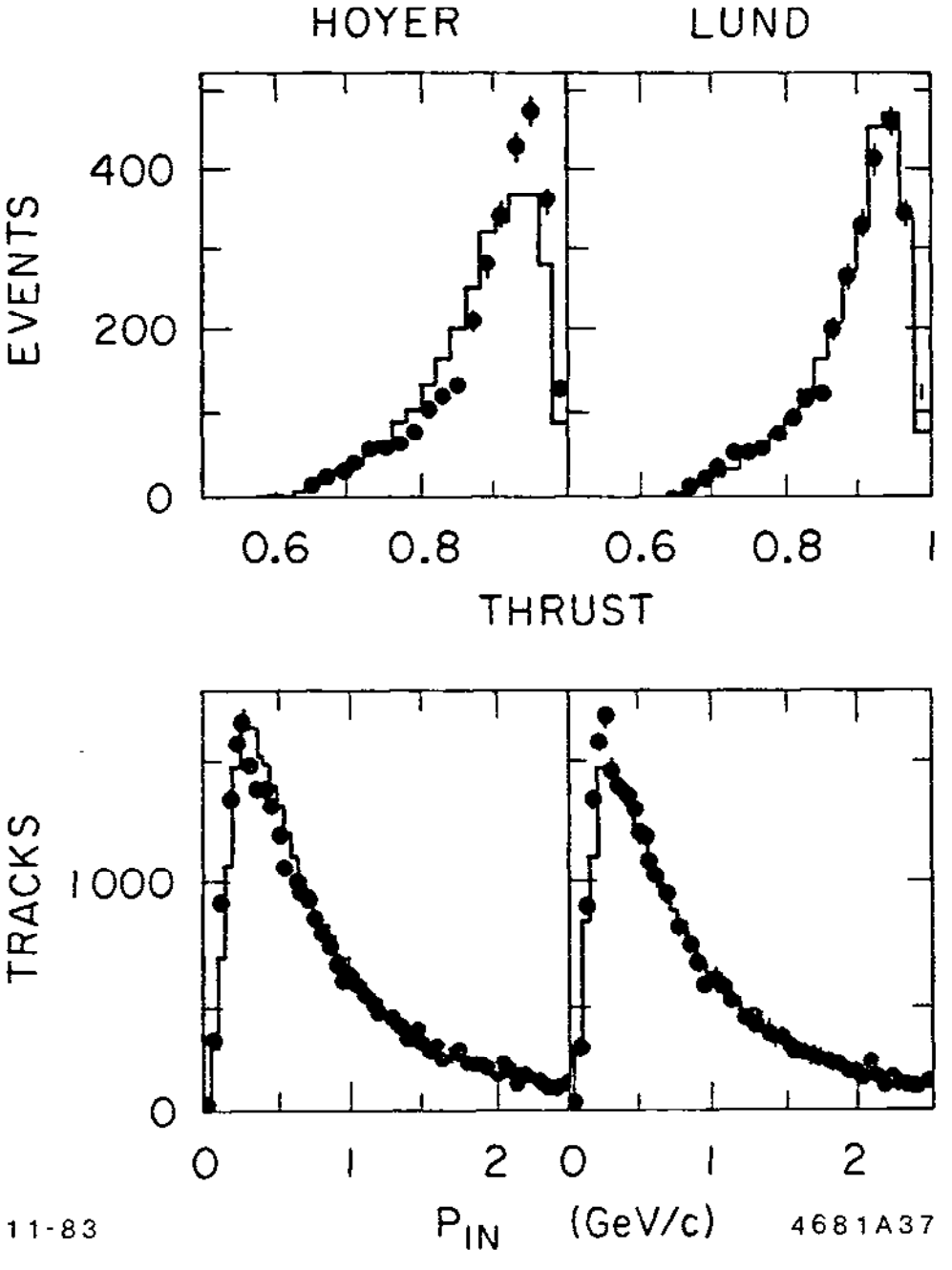
HOYER
LUND
EVENTS
400
200
0
0.6
0.8
0.6
0.8
1
THRUST
TRACKS
1000
0
0
1
2
0
1
2
11-83
P_{IN} (GeV/c)
4681A37

Figure 37

for u, d and s quarks. Heavier quarks are treated with a fragmentation function given by

$$f(z) = \frac{k}{z\left(1 - \frac{1}{z} - \frac{\epsilon}{1-z}\right)^2} \tag{80}$$

where $\epsilon = 0.18$ for c quarks and $\epsilon = 0.04$ for b quarks. The ρ to π ratio is used to determine the pseudoscalar fraction and they find

$$\frac{P}{P+V} = 0.42 \quad . \tag{81}$$

The K production fraction determines the strange quark fraction in the sea

$$\frac{s\bar{s}}{u\bar{u}} = \frac{s\bar{s}}{d\bar{d}} = 0.4 \tag{82}$$

and the proton fraction fixes the ratio of baryon to meson plus baryon production

$$\frac{\text{Prob}\,(q \to q' + B)}{\text{Prob}\,(q \to q' + M) + \text{Prob}\,(q \to q' + B)} = 0.1 \quad . \tag{83}$$

This leaves three free parameters a_L, σ_q and α_s which can be used to fit the remaining shape measures. The results of the fit using $O(\alpha_s^2)$ matrix elements (FKSS) are shown in Table 7 and agree qualitatively with the CELLO conclusion, that the value deduced for α_s is model dependent.

Table 7

TASSO $O(\alpha_s^2)$ Measurements of α_s (Preliminary)		
Method	Independent	String
x_p , Q_1 , Q_2	0.166	0.216
x_p , P_{out}^2 , P_{in}^2	0.155	0.201
3 Clusters , $O(\alpha_s)$	0.170	0.237

A similar study by the MARK J group[27] uses $O(\alpha_s^2)$ matrix elements (ERT) and fits the energy-energy correlations (discussed later) in the range $|\cos x| < 0.72$. In this case they find agreement between the two models on the value of α_s:

$$\alpha_s = 0.14 \pm 0.01 \qquad \text{Lund model}$$

$$\alpha_s = 0.12 \pm 0.01 \qquad \text{Ali model} \quad ,$$

in disagreement with the CELLO $O(\alpha_s)$ result for energy-energy correlations of

$$\alpha_s = 0.15 \pm 0.02 \qquad \text{Hoyer model}$$

$$\alpha_s = 0.25 \pm 0.04 \qquad \text{Lund model} \quad .$$

There is considerable disagreement on the precise value of α_s, and several systematic effects must be taken into account when comparing the different measurements. Different groups use different parameters within the independent models to fit their data. Some of these parameters (particularly σ_q) will affect the value found for α_s. The inclusion of higher order effects tends to decrease the value of α_s, and finally, with each model, determining α_s from the number of three-cluster events or the energy-energy correlation tends to give smaller results than the use of thrust distributions and shape parameters. Hopefully a detailed comparison of all of the parameters used to determine α_s and the sensitivity of α_s to these parameters will eventually allow us to make this measurement. Meanwhile, however, our confidence that this can be done in a truly model independent manner has been considerably shaken.

7. Determining Fragmentation Parameters

From the preceding discussion, it is clear that we need to carefully constrain the fragmentation parameters of the models and test our ideas about this soft physics with the available data before we can make further progress on the perturbative predictions of QCD. There are four ways in which this is currently being done.

* First, the mean multiplicities and momentum spectra of identified particles must be studied to determine the strange quark fraction in the sea, diquark production probabilities, and the spin ratios $\rho : \pi$ and $K^* : K$.

* Second, we should study the way in which quantum numbers are conserved. Are they conserved locally? Is there detailed $p_\perp$ balance between produced baryons? Are strange particles produced in pairs close together in rapidity?

* Third, heavy quark fragmentation must be studied to teach us about quark mass effects and to parameterize $f(z)$ for c and b quarks.

* Finally, we should look for differences between quark and gluon jets to distinguish between models (Hoyer) where their fragmentation is identical and other models (Ali, Lund) where eventually we should see differences in the momentum spectrum of fragmentation products or their multiplicity.

We now discuss the experimental information available on these questions.

New data on particle fractions are available from the TPC detector which uses the 65% truncated mean of 120 samples per track to measure the dE/dx energy loss of particles in the gas of the TPC detector. Different types of particles will have different energy losses depending on the β of the particle. Figure 38 shows the observed bands and allows separation of most particles out to momenta of order 1 GeV. Above 4 GeV, the particle fractions can be determined by fitting the distribution of energy losses. The resultant particle fractions (preliminary) are shown in Figure 39. Similar data are shown in Figure 40(a),(b) and (c), from the HRS, DELCO, and TASSO detectors. The HRS uses time-of-flight techniques to separate the particles, and the DELCO detector uses Čerenkov detectors. The TASSO detector uses a combination of time-of-flight and Čerenkov techniques. The data show good agreement between the different detectors and techniques and indicate that as the particle momenta increase, the difference between π, K and p production diminishes. Extrapolating from the observed behavior, it appears that at momenta of order 20 GeV, we would no longer see any dependence of the production mechanism on either the strangeness or baryon number of the produced particle. At high momenta it is important to remember that the particle fractions are separated statistically by all three methods and hence the fractions have highly correlated errors.

There are still some normalization differences between experiments, particularly in the proton fractions. The original versions of the Lund model adjusted the diquark

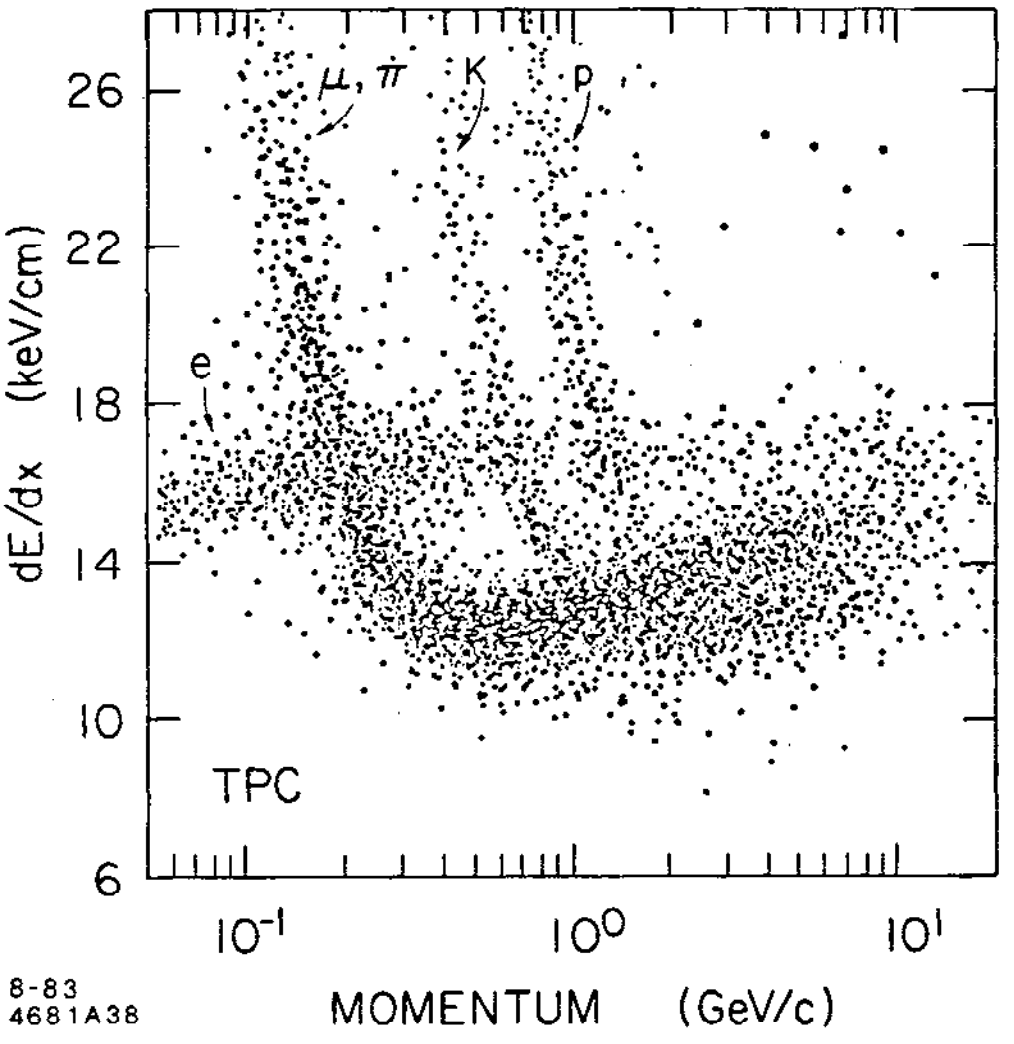
μ, π
K
p
e
26
22
18
14
10
6
dE/dx (keV/cm)
TPC
10⁻¹
10⁰
10¹
MOMENTUM (GeV/c)
8-83
4681A38

Figure 38

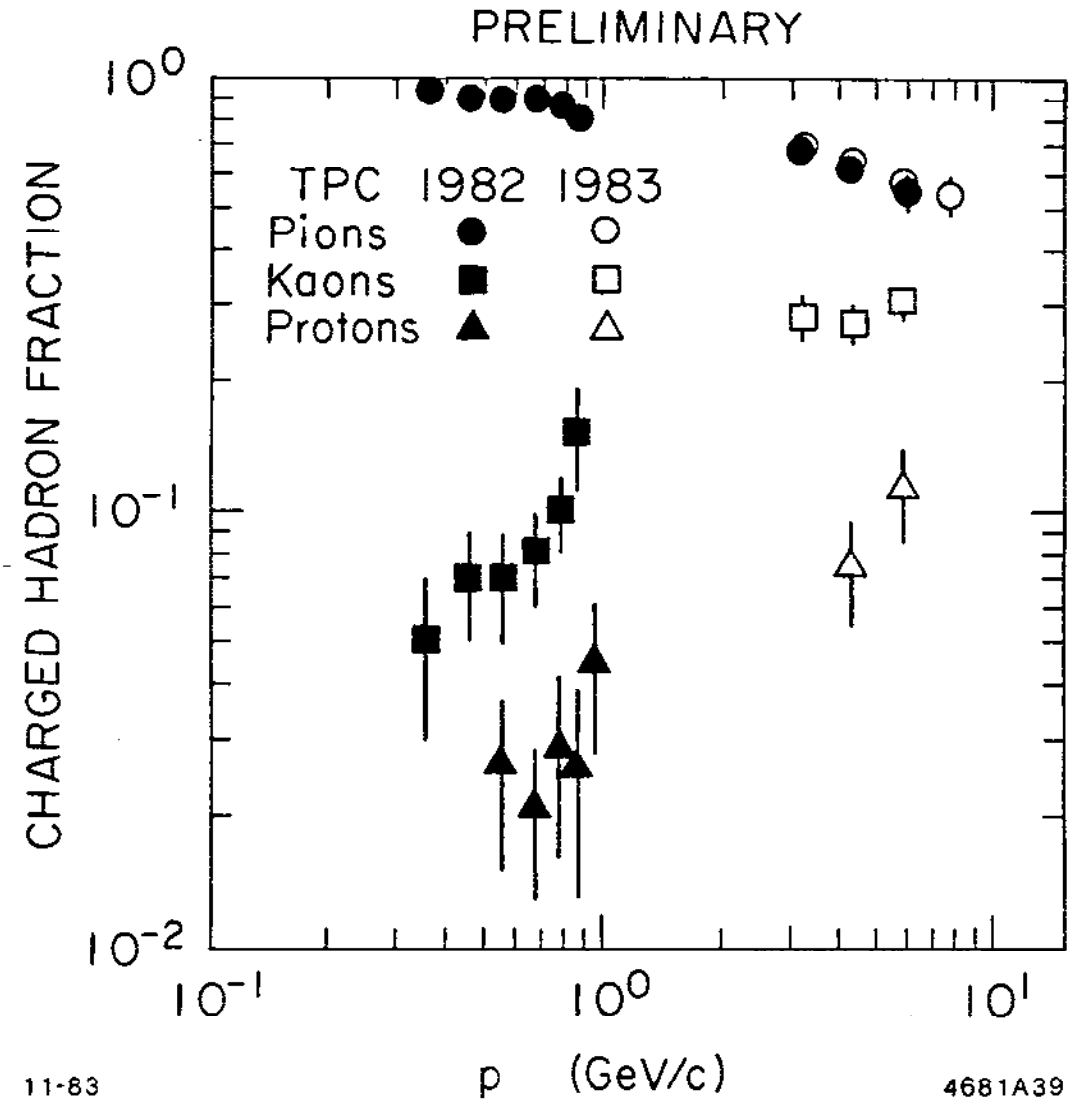
PRELIMINARY
TPC 1982 1983
Pions
Kaons
Protons
CHARGED HADRON FRACTION
10^0
10^{-1}
10^{-2}
10^{-1}
10^0
10^1
p (GeV/c)
11-83
4681A39

Figure 39

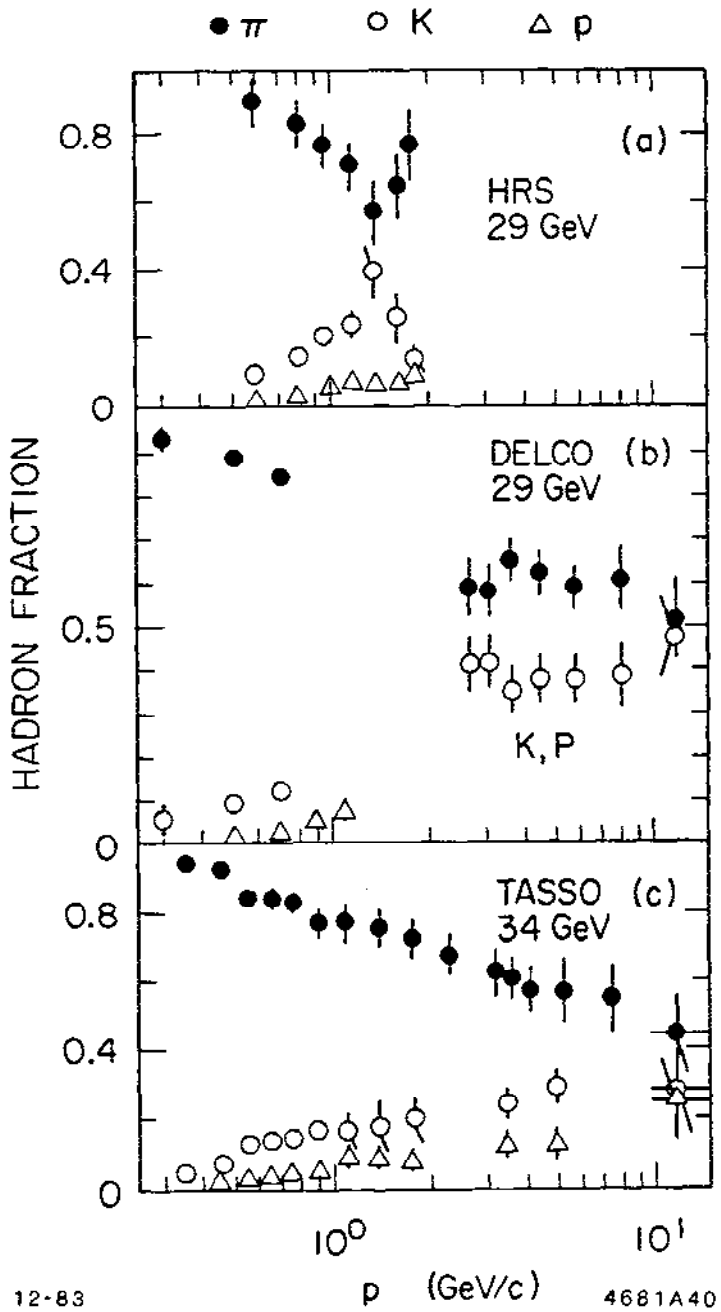
● π ○ K △ p
HADRON FRACTION
0.8
0.4
0
(a)
HRS
29 GeV
DELCO (b)
29 GeV
0.5
K, P
0
TASSO (c)
34 GeV
0.8
0.4
0
10⁰
10¹
p (GeV/c)
12-83
4681A40

Figure 40

production probabilities to 0.065 using data taken in the SPEAR energy range. Data from the MARK II and TASSO detectors indicate that a higher rate of proton production is seen at higher energy and are consistent with a diquark probability of 0.10. Figure 41, however, shows a comparison of the MARK II data on proton fractions with the recent HRS data. The HRS proton fraction is lower and probably in better agreement with the original 0.065 number.

The CELLO group has compared the production of neutral and charged π mesons. Figure 42 shows that the $\pi^{\pm}$ spectrum is the same within statistics as the π° spectrum. There is little room for significant amounts[28] of η production which would give an enhanced yield of π°'s. The data are in good agreement with simple isospin arguments which predict $2\sigma(\pi^{\circ}) \simeq \sigma(\pi^{+}) + \sigma(\pi^{-})$. When compared to hadrons, it appears that the π mesons (which are lighter) fall somewhat more steeply as expected from phase space arguments. The charged π meson spectra at low and high energies are shown in Figure 43 and show a steeply falling exponential with a slower fall off at high x, again as predicted by our phase space arguments.

Having measured the inclusive distribution for pions which is determined by the longitudinal fragmentation function $f(z)$, we can compare it to the same distribution for K mesons to see if the production dynamics of K's are similar. Figure 44 shows the inclusive distribution of K mesons together with the range of values seen at the same energies for π mesons. At high x, the slopes of the distributions are quite similar indicating similar fragmentation mechanisms. At low x, the suppression of the K mesons is due to the heavier mass of these objects since as shown in Equation (14) we expect the slope of the exponential falloff in the low x region to be smaller for higher masses. Figure 45 compares the behavior of the protons with that of the $K^{\pm}$ mesons and again, the behavior is similar in the high x region, and the slope is somewhat smaller in the low x region for the heavier particle.

In studying particle production ratios, neutral K mesons and Λ baryons are useful because they can be detected over a much larger momentum range than charged K's or protons. The detection technique for these particles is based on finding the two-body decay modes $K^{\circ} \rightarrow \pi^{+}\pi^{-}$ and $\Lambda \rightarrow p\pi^{-}$. With somewhat reduced efficiency, this allows detectors which do not have Čerenkov detectors to study the inclusive

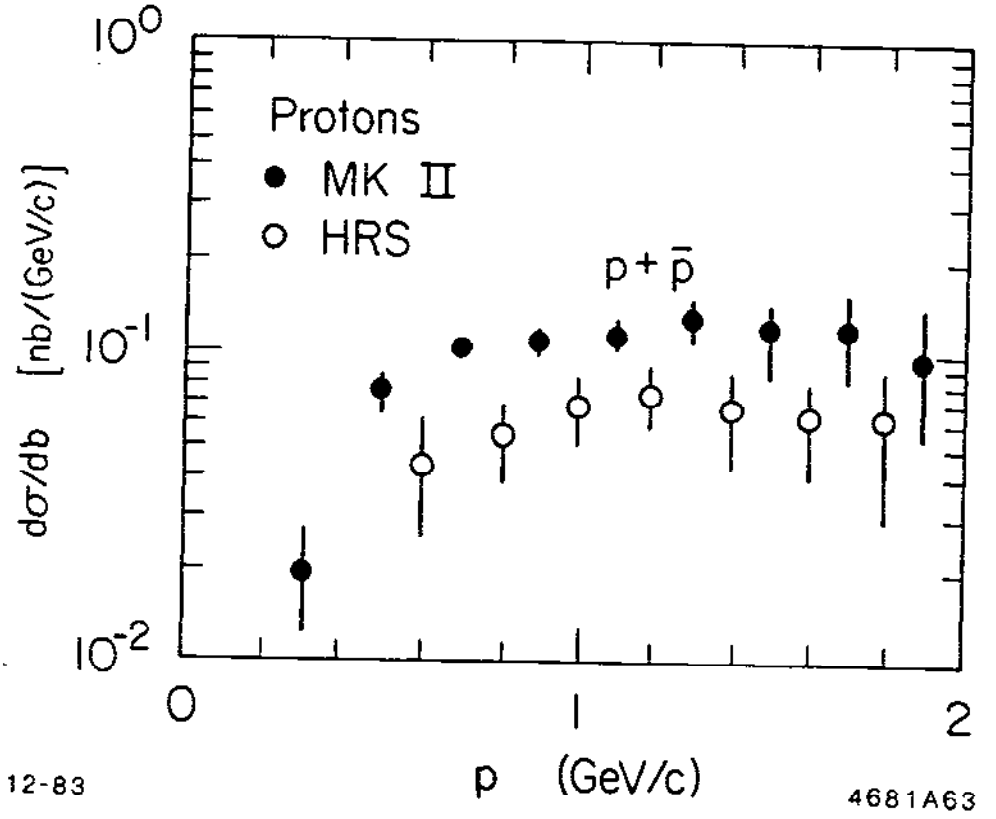
Protons
MK II
HRS
p + p̄
dσ/db [nb/(GeV/c)]
10^0
10^-1
10^-2
0
1
2
p (GeV/c)
12-83
4681A63

Figure 41

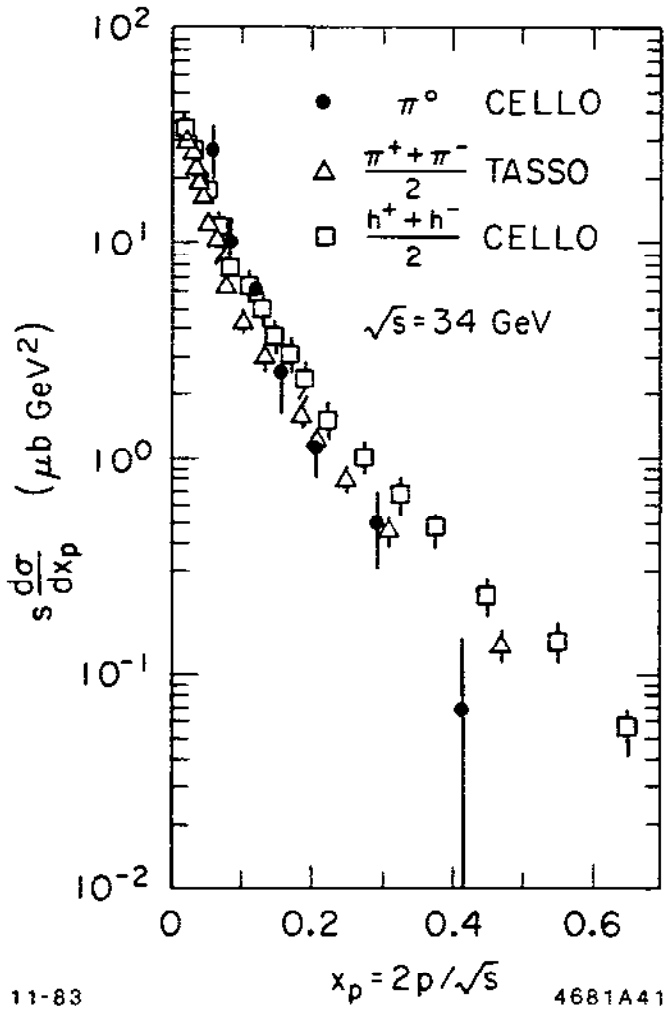
10^2
10^1
10^0
10^{-1}
10^{-2}
$s\frac{d\sigma}{dx_p}$ (μb GeV^2)
π° CELLO
$\frac{\pi^+ + \pi^-}{2}$ TASSO
$\frac{h^+ + h^-}{2}$ CELLO
$\sqrt{s} = 34$ GeV
0
0.2
0.4
0.6
$x_p = 2p/\sqrt{s}$
11-83
4681A41

Figure 42

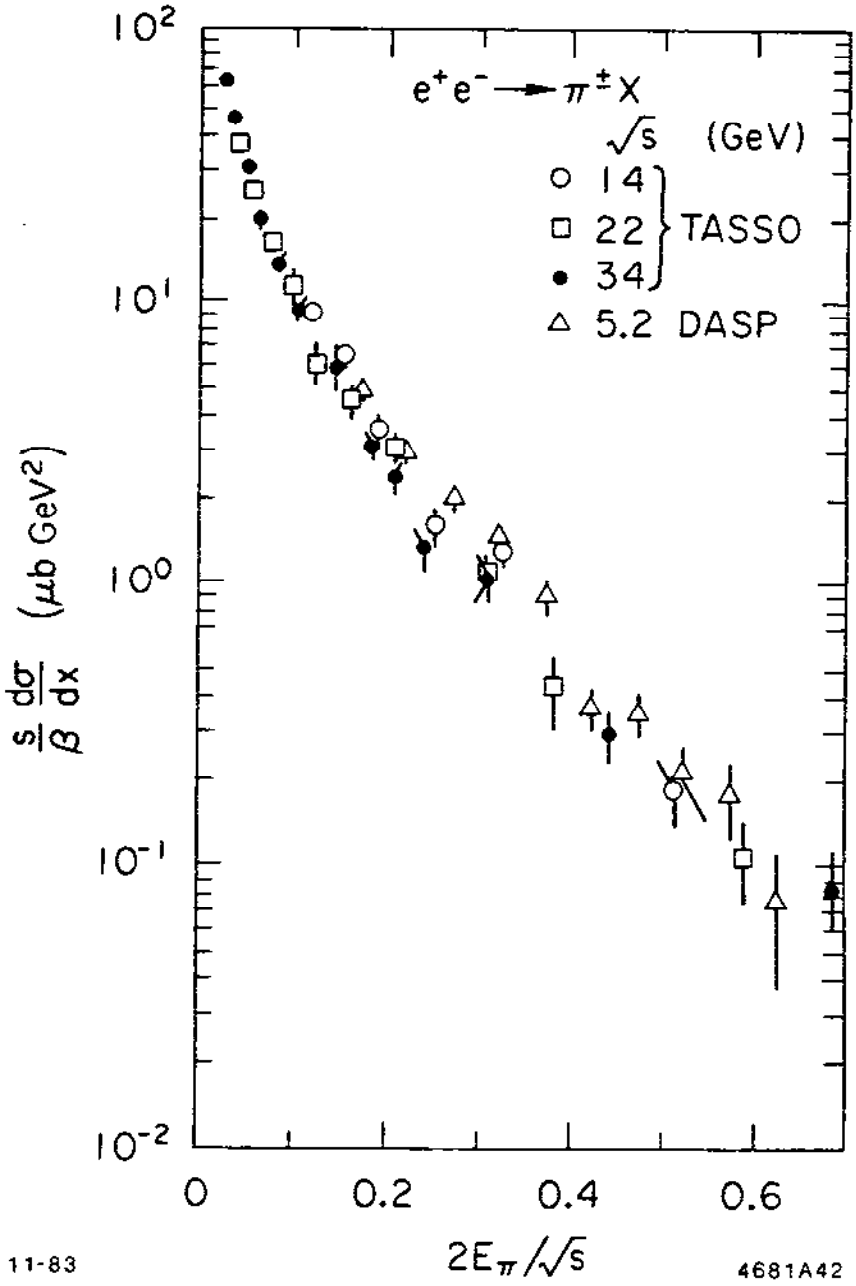
10^2
10^1
10^0
10^{-1}
10^{-2}
$e^+e^- \rightarrow \pi^\pm X$
$\sqrt{s}$ (GeV)
14
22
34
TASSO
5.2 DASP
$\frac{s}{\beta}\frac{d\sigma}{dx}$ (μb GeV^2)
0
0.2
0.4
0.6
$2E_\pi/\sqrt{s}$
11-83
4681A42

Figure 43

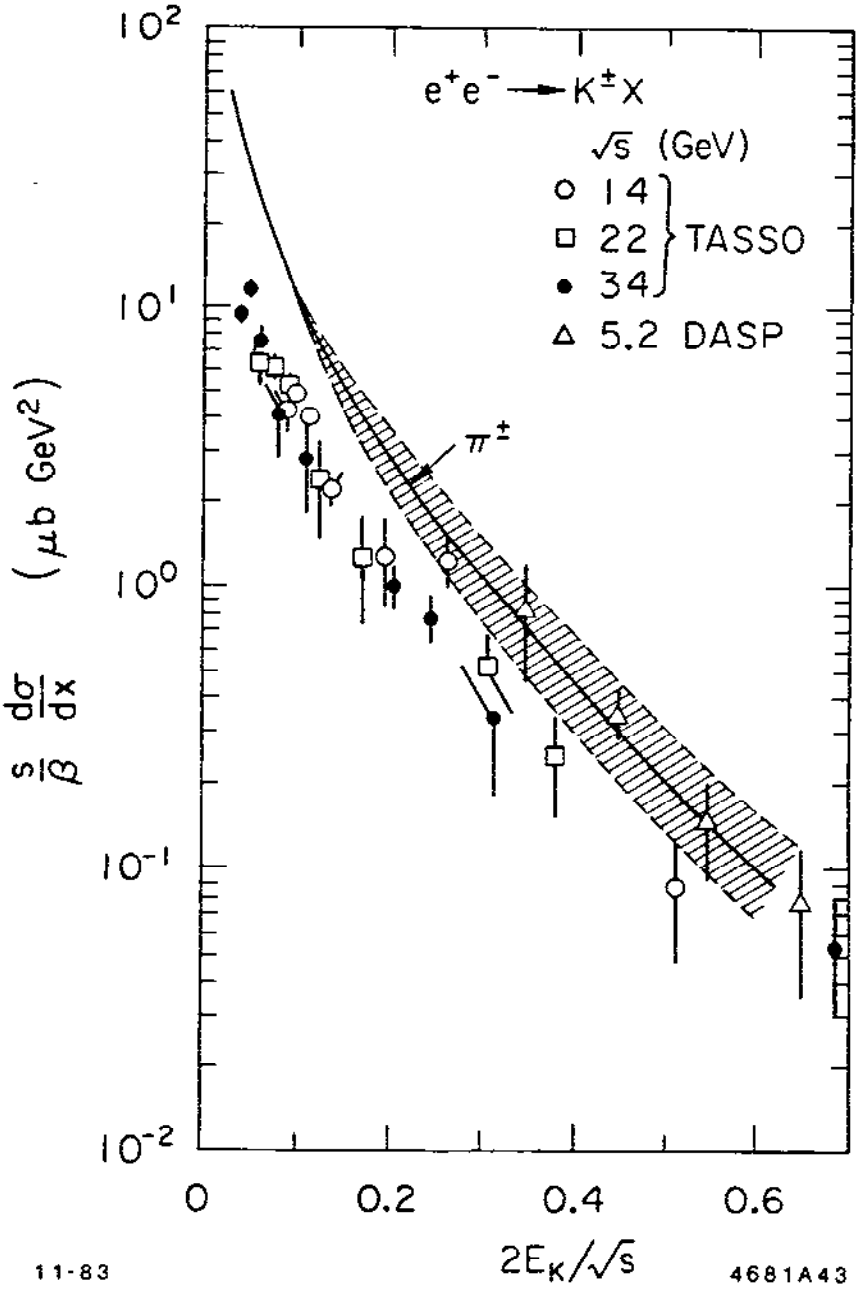
10^2
10^1
10^0
10^{-1}
10^{-2}
$e^+e^- \rightarrow K^\pm X$
$\sqrt{s}$ (GeV)
14
22
34
TASSO
5.2 DASP
$\pi^\pm$
$\frac{s}{\beta}\frac{d\sigma}{dx}$ (μb GeV^2)
0
0.2
0.4
0.6
$2E_K/\sqrt{s}$
11-83
4681A43

Figure 44

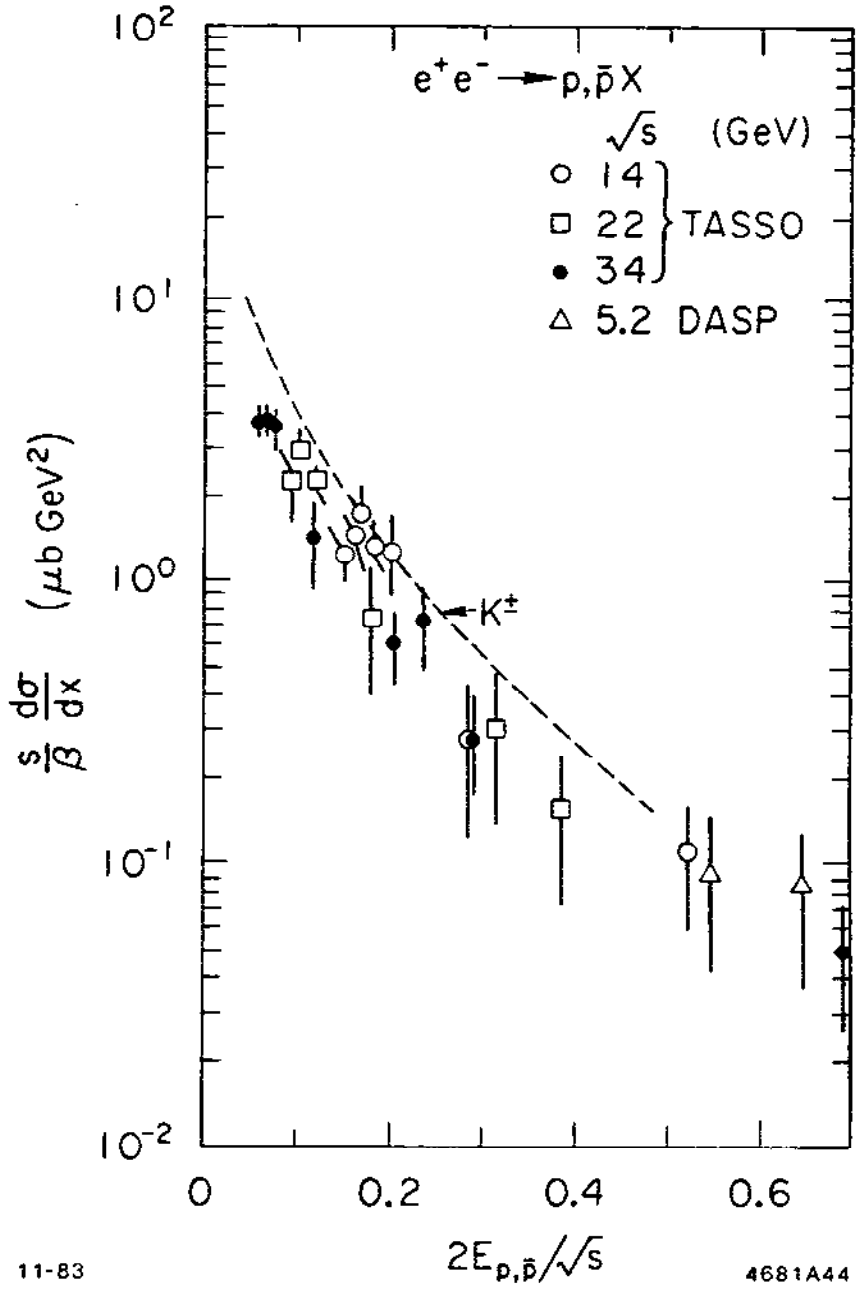
10^2
10^1
10^0
10^{-1}
10^{-2}
$e^+e^- \rightarrow p,\bar{p}X$
$\sqrt{s}$ (GeV)
14
22
34
TASSO
5.2 DASP
$K^\pm$
$\frac{s}{\beta}\frac{d\sigma}{dx}$ (μb GeV^2)
0
0.2
0.4
0.6
$2E_{p,\bar{p}}/\sqrt{s}$
11-83
4681A44

Figure 45

spectra of these particles. Figure 46 shows a comparison of the K° and Λ spectra with the π meson spectra from data taken by the TASSO detector. The ratio of K to Λ production is ~ 2.7 over the range $0.1 < X < 0.3$. This ratio is a free parameter in the independent fragmentation models, but is fixed in the LUND model due to the presence of $e^{-M^2/K}$ vertex factors.

7.1 ENERGY DEPENDENT PARAMETERS

In making these comparisons, we have so far ignored the fact that the particle fractions are changing as a function of center-of-mass energy. As shown in Figure 47, there is considerable information about the behavior of these fractions, and in principle we should expect that the model used to parameterize the high energy fragmentation behavior would also predict the observed energy dependence. In practice, while many groups have tried to optimize the model parameters at a single energy, very little work has been done to determine whether a single set of parameters also gives a consistent picture of these energy dependent effects.

In fact, we know that at least some of the parameters used in present models are energy dependent. This means that in order to implement a single set of energy independent parameters, the model builders will have to include further dynamical effects. As an example of this energy dependence, we examine the behavior of $s\bar{s}$ production from the sea. In order to determine this parameter, we must fit the observed rate of K° production.

Figure 48 shows that the number of K°'s observed per event changes by ~ 0.4–0.6 when crossing the charm threshold. Thus at ~ 5 GeV, roughly half of the observed rate comes from charm, and half comes from u, d or s quark production. Since the number of K's from charm depends for the most part on decay branching ratios of charm mesons, we ask only that the fragmentation model predict the observed K° rate which **does not** come from charm. For values of the probability of $s\bar{s}$ production between 0.0 and 0.1, the Feynman–Field model predicts noncharm K° rates between 0.57 and 0.92. The observed rate,[29] however, is 0.52 ± 0.05 which gives an estimate of $P_{s\bar{s}}$ of

$$P_{s\bar{s}} < 0.03 \ @ \ 7.3 \text{ GeV} \quad .$$

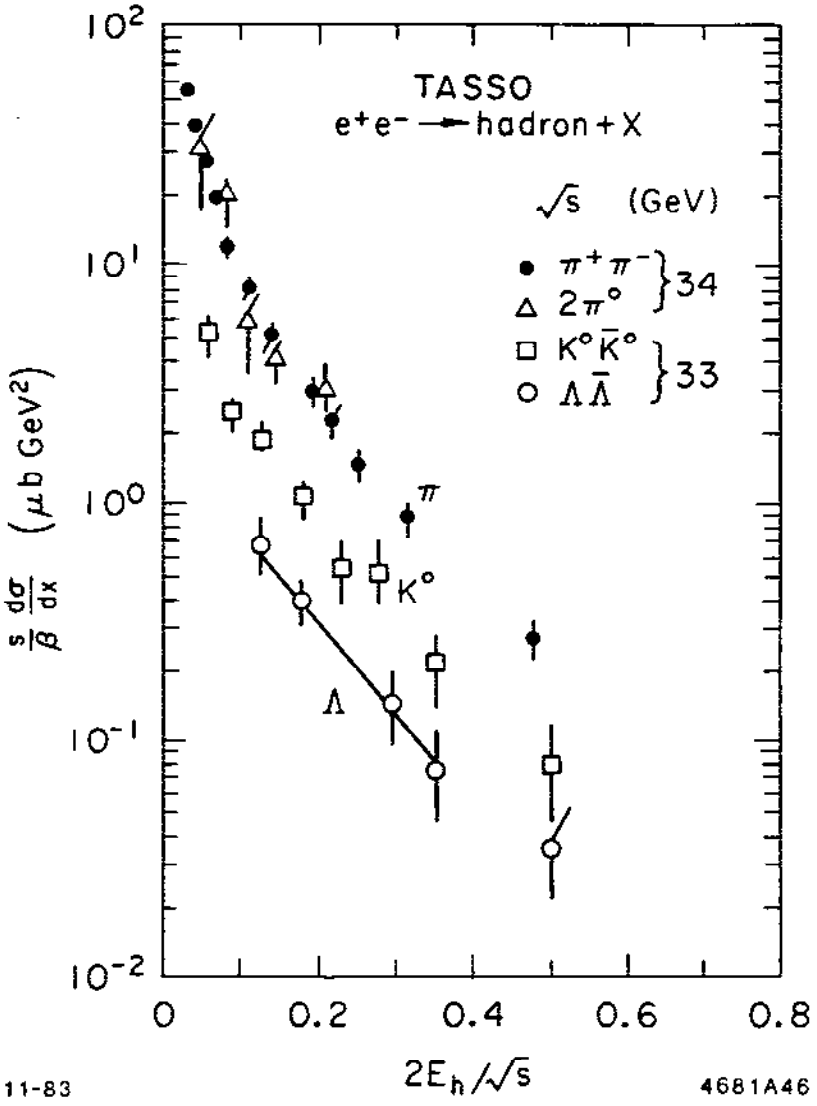
TASSO
e+e- → hadron + X
√s (GeV)
π+π- } 34
2π°
K°K̄° } 33
ΛΛ̄
π
K°
Λ
10²
10¹
10⁰
10⁻¹
10⁻²
0
0.2
0.4
0.6
0.8
s/β dσ/dx (μb GeV²)
2E_h/√s
11-83
4681A46

Figure 46

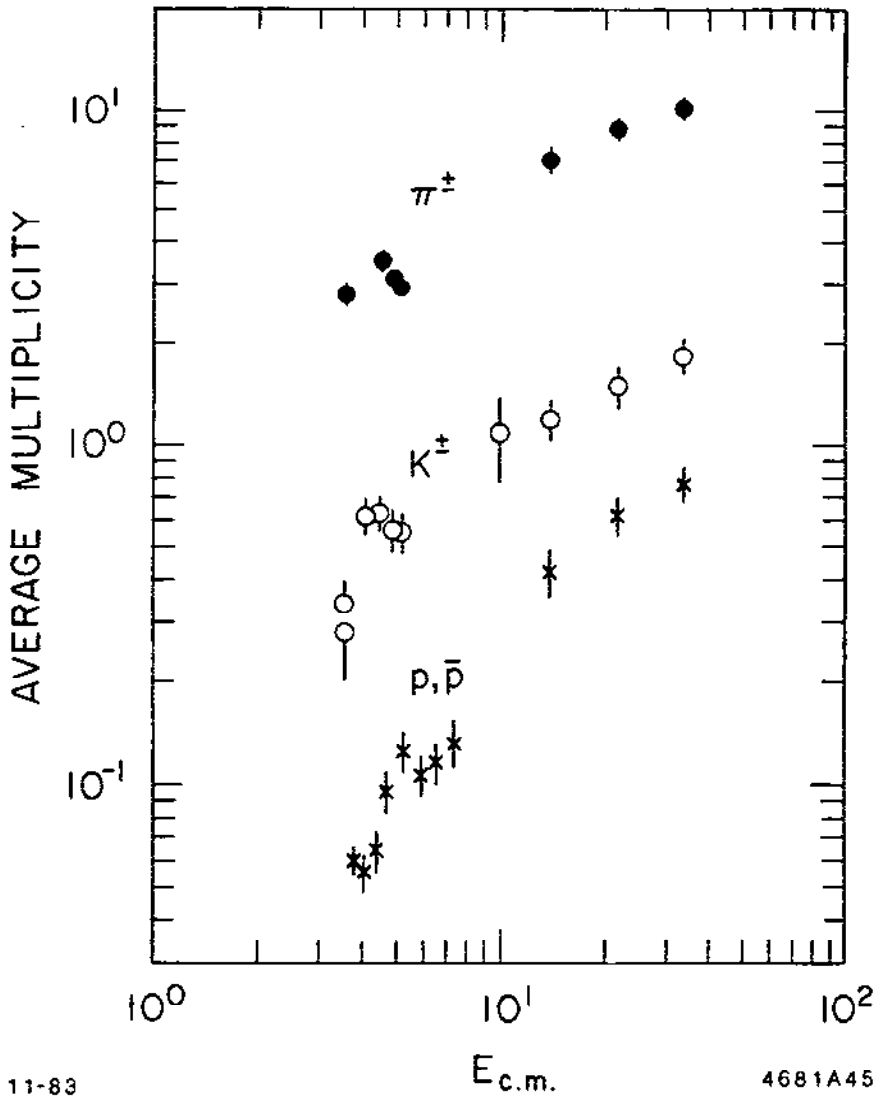
AVERAGE MULTIPLICITY
10^1
10^0
10^{-1}
$\pi^{\pm}$
$K^{\pm}$
$p,\bar{p}$
10^0
10^1
10^2
$E_{c.m.}$
11-83
4681A45

Figure 47

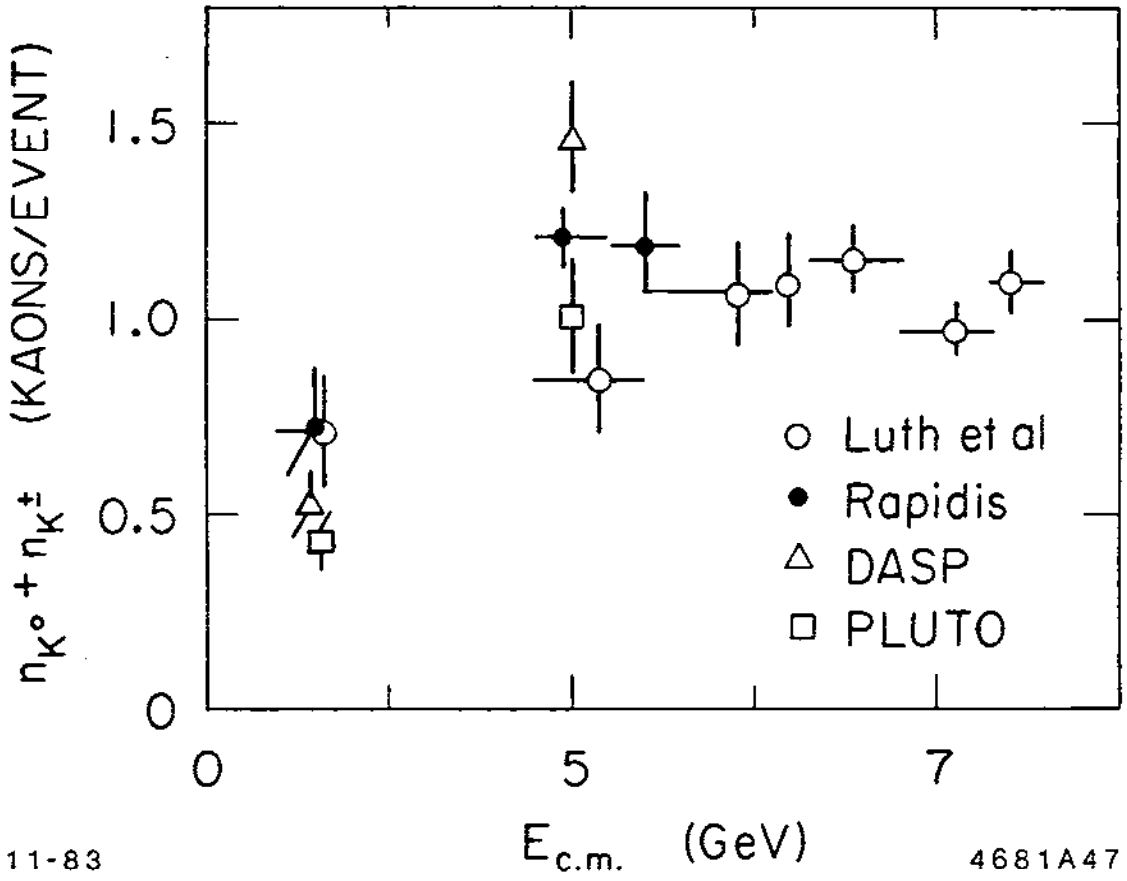
$n_{K^0} + n_{K^\pm}$ (KAONS/EVENT)
1.5
1.0
0.5
0
0
5
7
$E_{c.m.}$ (GeV)
Luth et al
Rapidis
DASP
PLUTO
11-83
4681A47

Figure 48

There are several additional uncertainties which must be accounted for in repeating this exercise at higher energy. Both bottom and charm mesons will now contribute to the observed K° rate. Furthermore, the effective branching ratio of b, c quarks to K° will depend on the fraction of D^* and D mesons produced. Figure 49 shows the (preliminary) MARK II rate for K°'s per event together with the prediction of the independent fragmentation model as a function of $P_{s\bar{s}}$ for values of $B(b,c \to K^\circ)$ between 0.36 and 0.56. This yields a value

$$P_{s\bar{s}} = 0.08 \pm 0.04 \quad @\ 29\ \text{GeV} \qquad .$$

This value of $P_{s\bar{s}}$ assumes that the production of strange baryons proceeds through mechanisms other than strange quark sea production. If, however, Λ production comes predominantly from diquark production with strangeness provided by an $s\,\bar{s}$ from the sea, then $P_{s\bar{s}}$ must be increased by ~ 0.04.

By comparing the low energy value of $P_{s\bar{s}}$ to the high energy value, we see that this parameterization of strange quark production is energy dependent. This is not really surprising since the independent fragmentation model does not explicitly account for quark mass effects and is using the $P_{s\bar{s}}$ parameter to describe the phase space suppression of the heavier strange quark. While the 1 GeV rest mass of the pair is significant at 7.3 GeV, we expect it to be less so at higher energies. It would be an interesting test of the dynamical model of such suppressions in the Lund model (i.e., tunneling) to apply that model to the center-of-mass energy variation of strange meson production.

7.2 Correlations Between Parameters

In addition to being energy dependent, many of the fragmentation model parameters are highly correlated. As an example of this, we now look at the effect of changing the vector fraction on the previous parameter $P_{s\bar{s}}$. If the production probabilities of u and s quarks at each branching are related by $s \simeq .3\,u$, then $P_{s\bar{s}}$ will be given by

$$\frac{s}{\text{TOT}} = \frac{.3}{.3+1+1} = .13 \qquad . \tag{84}$$

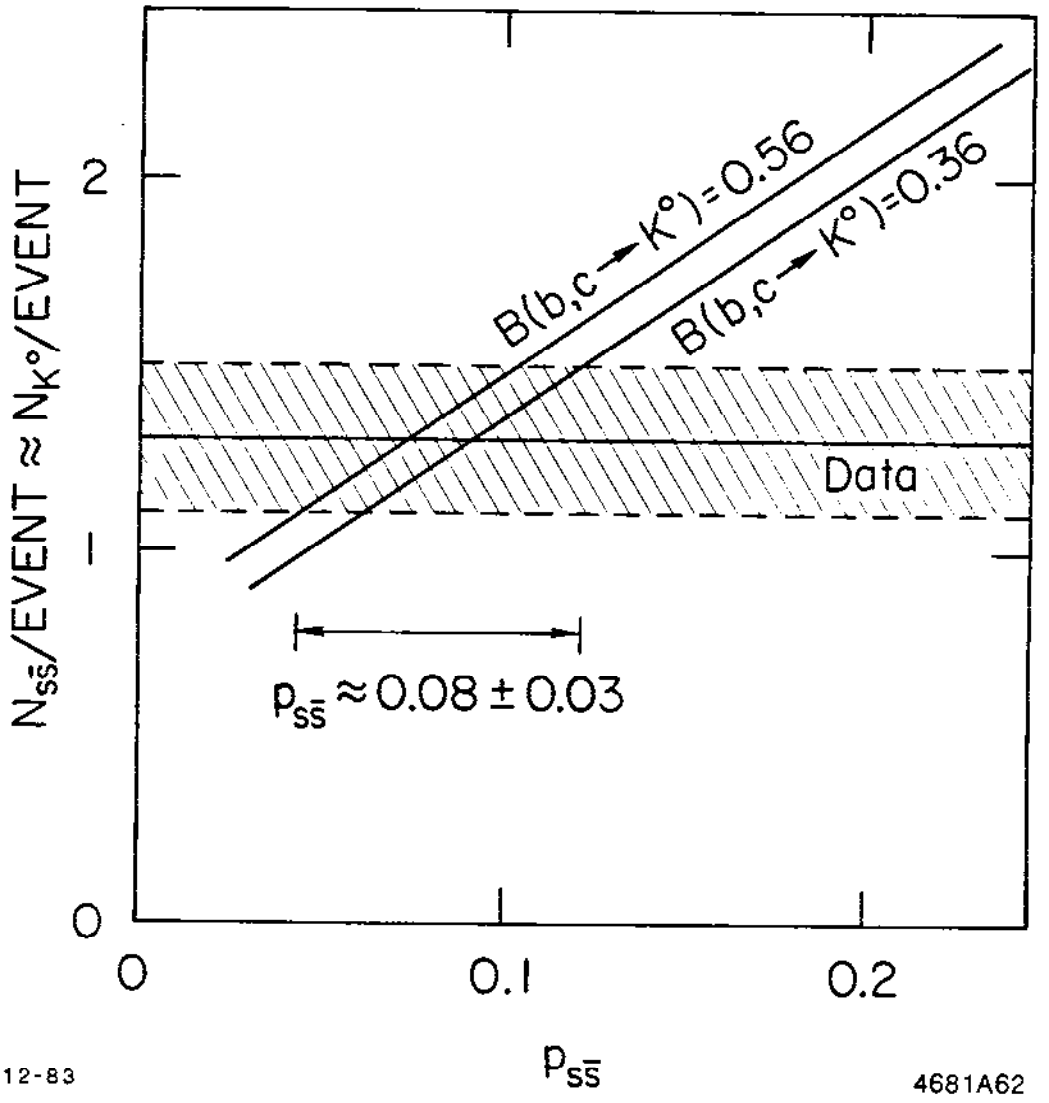
$N_{s\bar{s}}$/EVENT ≈ N_{K°/EVENT
2
1
0
0
0.1
0.2
$p_{s\bar{s}}$
B(b,c→K°)=0.56
B(b,c→K°)=0.36
Data
$p_{s\bar{s}} \approx 0.08 \pm 0.03$
12-83
4681A62

Figure 49

The observable is, however, not $P_{s\bar{s}}$ but the rate of K's per event. If we observe $\sim 1.3K^\circ$/event and again assume that 0.4–0.6 comes from charm production, then roughly 1 K°/event is due to $s\,\bar{s}$ production in the branchings of the fragmentation process. But to convert $P_{s\bar{s}}$ into an observed total rate, we need to know **how many** branches, N_B, there are on average in the fragmentation. This number of branches will of course also determine the final state multiplicity, however, it is only the primary mesons whose multiplicities are directly determined by N_B.

For a fixed secondary meson multiplicity, N_S, the relation between N_B and N_S and hence the relation between $P_{s\bar{s}}$ and N_{K° will depend on the vector fraction,V. For example, if $N_S \sim 18$ and the vector fraction is 1, the primary multiplicity is $N_S/2$ because the primary mesons are all ρ mesons and $\rho \to \pi\pi$. Since 1 K°/event will come from one $s\,\bar{s}$ pair (assuming equal charged and neutral K's), this translates to a $P_{s\bar{s}}$ of

$$\frac{s\,\bar{s}}{\text{TOT}} \sim \begin{cases} 1/18 & V = 0 \\ 1/9 & V = 1 \end{cases} . \tag{85}$$

The vector fraction can be directly determined by fitting the observed rates for ρ and K^* production. Figure 50 shows the observed $\pi\pi$ mass spectra at 7.3 GeV (MARK I) together with fits for a smooth background and K° and ρ production. The measured ρ° spectra yield $0.4 \pm 0.1\,\rho^\circ$/event which gives a vector fraction

$$\begin{aligned} V &= 0.24 \pm 0.12 \qquad \text{at 7.3 GeV} \quad , \\ P &= 0.76 \pm 0.12 \quad . \end{aligned} \tag{86}$$

A similar measurement has been made by the TASSO group,[30] and is shown in Figure 51 for data taken at 14, 22 and 34 GeV. Figure 52 shows the inclusive cross-section at 34 GeV compared to the π meson distribution with the familiar features of suppression of high mass production at low x and mass independent production at high x. The total number of ρ°/event in the x range $0.2 < x < 0.7$ is shown in Table 8 and determines a pseudoscalar fraction of $P/(P+V) = 0.42 \pm 0.08 \pm 0.15$ or

$$\begin{aligned} V &= 0.58 \pm 0.17 \quad , \\ P &= 0.42 \pm 0.17 \qquad \text{at 34 GeV} \quad . \end{aligned} \tag{87}$$

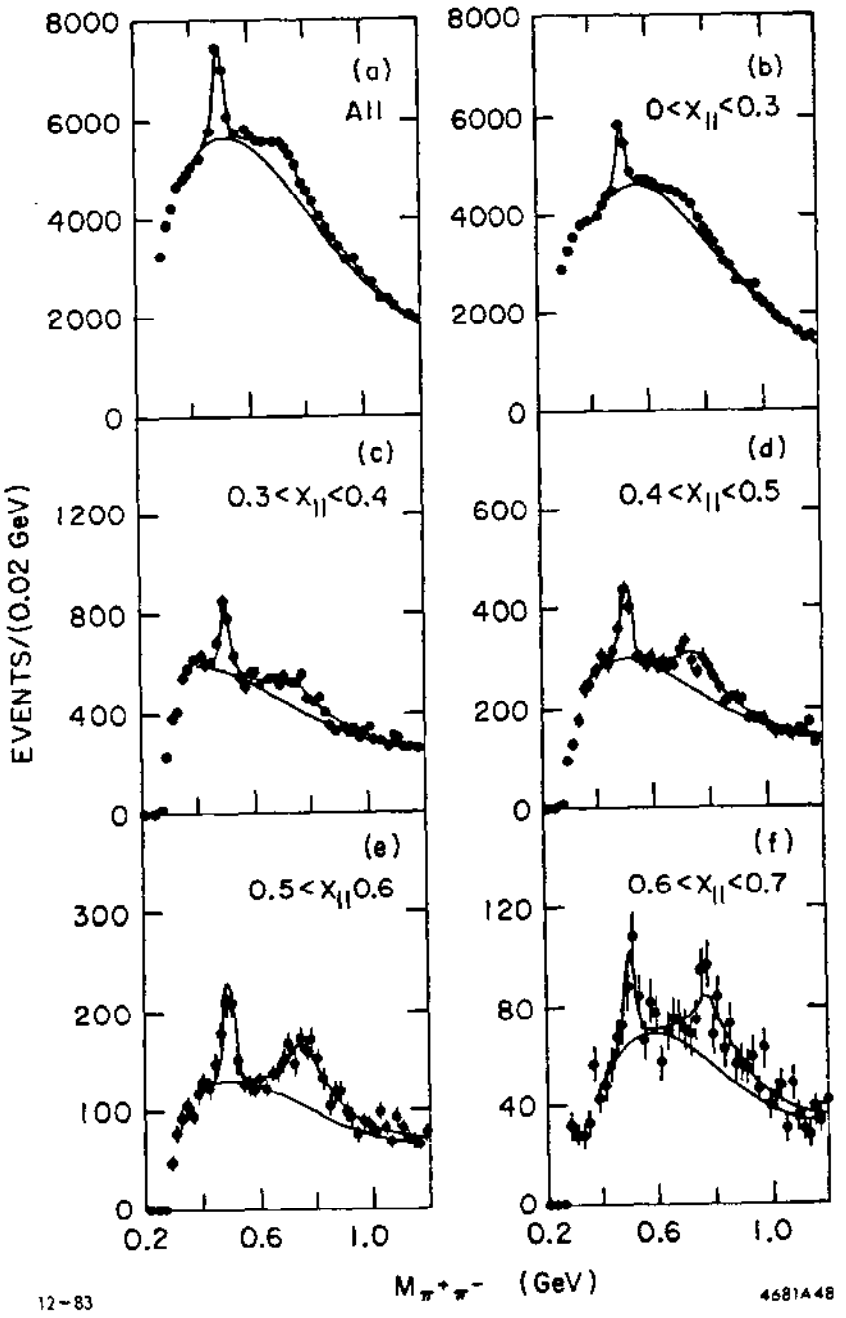
(a)
All
(b)
0<X11<0.3
(c)
0.3<X11<0.4
(d)
0.4<X11<0.5
(e)
0.5<X11<0.6
(f)
0.6<X11<0.7
EVENTS/(0.02 GeV)
Mπ+π- (GeV)
12-83
4681A48

Figure 50

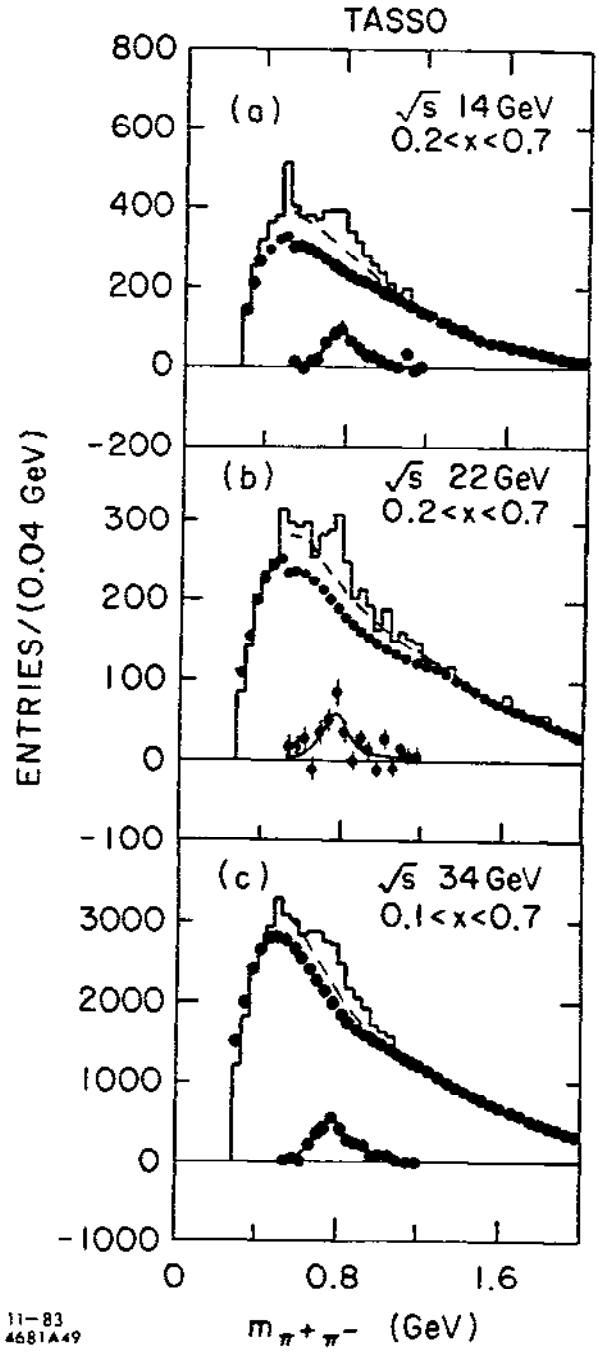
TASSO
(a)
√s 14 GeV
0.2<x<0.7
(b)
√s 22 GeV
0.2<x<0.7
(c)
√s 34 GeV
0.1<x<0.7
ENTRIES/(0.04 GeV)
800
600
400
200
0
-200
300
200
100
0
-100
3000
2000
1000
0
-1000
0
0.8
1.6
$m_{\pi^+\pi^-}$ (GeV)
11-83
4681A49

Figure 51

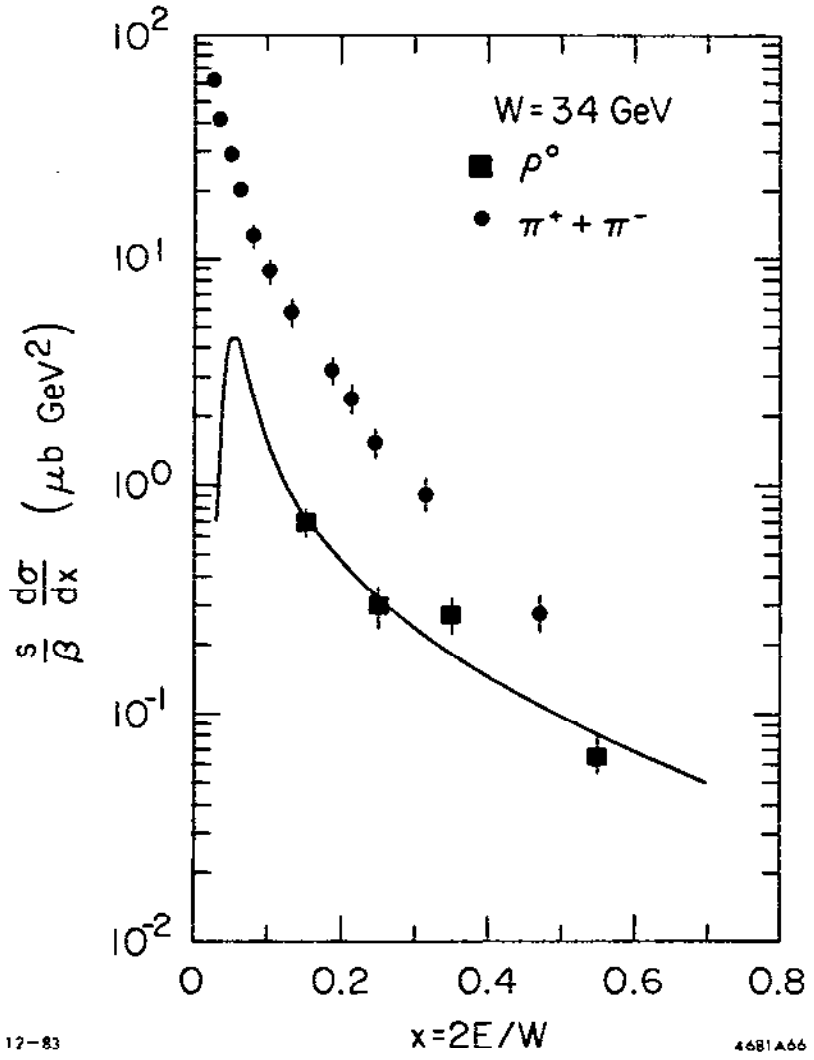
W = 34 GeV
ρ°
π⁺ + π⁻
10²
10¹
10⁰
10⁻¹
10⁻²
0
0.2
0.4
0.6
0.8
x=2E/W
s/β dσ/dx (μb GeV²)
12-83
4681A66

Figure 52

Table 8

TASSO ρ Production	
ρ_0 per event $(0.2 < x < 0.7)$	$\sqrt{s}$ (GeV)
$0.33 \pm 0.06 \pm 0.07$	14
$0.22 \pm 0.06 \pm 0.05$	22
$0.22 \pm 0.02 \pm 0.05$	34

The vector fraction is suppressed at low energies presumably because of the higher mass of vector ρ compared to pseudoscalar π. If there were no mass effects, we would expect the pseudoscalar to vector ratio to be the ratio of number of states

$$\frac{P}{V} = \frac{1}{3} \quad . \tag{88}$$

Although consistent with $V = 3P$, the central values of the TASSO measurements give $P/V \sim 1/1.4$ and the 7.3 GeV measurements give $P/V \sim 3.5/1$.

In summary, the study of perturbative QCD effects such as the determination of α_s requires a detailed parameterization of hadronization. Different models at present seem to give different results, thus we must be sure that each model correctly describes as many features of the data as possible. We already know that models as different as the Ali and Lund approaches can be adjusted at a particular energy to be virtually indistinguishable. Thus, the only possibility to distinguish between different dynamical assumptions appears to be to make use of the center-of-mass dependence of the parameterizations. As we have seen, this is complicated not only by the fact that there are charm and bottom thresholds between the low and high energy regions, but also by the fact that the models rely heavily on the simplifying assumptions of massless quarks and statistical spin ratios and hence cannot be expected to correctly predict low energy phenomena.

7.3 Quantum Number Correlations

So far we have used only the single particle inclusive distributions and particle ratios to test the dynamics of fragmentation. It is also possible to use particle correlations and in particular to look at the details of the ways in which charge, strangeness and baryon number are conserved in the models. In a model of fragmentation which uses the sequential production of $q\bar{q}$ pairs such as that shown in Figure 53 for example, we would expect that strangeness conservation is accomplished locally by the production of $s\bar{s}$ pairs. If the particles from such a pair tend to lie close together in rapidity, then there should be strong rapidity correlations for pairs of strange mesons. Similarly, if baryon production arises from diquark–antidiquark production, baryon–antibaryon pairs should show similar correlations.

Charge is also conserved locally in such a model. Note that if the event is divided into two jets as shown in Figure 53, the charge of each jet is either 0 or ± 1 depending on the flavor of the "last" $q\bar{q}$ pair. Groups of particles separated by $\sim 2y_{\rm MAX}/N_B$ should have zero net charge, and leading particles in each jet should be oppositely charged. The first evidence for this type of behavior was found by the TASSO group.[31] The data in Figure 54 shows the charge compensation probability $\tilde{\phi}_r(y,y')$ which is the probability for fixed y' that the particle charge at y' is compensated by an oppositely charged particle at y normalized to the density of particles at y and y'. As can be seen in the figure, the charge of a particle tends to be compensated by a short range correlation with other particles with $\Delta y \sim \pm 1.5$. The open circles compare the results which are obtained using the same events but randomizing all of the charges in the final state. In principle, this randomization should only be applied to primary mesons, since we have already seen, Equation (87), that vector meson production is significant. Nevertheless, the results are in good agreement with an independent fragmentation model of the Ali type. In addition to the short range correlation, the fastest particles ($2.5 \leq |y'| \leq 5.5$) show a long tail in the charge compensation probability indicating that $\sim 15 \pm 3\%$ of the charge is compensated by particles in the opposite jet. The authors were unable to reproduce this long range correlation using a model which produced neutral partons [$MC(gg)$] obeying Feynman–Field fragmentation, and interpreted it as evidence for the production of charged primary partons.

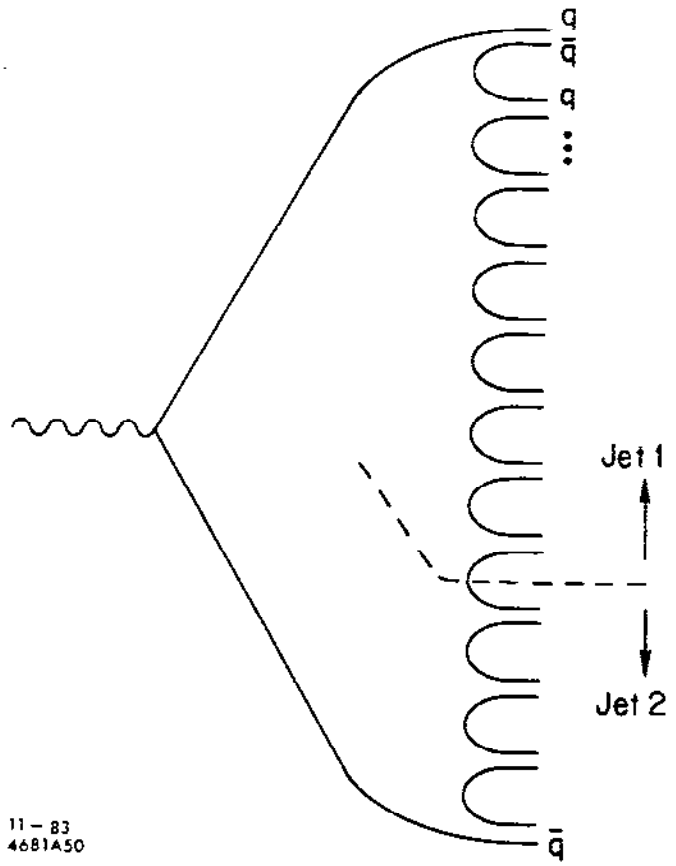

Figure 53

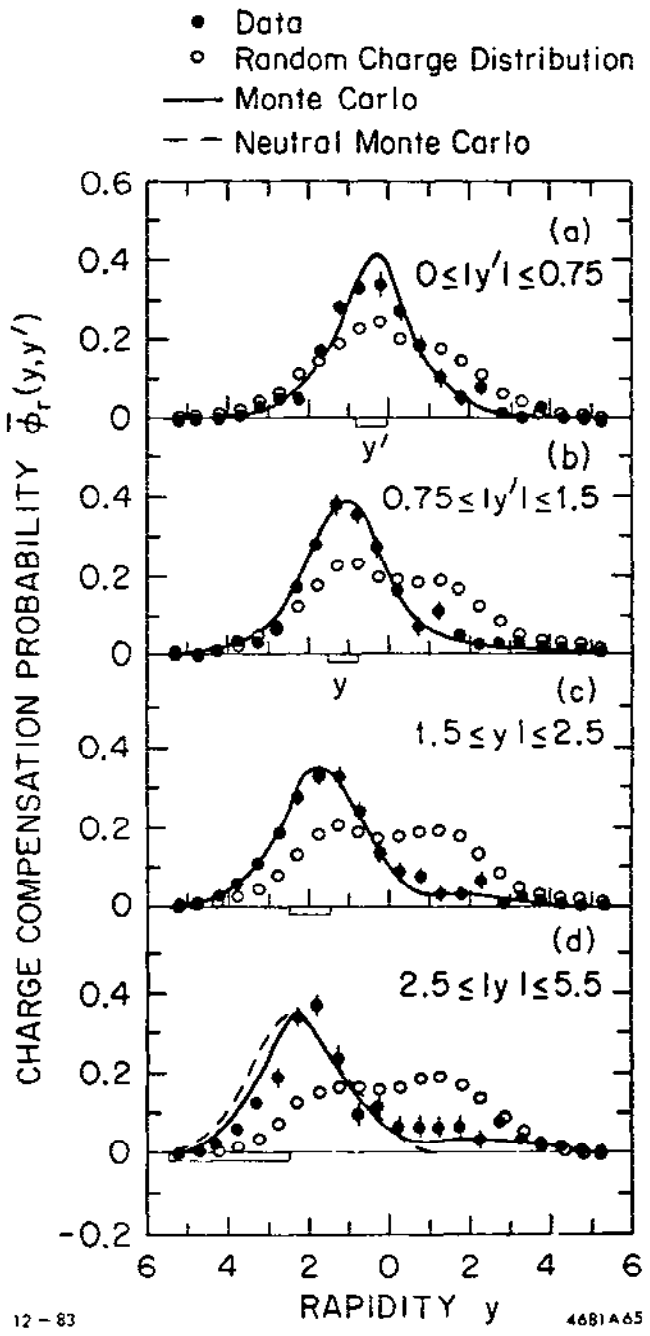
Data
Random Charge Distribution
Monte Carlo
Neutral Monte Carlo
CHARGE COMPENSATION PROBABILITY $\bar{\Phi}_r(y,y')$
(a)
$0 \le |y'| \le 0.75$
(b)
$0.75 \le |y'| \le 1.5$
(c)
$1.5 \le |y| \le 2.5$
(d)
$2.5 \le |y| \le 5.5$
y'
y
0.6
0.4
0.2
0
-0.2
6
4
2
0
2
4
6
RAPIDITY y
12 – 83
4681A65

Figure 54

In a similar study of two particle charge correlations, the PLUTO group found[32] that the mean charge of a jet in a two jet event was

$$|Q| = 0.55 \pm 0.25 \quad . \tag{89}$$

This was determined by extrapolating the observed mean jet charge with experimental cuts between the values detected for Feynman-Field jets with charges of zero and one. This value is in good agreement with what would be expected from the simplest model. Let us assume that primary quarks u, d, s, c, b are produced with probabilities $4/11 : 1/11 : 1/11 : 4/11 : 1/11$, and $q\bar{q}$ pairs of the type u, d, s are produced in the ratio $1 : 1 : .3$ or $.43 : .43 : .13$. Then a charge one jet will result from a u quark provided the "last" quark pair is of the $d\bar{d}$ or $s\bar{s}$ type. Similarly, charge one jets will result from d quarks when the last pair is a $u\bar{u}$. Thus the average jet charge is just

$$2 \times \frac{4}{11} \times [.43 + .13] + 3 \times \frac{1}{11} \times [.43] = 0.52 \quad . \tag{90}$$

Figure 55 shows preliminary data from the TPC detector. They measure the product of charges in the two jets with a gap of width Δy excluded from the central region. Thus for $\Delta y \to 0$, this product is the product of jet charges, and for $\Delta y \to 8$, it measures the correlation of the leading particles. The event sample consists of events with sphericity less than 0.25 and charged multiplicity greater than five. Also shown is the fact that the fragmentation parameters for two-jet events in the Lund model reproduce the shape of the observed correlations and that models with random final state charges or randomized charges for the primary mesons do not agree with the data. Similar (preliminary) data are shown in Figure 56 from the MARK II detector (an $x_\perp$ cut is used in place of a rapidity gap) and compared to the behavior of charge one and charge zero jets in the Ali model. As in the case of the PLUTO data, one can extrapolate between the behavior of these two samples to determine the mean charge product of two jets

$$-\langle Q_1 Q_2 \rangle = 0.53 \pm 0.12 \quad . \tag{91}$$

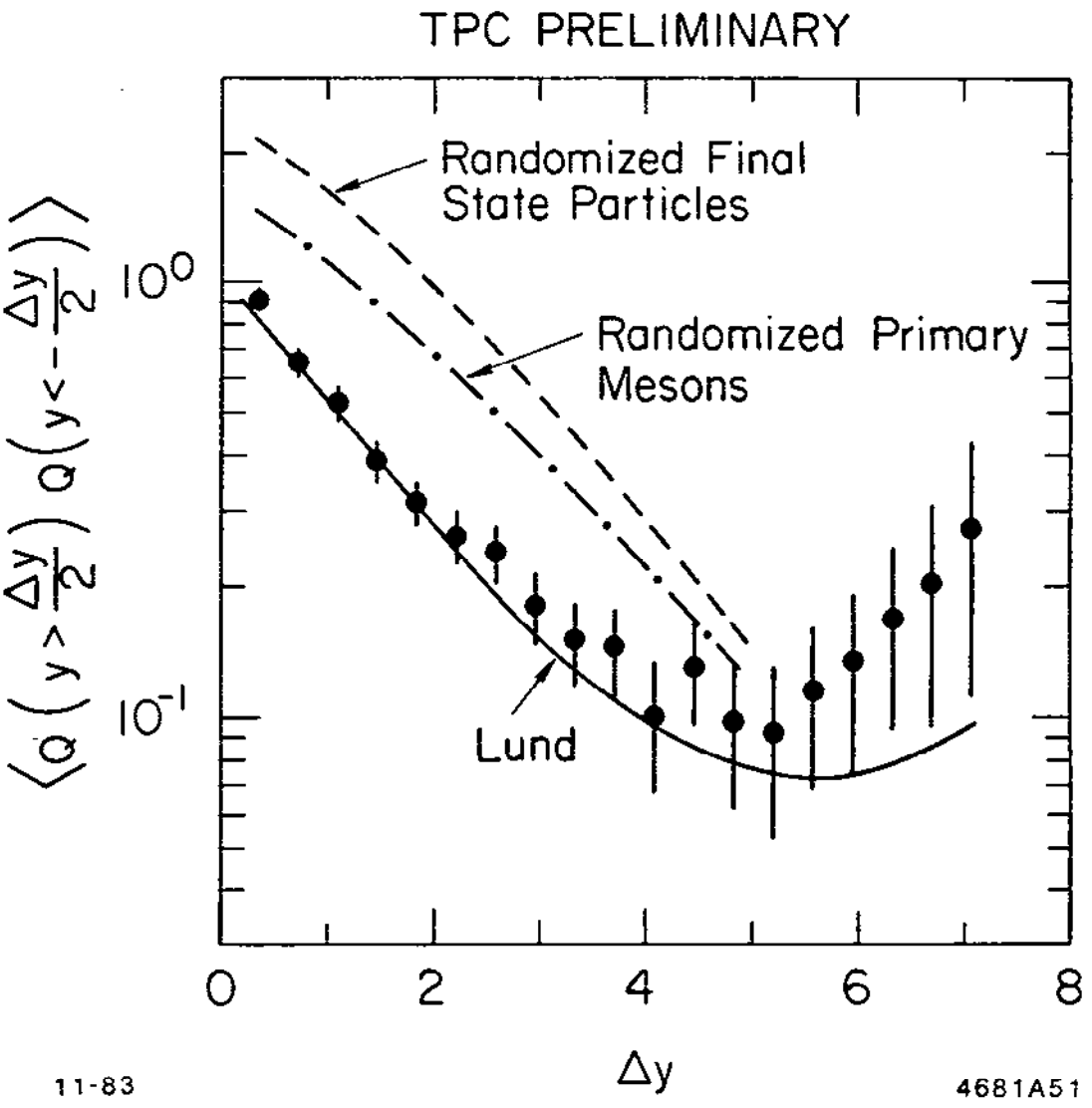
TPC PRELIMINARY
Randomized Final State Particles
Randomized Primary Mesons
Lund
$\langle Q(y > \frac{\Delta y}{2})\, Q(y < -\frac{\Delta y}{2}) \rangle$
10^0
10^{-1}
0
2
4
6
8
Δy
11-83
4681A51

Figure 55

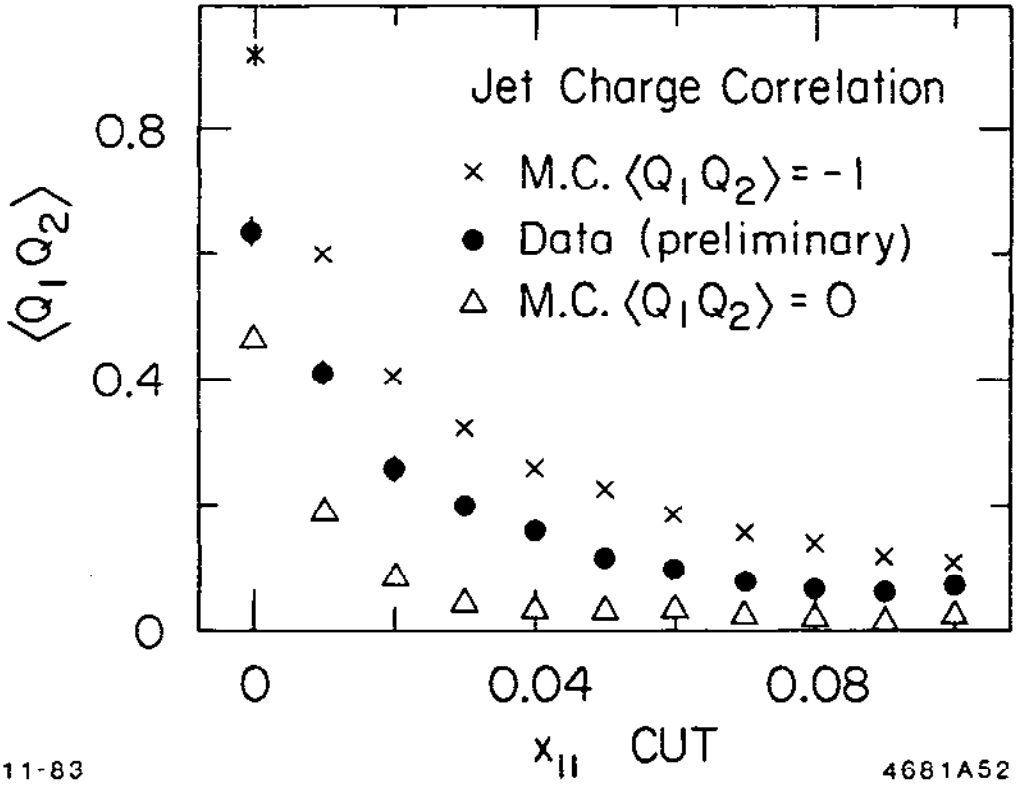
Jet Charge Correlation
× M.C. ⟨Q1 Q2⟩ = -1
● Data (preliminary)
△ M.C. ⟨Q1 Q2⟩ = 0
⟨Q1 Q2⟩
0.8
0.4
0
0
0.04
0.08
x11 CUT
11-83
4681A52

Figure 56

7.4 BARYON CORRELATIONS

If the diquark production mechanism is correct, we would expect that baryons would also show short range correlations. Other mechanisms may also lead to such effects; in any case it is interesting to determine whether baryon number is conserved locally or globally. We can study the mechanism of baryon production most easily by comparing the rates of proton–antiproton pairs produced in the same and opposite jets. Early data using time-of-flight techniques in the MARK II detector[33] used pairs of baryons in the region $x < 0.14$ and showed only slight enhancement of same jet $p\bar{p}$'s in the soft region.

This has been extended by the TASSO detector which uses its hadron arms to identify protons in the ranges $1 < p < 2.3$ and $3 < p < 5$ GeV/c. In a sample of 26,376 hadronic events, they find as shown in Table 9 that the observed pairs are predominantly produced in the same jet.

Table 9

TASSO Baryon Pairs (no acceptance corrections)		
	Opposite Jet	Same Jet
$p\bar{p}$	2.2 ± 2.8	15.2 ± 4.6
pp, $\bar{p}\bar{p}$	1.8 ± 2.6	-0.05 ± 2

As improved statistics become available, it will be interesting to test the diquark model assumption that the $p_\perp$ of the diquark (baryon) relative to the fragmentation axis is balanced by the $p_\perp$ of the antidiquark (antibaryon). This question has been examined by Bartl *et al.*, who suggest several tests of this mechanism. These studies should also be extended to pairs of strange mesons, although since the probability of $s\bar{s}$ production in the fragmentation process is higher than diquark production, the increased number of $s\bar{s}$ branchings will make it more difficult to test detailed $p_\perp$ balance and short range correlations.

7.5 Heavy Quark Fragmentation

The presence of heavy quark thresholds considerably complicates the analysis of present data since it means that mass effects which fall off as a power of

$$\frac{2M_Q}{\sqrt{s}} \tag{92}$$

can remain important to quite high energies. It is important then to correctly parameterize the fragmentation functions of heavy B and D mesons. Theoretically we expect the transition probability between a heavy quark Q and a state containing the heavy quark plus a light pair as shown in Figure 57 to be given by

$$P(i \to f) \sim \frac{1}{(\Delta E)^2} \tag{93}$$

where $\Delta E \sim E(Q\bar{q}) + E(q) - E(Q)$. If the heavy meson $Q\bar{q}$ carries a fraction z of the initial quark momentum, ΔE is

$$\left(M_Q^2 + z^2p^2\right)^{1/2} + \left(M_q^2 + (1-z)^2p^2\right)^{1/2} - \left(M_Q^2 + p^2\right)^{1/2} \sim 1 - \frac{1}{z} - \frac{\epsilon}{1-z} \tag{94}$$

where $\epsilon = (m_q/M_Q)^2$. The resulting transition probability will be[34]

$$D_Q^H(z) = \frac{1}{z}\,\frac{k}{\left[1 - \frac{1}{z} - \frac{\epsilon}{1-z}\right]^2} \tag{95}$$

which peaks toward larger z for heavier mesons.

Heavy mesons have been directly detected using the reaction

$$\begin{array}{lll} D^{*+} \to D^0\pi^+ & & \mathrm{BR} = 0.44 \pm 0.1 \\ \quad\quad \hookrightarrow & K^-\pi^+ & \mathrm{BR} = 0.03 \pm 0.06\ . \end{array}$$

Due to the small mass difference between the D^* and the D mesons,

$$\begin{aligned} M(D^{*\pm}) - M(D^0) &= 145.3\ \mathrm{MeV} \\ &= m_\pi + 5.7\,\mathrm{MeV} \end{aligned}$$

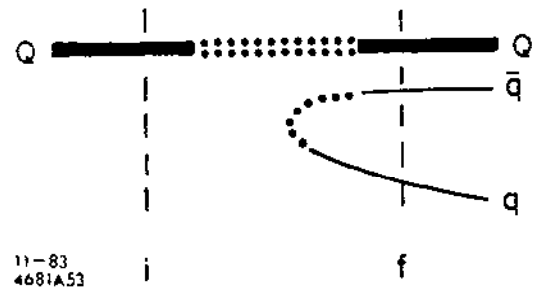

Figure 57

the system is highly constrained and a clean sample can be found without identification of the K meson.[35] Recent data from the DELCO detector uses Čerenkov identified K mesons to search for D^*'s in the mode

$$\begin{array}{lll} D^{*+} \rightarrow & D^0\pi^+ & \\ & \hookrightarrow & K\pi \\ & \rightarrow & K\pi x \\ & \rightarrow & K\pi\pi\pi \end{array} .$$

The measured cross sections as a function of the z of the D^* meson are shown in Figure 58, where for comparison all measurements have been normalized to a $D^* \rightarrow D\pi$ branching ratio of 0.44. Table 10 shows the values obtained for the ϵ parameter from fitting the z distributions to a fragmentation function of the form (95) and the total cross-sections and R values for D^* production. The average R value is 1.65 which indicates that D^* production is a significant fraction of the total charm and bottom quark fragmentation

$$\frac{\sigma(D^{*+} + D^{*-})}{2\sigma_{c,\bar{c}} + 2\sigma_{b,\bar{b}}} \sim 0.5 \quad . \tag{96}$$

Table 10

D^* Production Spectra and Cross-Sections				
Detector	$\sqrt{s}$	ϵ	$\sigma(D^{*\pm})$	R_{D^*}
MARK II	29	0.25	0.25 ± 0.13	2.5 ± 1.3
DELCO	29	0.39 ± 0.16	$0.20 \pm 0.3 \pm 0.07$	2.0 ± 0.8
CLEO	10		1.6 ± 0.6	1.8 ± 0.7
TASSO	34	0.18 ± 0.07	0.094 ± 0.041	$1.25 \pm 0.32 \pm 0.44$

As shown in Figure 59, the HRS detector has detected D^0 mesons directly in the $K\pi$ mass spectrum. This allows a direct comparison D^0 and D^* spectra which are found to be similar, and eventually will eliminate uncertainties in the total D^* production rate due to the $D^* \rightarrow D^0$ branching ratio.

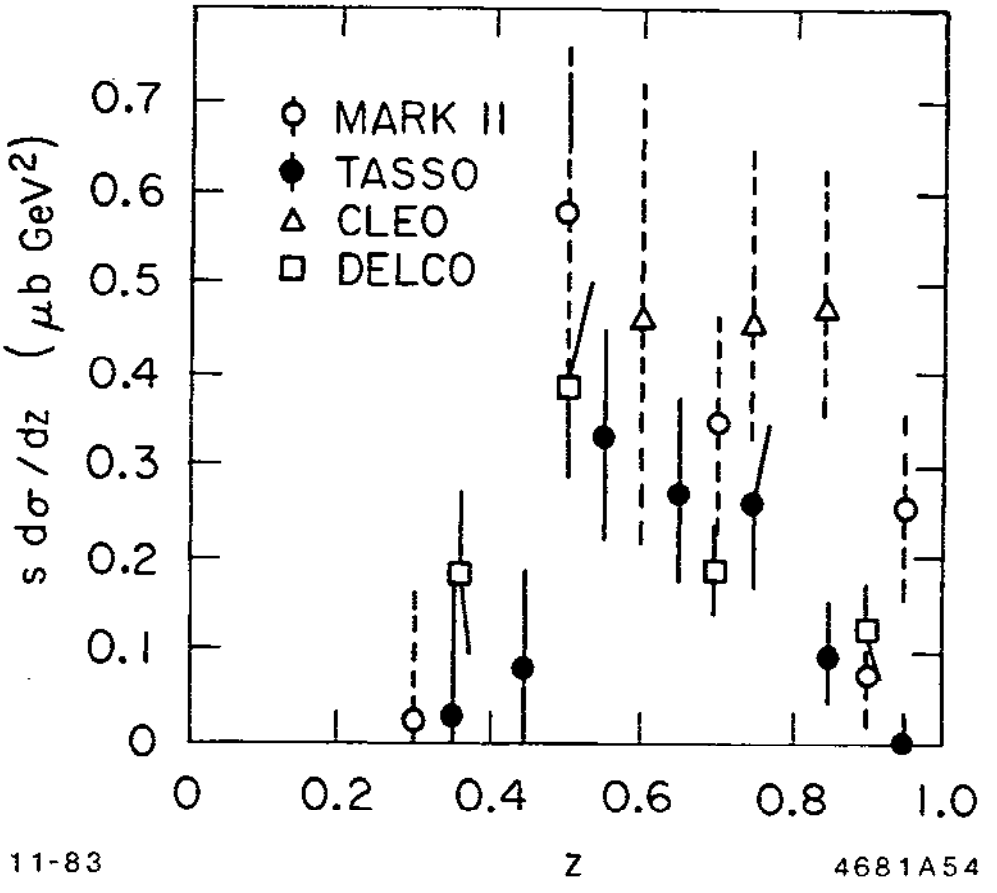
MARK II
TASSO
CLEO
DELCO
s dσ/dz (μb GeV²)
0.7
0.6
0.5
0.4
0.3
0.2
0.1
0
0
0.2
0.4
0.6
0.8
1.0
z
11-83
4681A54

Figure 58

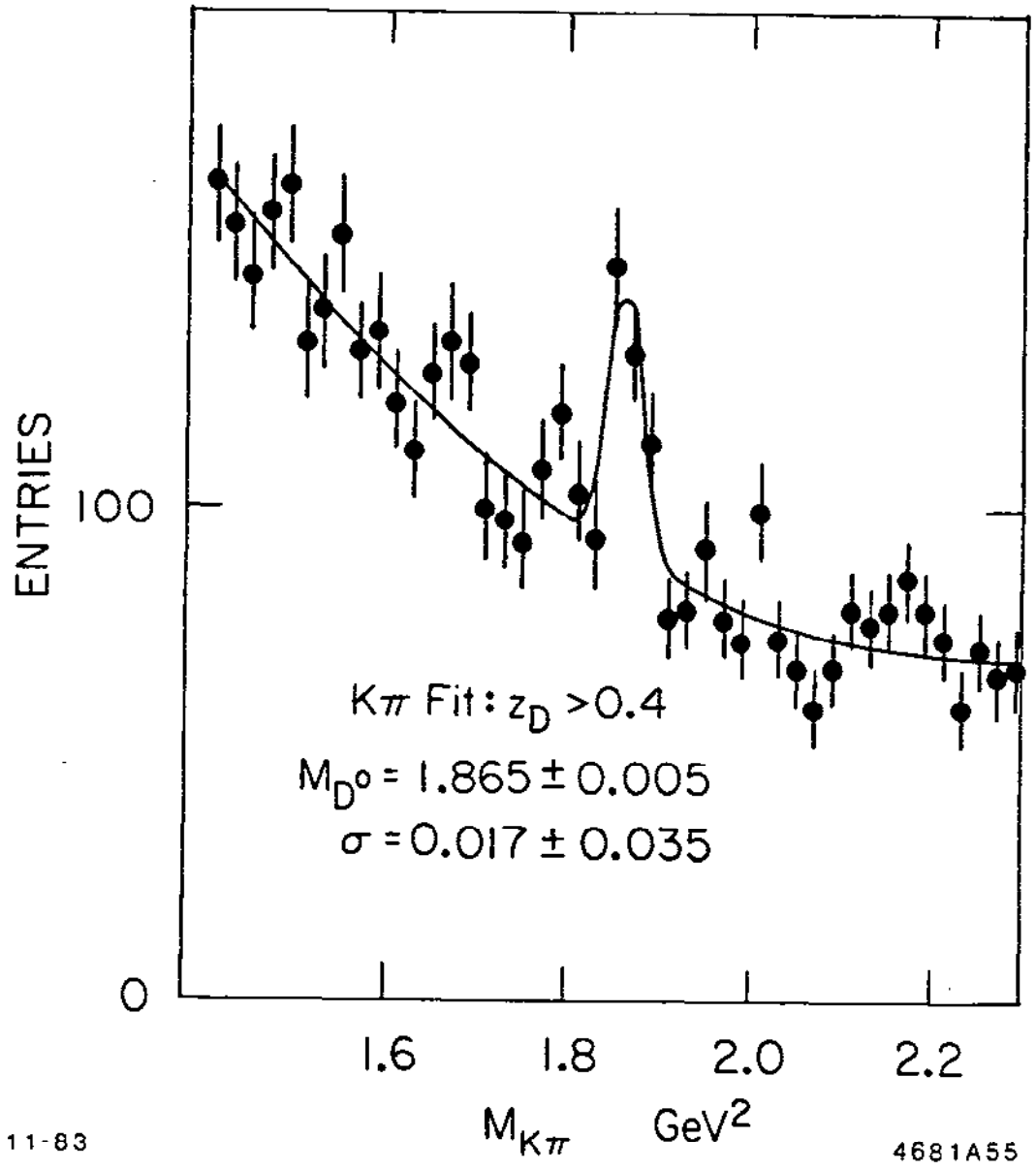
ENTRIES
100
0
Kπ Fit : z_D >0.4
M_{D^0} = 1.865 ± 0.005
σ = 0.017 ± 0.035
1.6
1.8
2.0
2.2
$M_{K\pi}$ GeV^2
11-83
4681A55

Figure 59

Charm and bottom mesons can also be detected indirectly by fitting the transverse momentum spectra of leptons from the semileptonic decays of these mesons. Detected leptons are binned in momentum and transverse momentum and the spectrum is fit with the semileptonic branching ratios $\mathrm{BR}(c \to e)$, $\mathrm{BR}(b \to e)$ and the shape of the b fragmentation function (ϵ_b) as free parameters. The shape of the c fragmentation function is taken from the D^* cross-section. Since high $p_\perp$ bins are dominated by $b \to e$ and low $p_\perp$ bins are dominated by $c \to e$, the two contributions can be separated. The results of the fit from the MARK II detector[36] give

$$\mathrm{BR}(c \to e) = 7 \pm 2 \pm 2\% \quad ,$$

$$\mathrm{BR}(b \to e) = 11 \pm 3 \pm 3\% \quad ,$$

$$\epsilon_b = 0.04^{+0.35}_{-0.25} \quad .$$

Similar measurements have been done by the MAC detector using the muon spectra. They find[37]

$$\mathrm{BR}(c \to \mu) = 7.6^{+9.7}_{-2.7}\% \quad ,$$

$$\mathrm{BR}(b \to \mu) = 15.5^{+5.4}_{-2.9}\% \quad ,$$

$$\epsilon_b = 0.008^{+0.037}_{-0.008} \quad .$$

Figure 60 shows a comparison of the fragmentation functions for heavy mesons for values $\epsilon_c \sim 0.25$ and $\epsilon_b \sim 0.04$ and indicates that the spectrum from b quarks is considerably harder than that of c quarks. Using a value of $\epsilon_c \sim 0.25$, the expected parameter for b quarks using Equation (94) would be

$$\epsilon_b \sim \epsilon_c \cdot \frac{m_c^2}{m_b^2} \sim 0.03 \tag{97}$$

in good agreement with the data.

7.6 Gluon Fragmentation

The gluon fragmentation function is believed to behave *asymptotically* in QCD in a way which differs from quark jets. The total multiplicity and mean transverse momentum of gluon jets should be larger. In order to test these predictions, however,

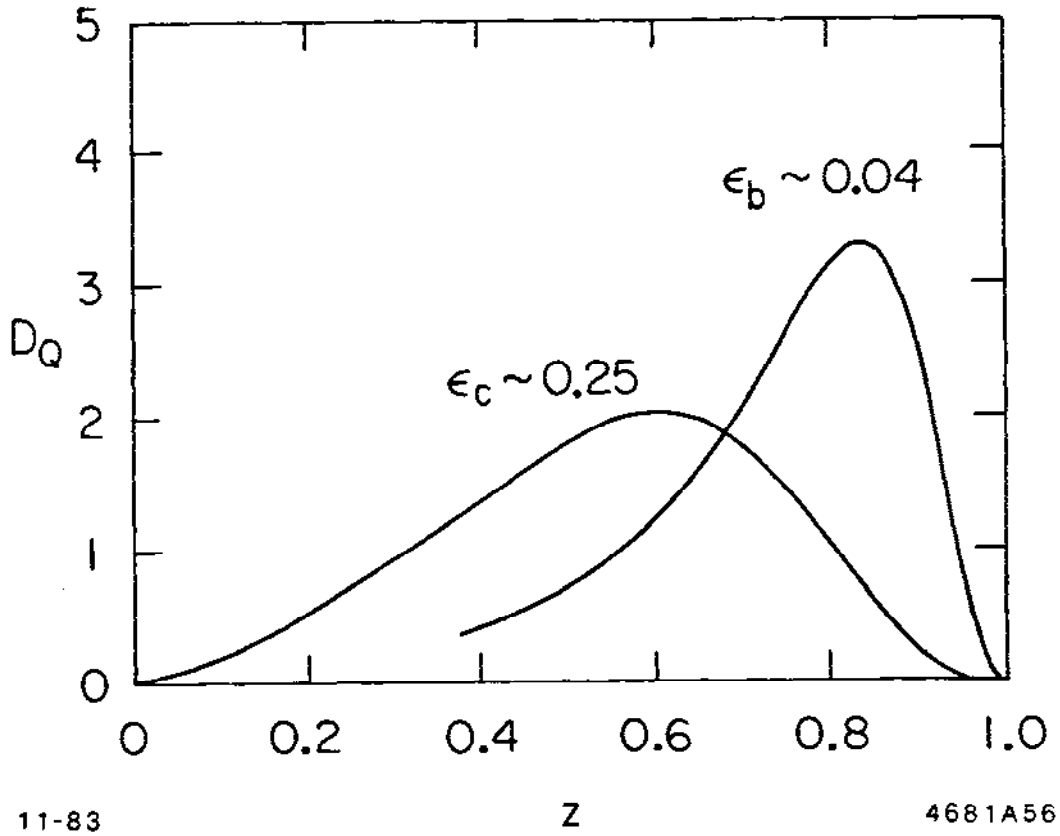
5
4
3
2
1
0
D_Q
$\epsilon_b \sim 0.04$
$\epsilon_c \sim 0.25$
0
0.2
0.4
0.6
0.8
1.0
Z
11-83
4681A56

Figure 60

we must be careful since, on average, the energy of gluon jets is much less than that of observed quark jets. Figure 61 shows the energy distributions dN/dx_i of the three jets produced in QCD at the parton level. Note that there is almost no overlap at a fixed center-of-mass energy between the fastest jet (quark) and the slowest jet (gluon). In fact, in the region where they overlap, the confusion about which jet is actually the gluon is maximal! Since we have seen that particle fractions and other jet parameters are energy dependent, we would like to compare jets which we believe to be gluons with quark jets of the **same** energy. This has been done by the JADE group using center-of-mass energies of 22 GeV and 29–36.4 GeV.[38] Gluon jets of energy between 7 and 10 GeV come mainly from the higher center-of-mass data, and can be compared to fast jets coming predominantly from the 22 GeV sample. Figure 62(a) shows the mean transverse momentum of the three jets ($x_1 > x_2 > x_3$) as a function of the detected jet energy. The jet energies are calculated in each event from the angles of the three-jets. The observed distributions are consistent with an independent fragmentation model where σ_q is 500 MeV/c for a gluon and 330 MeV/c for a quark jet. They are also consistent with the Lund model which results in a softer fragmentation function for gluons than for quarks [see Equation (74)]. As shown in Figure 62(b), these differences are not seen in Monte Carlo events where the quark and gluon have identical fragmentation functions (Hoyer model).

In order to eliminate the possibility that the above result arises from incorrect identification of the quark axis for the first and second jets at 22 GeV, the JADE group has also compared the $p_\perp$ spectra of particles seen in a 50° cone around the third jet at 33 GeV with the spectra seen for a similar cone around the axis of two-jet events at 14 GeV.[39] Again, the Monte Carlo shows that there is little relative bias in the two spectra [Figure 63(a)] and that similar spectra are obtained for Monte Carlo data with identical quark and gluon fragmentation functions. The data indicate [Figure 63(b)] again that the gluon jets at 33 GeV are wider than the quark jets.

The particle compositions in the gluon jets could also differ from quark jets. In this respect, since the average gluon jet energy is small, we would expect heavier mass particle production to be suppressed at low energies as it is in quark jets. Gluons, however, are flavor blind. Unlike the fragmentation process which involves very soft gluons

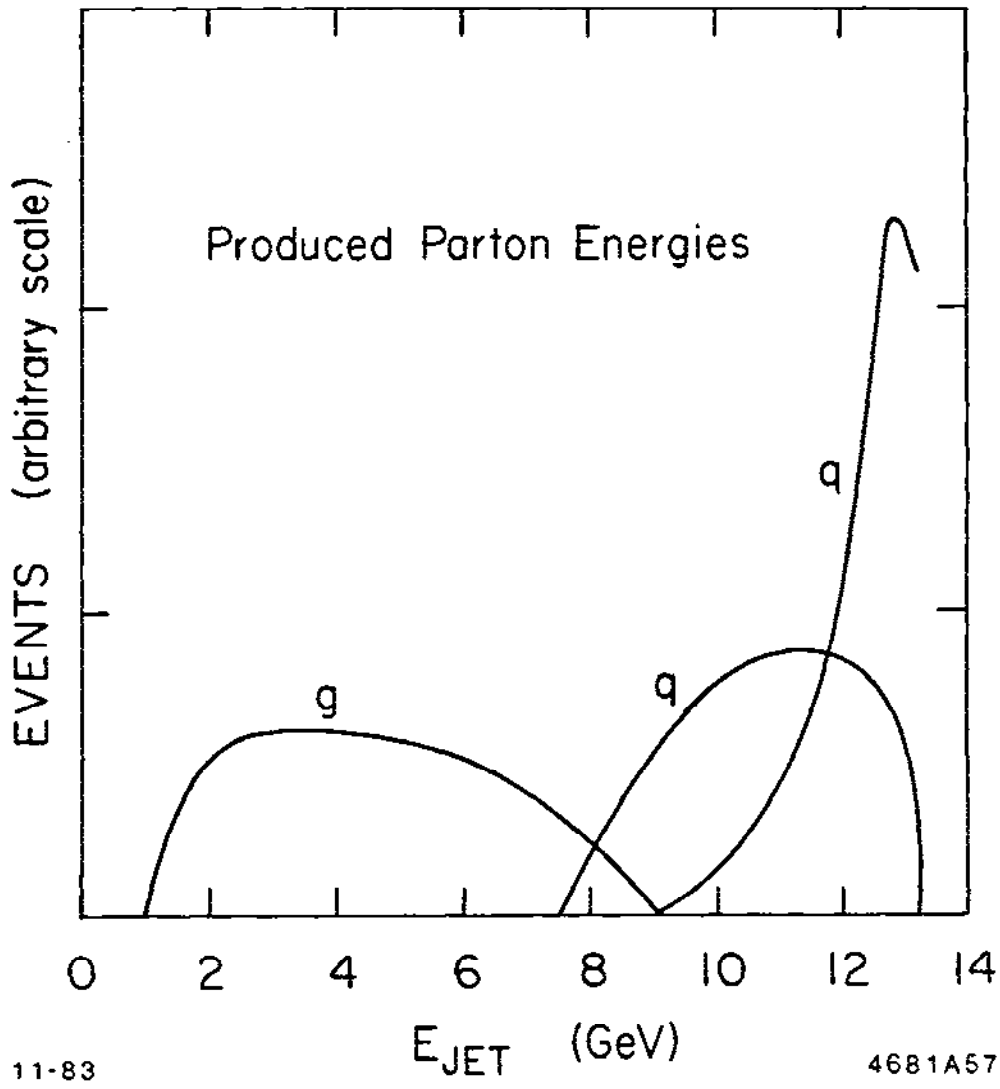
Produced Parton Energies
EVENTS (arbitrary scale)
g
q
q
0
2
4
6
8
10
12
14
E_JET (GeV)
11-83
4681A57

Figure 61

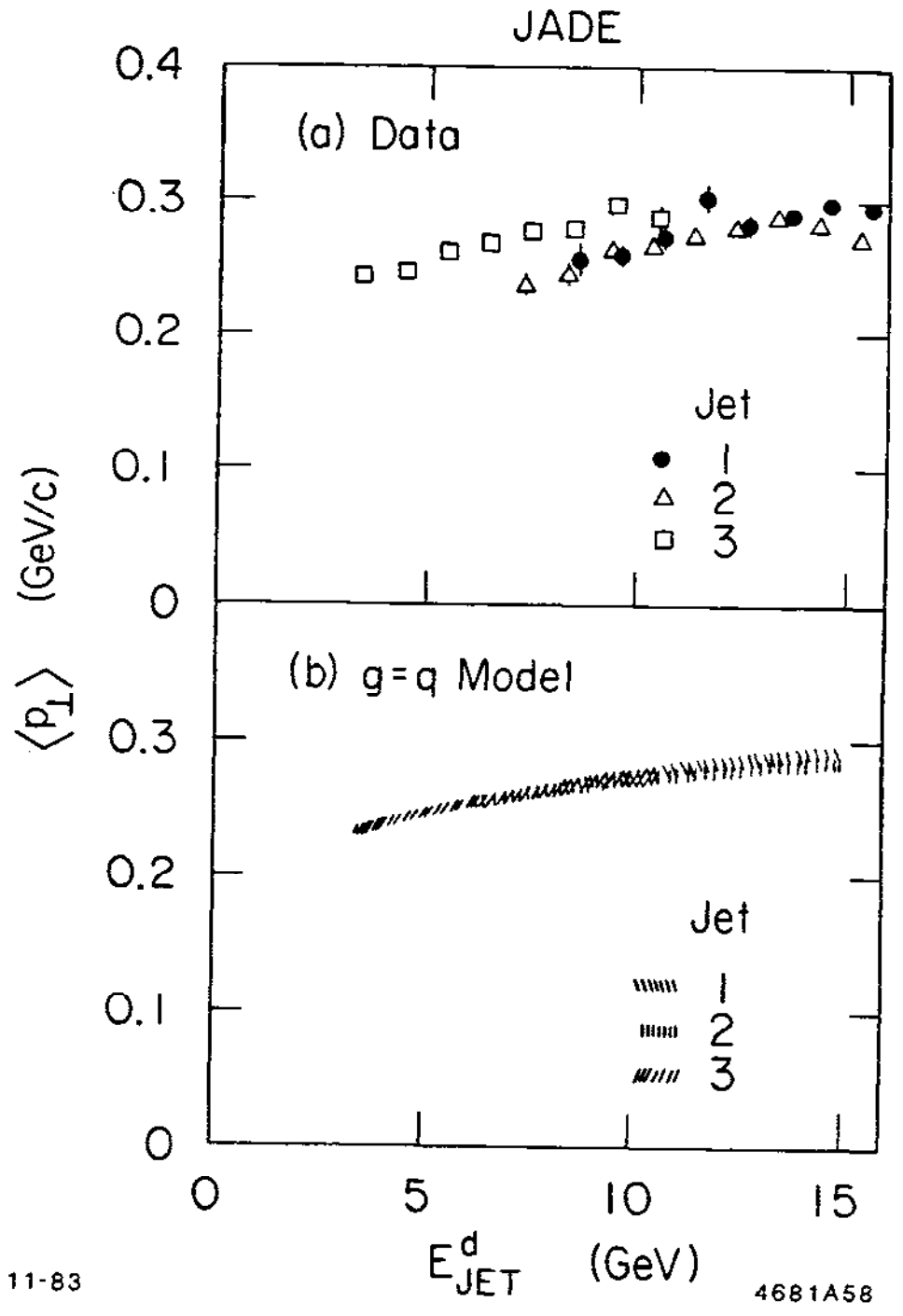
JADE
(a) Data
(b) g=q Model
Jet
1
2
3
Jet
1
2
3
0.4
0.3
0.2
0.1
0
0.3
0.2
0.1
0
0
5
10
15
⟨p_T⟩ (GeV/c)
E^d_JET (GeV)
11-83
4681A58

Figure 62

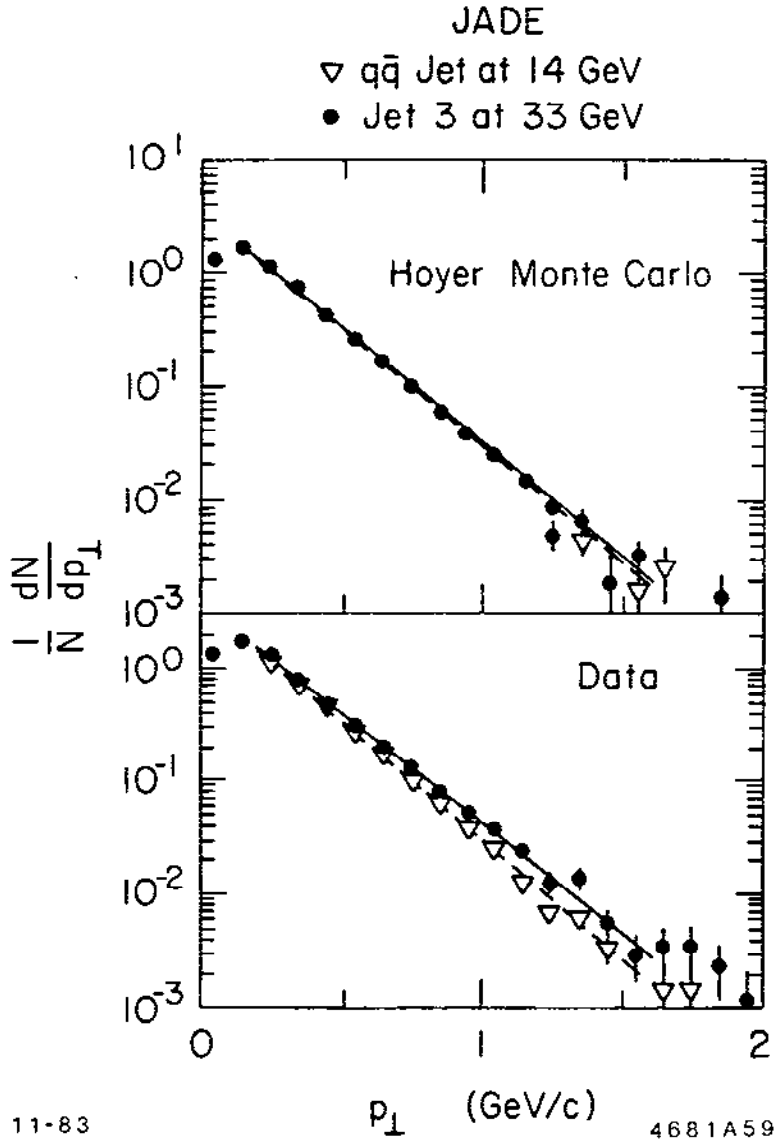
JADE
▽ qq̄ Jet at 14 GeV
• Jet 3 at 33 GeV
Hoyer Monte Carlo
Data
$\frac{1}{N}\frac{dN}{dp_T}$
$p_\perp$ (GeV/c)
11-83
4681A59

Figure 63

so that strange quarks are suppressed, three-jet events contain hard gluons and hence may result in increased strange particle production.

An interesting hint that this may be the case has been found by the TASSO group which has compared the $\Lambda, \bar{\Lambda}$ yield in three-jet events with that found in the entire event sample. The yield in three-jet events is[40]

$$0.052 \pm 0.010 \ \Lambda_s' \ / \ \text{event}$$

and in the entire sample it is

$$0.022 \pm 0.003 \ \Lambda_s' \ / \ \text{event} \quad .$$

Since no correction has been made for the lower average energy of the gluon jet, this may indicate significant enhancement of Λ production for the third jet. A similar enhancement has been seen by the JADE group in the production of η mesons.[41] Events identified at 34 GeV as 2 jets ($S < 0.15$) contain

$$0.22 \pm 0.06 \pm 0.06 \ \eta \ / \ \text{event}$$

while the event sample as a whole has

$$0.72 \pm 0.10 \pm 0.18 \ \eta \ / \ \text{event} \quad .$$

In both of these analyses, no corrections have yet been applied for the contribution of b and c quark events to the non-two-jet samples.

8. Energy–Energy Correlations

The parameterization of fragmentation is obviously a difficult and complex task. There are a large number of parameters in any model which must be determined from the data, and as we have seen, most of these parameters are correlated or energy dependent. While some of the fragmentation studies which have been mentioned are interesting tests of soft hadron dynamics (quantum number correlations, particle fractions in the third jet, baryon dynamics), our primary purpose in studying fragmentation was to eliminate uncertainties due to soft corrections to perturbative processes.

It appears at present, for example, that different models make different predictions about the relationship of the perturbative parameter α_s and the observed three-jet fraction.

One can, however, take an entirely different approach, and look for new observables which will be insensitive to fragmentation. This assumes of course that hard and soft processes do in fact factor and that such observables exist. This is by no means a proven conclusion yet in QCD.[42]

One possibility for a fragmentation independent measure of α_s is the behavior of the correlation function between two energy deposits in finite solid angle elements. As shown in Figure 64, one determines the energy weighted cross-section for two solid angle elements Ω_1 and Ω_2:

$$\frac{1}{\sigma_0}\frac{d\Sigma}{d\Omega_1\, d\Omega_2} \quad ,$$

$$\Sigma = S_N \int \left(\frac{d^2\sigma}{dx_1\, dx_2}\right) x_1\, x_2\, dx_1\, dx_2 \quad , \tag{98}$$

$$S_N = 1, \;\; i = j\,; \qquad S_N = 2, \;\; i \neq j \quad .$$

Although this cross-section looks quite complicated, it solves a number of QCD problems. Since we look only at the energy deposit, and do not ask whether the parent parton is a gluon or a quark, problems due to collinear gluon emission within a quark jet are eliminated. Furthermore, soft gluon problems are cured by using the energy weighted cross-section.

The energy-energy correlation function can be calculated in first order QCD and is of the form[43]

$$\frac{1}{\sigma_0}\frac{d\Sigma}{d\Omega_1\, d\Omega_2} = A(\chi)\,\frac{1}{\sigma}\left(\frac{d\sigma}{d\Omega_1} + \frac{d\sigma}{d\Omega_2}\right) + B(\chi)\,\frac{3}{16\pi}\,(\cos\chi + \cos\theta\cos\theta') \tag{99}$$

where the two elements of solid angle Ω_1, Ω_2 are specified by angles θ, ϕ, θ', ϕ' and χ is the angle between $d\Omega_1$ and $d\Omega_2$. The functions A and B determine the independent and correlated parts of the energy deposit and are given by

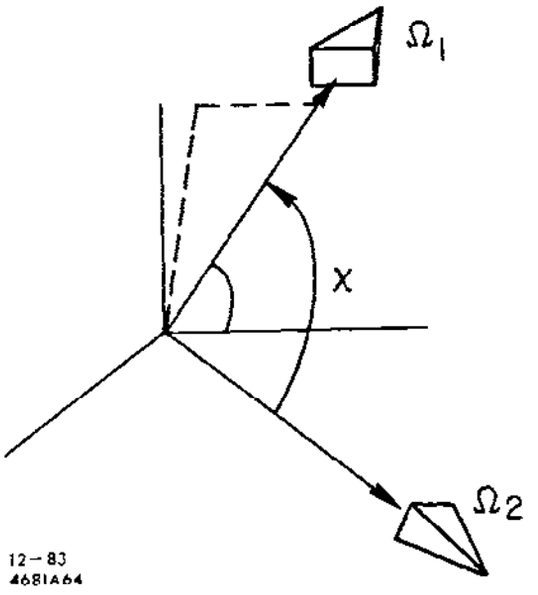

Figure 64

$$A(\chi) = \frac{\alpha_s}{12\pi}\,\frac{1}{1-z}\left[\left(\frac{3}{z^5}-\frac{4}{z^4}\right)\ell n\,(1-z)+\frac{3}{z^4}-\frac{5}{2z^3}-\frac{1}{z^2}\right]\quad,$$
$$B(\chi) = \frac{\alpha_s}{12\pi}\,\frac{1}{1-z}\left[\left(\frac{12}{z^5}-\frac{16}{z^4}+\frac{4}{z^3}\right)\ell n\,(1-z)+\frac{12}{z^4}-\frac{10}{z^3}\right] \tag{100}$$

where $z = (1/2)(1-\cos\chi)$. Note that both of these functions are proportional to α_s, and therefore if second order corrections[44] are small, one could hope to determine α_s directly from a fit to the energy-energy correlation.

We can also see from the forms above that the perturbative calculations tend to be singular both for large and small χ, ($z = 0, 1$). In these regions, one should not attempt to fit the energy-energy correlation to the perturbative formulae since there are significant logarithmic and fragmentation dependent corrections.[45] In the simplest models of fragmentation, one expects the fragmentation contributions of a single jet to be of the form[43]

$$\frac{c(p_\perp)}{4\pi\sqrt{s}}\,\sin^{-3}\chi \tag{101}$$

where the coefficient $c(p_\perp)$ measures the width of the energy weighted jet, and depends on the jet multiplicity

$$\langle n\rangle \simeq c\,\ell n\,\sqrt{s} + \text{constant} \quad . \tag{102}$$

If the fragmentation is the same for both jets in a two-jet event, then it contributes a symmetric term which will cancel in the asymmetry

$$A(\chi) = \frac{1}{\sigma}\left[\left.\frac{d\sigma}{d\cos\chi}\right|_{\pi-\chi} - \left.\frac{d\sigma}{d\cos\chi}\right|_{\chi}\right] \quad . \tag{103}$$

This cancellation is however, not complete in a three-jet event as illustrated in Figure 65. Jets two and three are not at $\chi = 180°$ and may have widths which differ from those of jet one. Thus we expect some residual fragmentation dependence even in the asymmetry.[46]

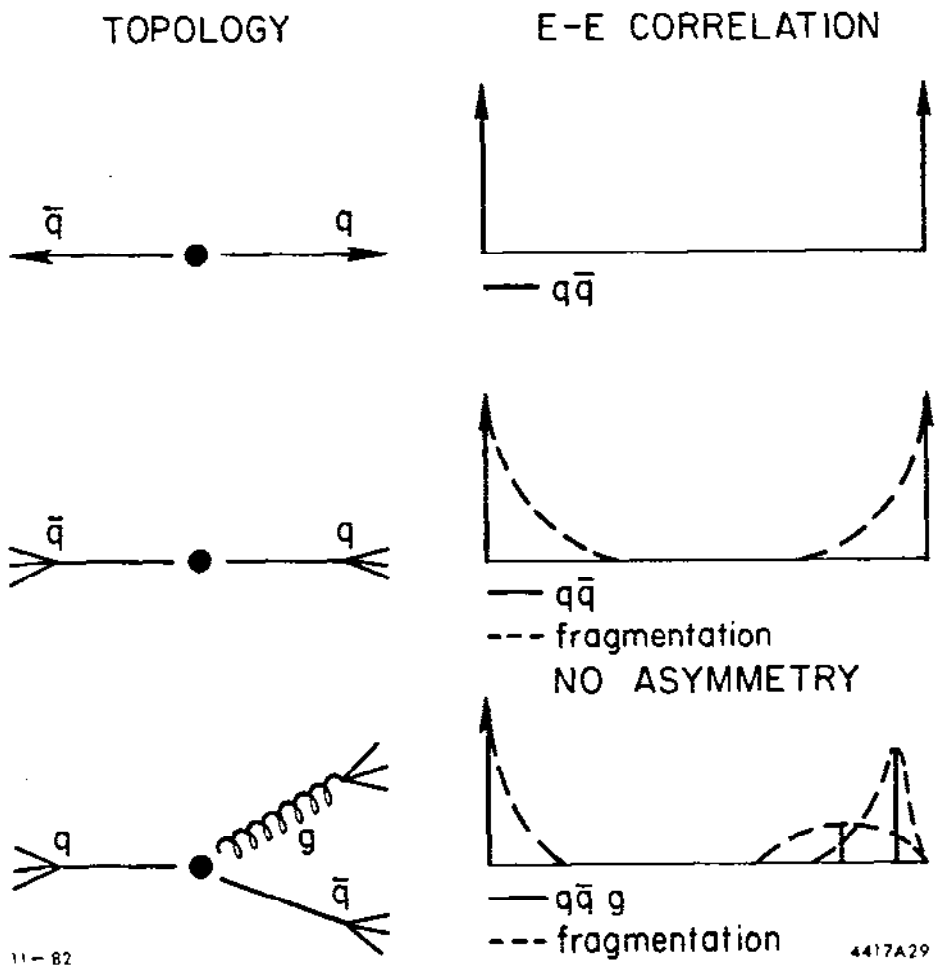
TOPOLOGY
E-E CORRELATION
q̄
q
qq̄
q̄
q
qq̄
fragmentation
NO ASYMMETRY
q
g
q̄
qq̄ g
fragmentation
11-82
4417A29

Figure 65

Figure 66 shows the data from the CELLO collaboration[47] for the energy-energy correlation as a function of χ. A fit for α_s yields

$$\begin{aligned} \alpha_s &= 0.21 \pm 0.01 \quad , \\ c\langle p_\perp \rangle &= 1.2 \pm 0.05 \end{aligned} \tag{104}$$

to first order in α_s. Fitting the asymmetry alone gives a value of α_s of

$$\alpha_s = 0.15 \pm 0.02 \quad .$$

A similar fit by the MARK II collaboration[46] gave

$$\alpha_s = 0.19 \pm 0.02 \pm 0.03$$

to first order in α_s and used a fragmentation form

$$\frac{\alpha_s A_1}{\sqrt{s}} \begin{cases} \frac{1}{\sin^3 \chi} & \cos\chi > 0 \\ \sin\chi & \cos\chi < 0 \end{cases} \quad . \tag{105}$$

Data from the MAC detector are shown in Figure 67. The data from different detectors cannot always be compared directly because they may or may not be corrected for experimental acceptances. In addition, the MARK II data are normalized using

$$\frac{E_i E_j}{s}$$

and the MAC data are normalized to

$$\frac{E_i E_j}{(E_{vis})^2} \quad .$$

At the moment, there are still uncertainties of order fifteen percent in the value of α_s determined in this way due to uncertainties in second order corrections, the form of the fragmentation contributions, and the angular range of χ which should be used to

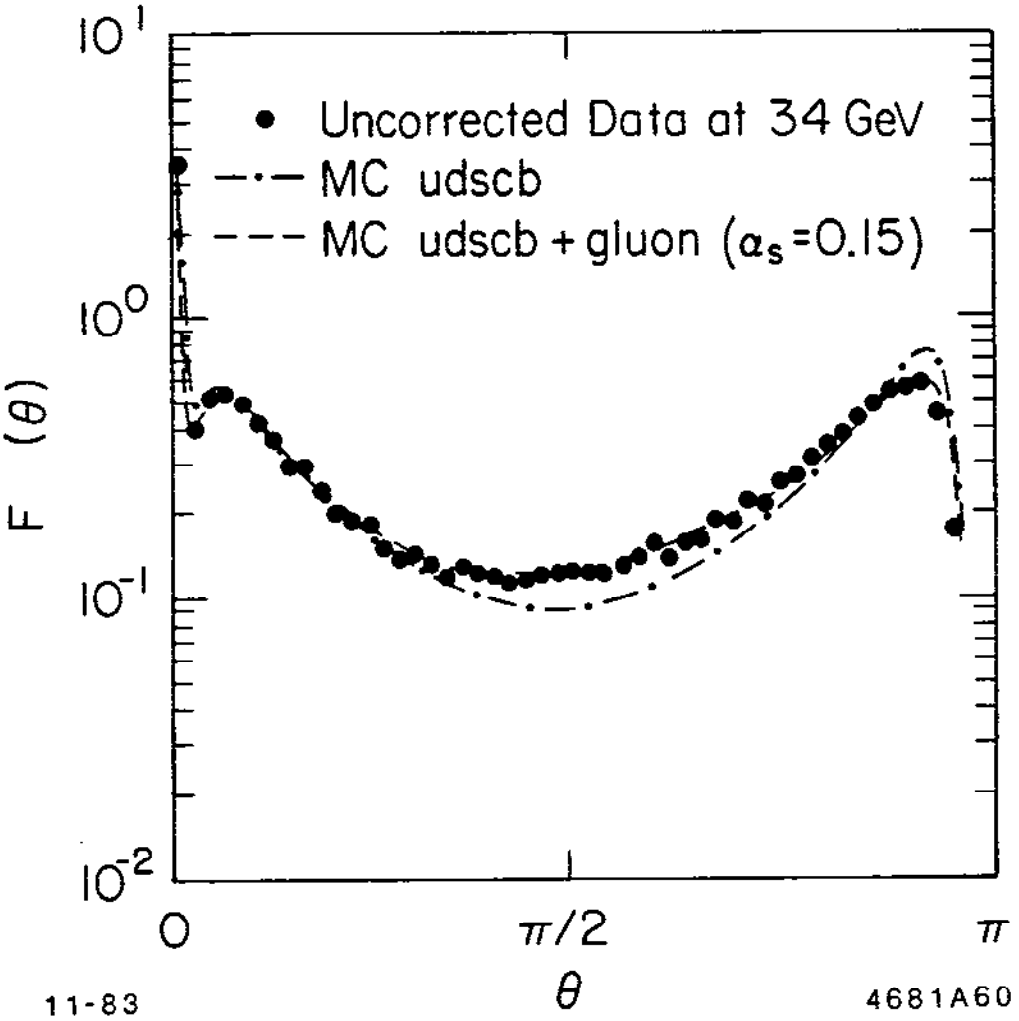
Uncorrected Data at 34 GeV
MC udscb
MC udscb + gluon (α_s=0.15)
10^1
10^0
10^{-1}
10^{-2}
F (θ)
0
π/2
π
θ
11-83
4681A60

Figure 66

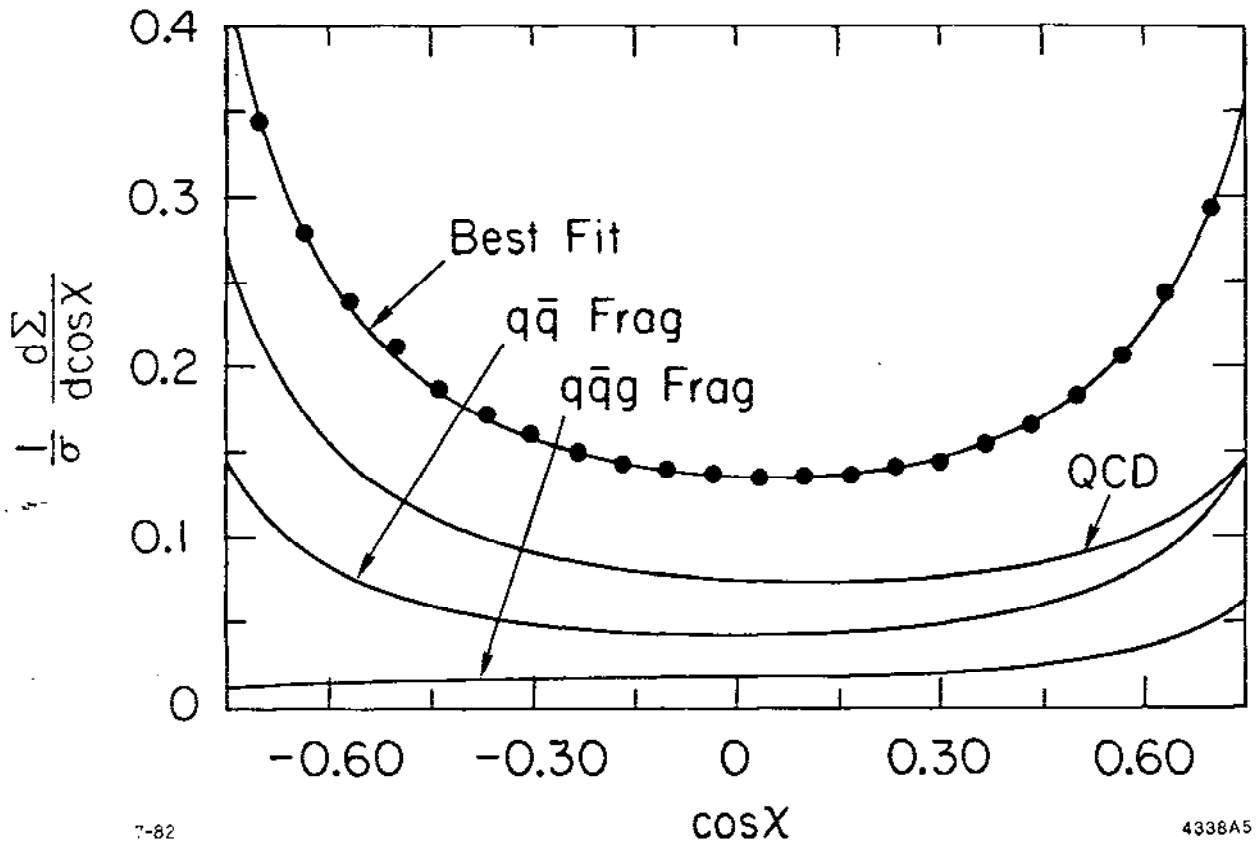
0.4
0.3
0.2
0.1
0
$\frac{1}{\sigma}\frac{d\Sigma}{d\cos\chi}$
Best Fit
$q\bar{q}$ Frag
$q\bar{q}g$ Frag
QCD
-0.60
-0.30
0
0.30
0.60
cosχ
7-82
4338A5

Figure 67

fit for α_s. The technique, however, seems promising, and recent data from the MARK J collaboration[48] indicate that by fitting α_s over the restricted region $|\cos\chi| < 0.72$ and using second order corrections (ERT), the independent and string models give essentially the same result for α_s

$$\alpha_s = 0.14 \pm 0.01 \qquad \text{Lund} \quad ,$$

$$\alpha_s = 0.12 \pm 0.01 \qquad \text{Ali} \quad .$$

9. Summary

We have a simple perturbative picture of the production of hadrons from e^+e^- annihilations which works quite well in predicting the main features of this interaction. It explains the magnitude of the total cross-section, the basic two-jet structure, and the final state angular distributions. It is also consistent with our present ideas about the structure of hadronic matter and the requirement that at high enough energies, the corrections due to strong interactions are small and hence treatable in a perturbative sense. We have seen, however, that to progress beyond this point requires a detailed model of fragmentation phenomena and that differences in models prevent us from making clean predictions about QCD. It is therefore important that we continue to study the fragmentation process and try to parameterize it as well as possible. Large amounts of experimental data are now available on this subject, and new tests will become available as experimenters look in more detail at the behavior of quantum number correlations and energy dependent effects. In doing this, it will be important to keep in mind that mass effects can yield significant energy variations in the model parameters.

Our eventual goal should be to find ways of treating the data which will yield quantitative tests of QCD. Studies of three- and four-jet fractions, three-jet fragmentation properties, and energy-energy correlations have begun, and hopefully with improved understanding of fragmentation effects, will yield such tests.

References

1. J. Dorfan, SLAC-PUB-2963, August 1982.
2. E. Fermi, Prog. Theor. Phys. 5, 570 (1950).
3. J. Lepore and R. Stuart, Phys. Rev. 94, 1724 (1954).
4. See for example, G. Hanson *et al.*, Phys. Rev. D26, 991 (1982).
5. R. Brandelik, *et al.*, Phys. Lett. 89B, 418 (1980).
6. See for example, S. Brandt and H. D. Dahmen, Z. Phys. C1, 61 (1979).
7. H. Georgi, M. Machacek, Phys. Rev. Lett. 39, 1237 (1977).
8. A. De Rujula, J. Ellis, E. Floratos, M. Gaillard, Nucl. Phys. B138, 387 (1978).
9. San Lan Wu and Georg. Zobernig, Z. Phys., C2, 107 (1979).
10. See also, H. Daum, H. Meyer, J. Burger, Z. Phys. C8, 167 (1981); J. Dorfan, Z. Phys. C7, 349 (1981); and K. Lanius, DESY 80/36.
11. D. Cords, Proc. XXth Int. Conf. on High Energy Physics, Madison, Wisconsin, DESY 80/92.
12. TASSO, Phys. Lett. 94B, 437 (1980).
13. P. Söding, G. Wolf, Ann. Rev. Nucl. Sci. 31, 231 (1981). Data from TASSO, Phys. Lett. 86B, 243 (1979),
14. See C. H. Llewellyn Smith, Proc. XXth Int. Conf. on High Energy Physics, Madison, Wisconsin, p. 1345.
15. T. Appelquist, H. Politzer, Phys. Rev. Lett. 34, 43 (1975).
16. J. Ellis, I. Karliner, Nucl. Phys. B148, 141 (1979).
17. A. Bartl, SLAC-PUB-3163.
18. R. Ellis, D. Ross and A. Terrano, Nucl. Phys. B178, 421 (1981); J. Vermaseren, K. Gaemers and S. Oldham, Nucl. Phys. B187, 301 (1981).

19. K. Fabricius, G. Kramer, G. Schierholz and I. Schmitt, Z. Phys. C11, 315 (1981).

20. T. Gottschalk, Phys. Lett. 109B, 331 (1982).

21. A. De Rujula *et al.*, Nucl. Phys. B138, 387 (1978).

22. J. Schwinger, Phys. Rev. 82, 664 (1951).

23. For a more detailed discussion of the model parameters see: T. Sjöstrand, Comput. Phys. Commun. 28, 229 (1983) and Comput. Phys. Commun. 27, 243 (1982).

24. B. Andersson, G. Gustafson and T. Sjöstrand, Phys. Lett. 94B, 211 (1980).

25. H. J. Behrend *et al.*, Nucl. Phys. B218, 269 (1983).

26. W. Bartel *et al.*, Phys. Lett. 119B, 239 (1982).

27. B. Adeva *et al.*, Phys. Rev. Lett. 50, 2051 (1983).

28. Direct observation of η's indicates $\sim 0.7\,\eta$'s/event at 34 GeV, JADE, DESY 83-063, July 1983.

29. S. Cooper, LBL-11322, August 1980.

30. TASSO, Phys. Lett. 117B, 135 (1982).

31. TASSO, Phys. Lett. 100B, 357 (1981).

32. Ch. Berger *et al.*, Nucl. Phys. B214, 189 (1983).

33. R. Hollebeek, Int. Symp. on Lepton Photon Interaction at High Energy, Bonn, 1981.

34. C. Peterson, D. Schlatter, I. Schmitt and P. Zerwas, Phys. Rev. D27, 105 (1983).

35. J. Yelton *et al.*, Phys. Rev. Lett. 49, 430 (1982).

36. M. Nelson *et al.*, Phys. Rev. Lett. 50, 1542 (1983).

37. E. Fernandez *et al.*, Phys. Rev. Lett. 50, 2054 (1983).

38. W. Bartel *et al.*, Phys. Lett. 123B, 460 (1983).

39. W. Bartel *et al.*, DESY 82/086, Phys. Lett. 123B, 460 (1983).

40. San Lan Wu, DESY 83-007, February 1983.

41. W. Bartel *et al.*, DESY 83-063, July 1983.

42. H. Quinn, SLAC-PUB-3190, August 1983.

43. C. Basham, L. Brown, S. Ellis and S. Love, Phys. Rev. D17, 2298 (1978).

44. D. Richards, W. Stirling, and S. Ellis, Phys. Lett. 119B, 193 (1982); A. Ali and F. Barreiro, Phys. Lett. 118B, 155 (1982).

45. D. Richards, W. Stirling and S. Ellis, DAMTP 83/1.

46. D. Schlatter, *et al.*, Phys. Rev. Lett. 49, 521 (1982).

47. H. S. Behrend *et al.*, Z. Phys. C14, 95 (1982).

48. B. Adeva *et al.*, Phys. Rev. Lett. 50, 2051 (1983).